

Whispering-gallery mode resonators for nonlinear and quantum optical applications

Matthew Thomas Simons

Herndon, Virginia

Master of Science, College of William and Mary, 2009

Bachelor of Science, University of Virginia, 2007

A Dissertation presented to the Graduate Faculty
of the College of William and Mary in Candidacy for the Degree of
Doctor of Philosophy

Department of Physics

The College of William and Mary

August, 2014

©2014
Matthew Thomas Simons
All rights reserved.

APPROVAL PAGE

This Dissertation is submitted in partial fulfillment of
the requirements for the degree of

Doctor of Philosophy

Matthew Thomas Simons

Approved by the Committee, June, 2014

Committee Chair

Associate Professor Irina Novikova, Physics
The College of William and Mary

Associate Professor Seth A. Aubin, Physics
The College of William and Mary

Distinguished VMEC Professor R. Alejandra Lukaszew, Physics
The College of William and Mary

Assistant Professor Eugeny E. Mikhailov, Physics
The College of William and Mary

Assistant Professor Hannes Schniepp, Applied Science
The College of William and Mary

ABSTRACT

Quantum information is the next frontier in communications. To realize quantum communications, the quantum mechanical properties of today's best communication medium, light, must be harnessed in a scalable and efficient manner.

Whispering-gallery mode resonators (WGMRs), a type of optical cavity, have advantages over traditional designs that can enhance processes used in the generation of nonclassical (quantum) states of light. In particular they reduce the power threshold for intensity-dependent nonlinear phenomena. One such process, second harmonic generation, can reduce the shot noise of light below the standard quantum limit. This dissertation explores the theoretical analysis and experimental tests of noise reduction through second harmonic generation in a crystalline whispering-gallery mode resonator. We also observe the generation of another nonlinear optical process, hyper-Raman scattering, at modest optical powers inside a crystalline WGMR. The change in optical properties of vanadium dioxide due to an optically-induced phase transition is also studied as a potential Q-switching material in a WGMR-type cavity.

TABLE OF CONTENTS

Acknowledgments	iv
Dedication	v
List of Tables	vi
List of Figures	vii
CHAPTER	
1 Introduction	2
2 Nonlinear optics and cavities	5
2.1 Nonlinear optics	7
2.1.1 Second harmonic generation	9
2.1.2 Nonlinear crystals	13
2.1.3 Phase-matching	15
2.1.4 Intensity dependence	18
2.2 Optical cavities	19
2.3 Whispering-gallery mode resonators	24
2.3.1 Optical WGMRs	25
2.3.2 WGM spectral properties	26
3 Quantum model of light	30
3.1 Cavity vs. free-space operators	34
3.2 Coherent states	36
3.3 Squeezed light	38
3.4 Quantum noise analysis of WG modes	44
3.4.1 Coherent Equations	46

3.4.2	Fluctuation Equations	47
3.4.3	Experimental variables	49
3.5	Model predictions	53
3.5.1	Undepleted pump approximation	53
3.5.2	Transmitted pump noise analysis	55
4	Whispering-gallery mode resonator experiment	67
4.1	WGMR coupling	68
4.1.1	Prism geometry	69
4.1.2	Coupling mount	71
4.1.3	Temperature control	71
4.2	Experimental setup	73
4.2.1	Equipment	74
4.2.2	CCD camera and scattering detection	75
4.2.3	WGM spectrum	76
4.3	Whispering-gallery mode resonator polishing	77
5	Second harmonic generation inside a WGMR	81
5.1	SHG Experiment	81
5.2	Detection of SHG	84
5.3	Whispering-gallery cavity locking	86
5.3.1	Pump laser frequency locking	87
5.3.2	Electric field tuning	91
5.4	SHG Efficiency measurements	95
6	Quantum noise measurements	98
6.1	Photodetectors	99
6.2	Electronics noise	101

6.3	Laser noise	102
6.4	Shot noise	103
6.5	Experimental results	104
6.5.1	Transmitted pump noise measurements	106
6.5.2	Second harmonic noise measurements	112
7	Hyper-Raman scattering in a WGMR	114
7.1	Raman scattering	114
7.2	Hyper-Raman scattering	116
7.3	HRS in WGMR Experiment	117
8	VO ₂ MIT and Q-switching	123
8.1	Q-switching	123
8.2	VO ₂ metal-insulator phase transition	124
8.2.1	Time-resolved pump-probe reflection measurements	126
8.2.2	CW probe reflection measurements	130
8.2.3	Metallic state decay analysis	131
9	Conclusions and Outlook	135
9.1	Summary of results and limitations	136
9.2	Outlook and potential improvements	139
APPENDIX A		
	Ultrafast laser system	141
	Bibliography	143
	Vita	155

ACKNOWLEDGMENTS

I would like to thank my advisor, Irina Novikova, without whose guidance and patience I would not have been able to arrive at this point. I also thank Eugeny Mikhailov for providing years of advice. Thanks to all of my lab mates over the years - Nate, Travis, Gleb, Ellie, Mi, Bain, David, Nathan, Joe, and all of the others I've worked with in the lab. I have enjoyed working alongside all of you. And thanks to all of the rest of the graduate students who joined me in our multiple award-winning intramural teams and other recreational activities, and helped me retain my sanity. I want to thank my undergraduate advisor Olivier Pfister for introducing me to quantum optics and experimental research. And thank you to all of the other professors and teachers who have given me assistance and advice throughout my undergraduate and graduate career. A special thanks to the U.Va. Reference Room crew - there is no way I would have made it through to graduate school without the countless hours of discussions, encouragement, and entertainment. Lastly I want to thank all of my friends and family, especially my mom, dad, and brother, for all of their support and love, without which none of this would be possible.

I present this thesis in honor of my parents and grandparents, Richard and Beverly Simons, Raymond and Dorothy Simons, and Beverly and Virginia Hudnall.

LIST OF TABLES

2.1	Nonlinear optical properties of lithium niobate	15
2.2	Quality factors for different optical materials	26
3.1	Constraints on independent variables for theory	56
4.1	Refractive indices of prism and disk material used in this dissertation. Values are given for the ordinary (n_o) and extraordinary (n_e) indices of refraction for pump (1064 nm) and second harmonic (532 nm) wave- lengths of light. Diamond is isotropic and has only one index of refraction.	70

LIST OF FIGURES

2.1	Nonlinear generation photo	8
2.2	Photo of second harmonic generation	10
2.3	Schematic of SHG	13
2.4	Birefringent media	14
2.5	Phase-matching curve	18
2.6	Diagram of a two-mirror	19
2.7	Spectrum of a Fabry-Perot	23
2.8	The dome of St. Paul's Cathedral	24
2.9	Lithium niobate WGMR disks	25
2.10	Whispering-gallery mode resonator spectrum	27
3.1	Representation of light in quadrature	39
3.2	Ball-on-stick representation of a laser	40
3.3	Photon schematic of intensity noise reduction	43
3.4	Input/output diagram of WGMR	45
3.5	Output second harmonic generation efficiency versus input pump power	51
3.6	Squeezing vs. detection frequency for the pump field under ideal conditions	57
3.7	Squeezing vs. saturation power (W_0) for the pump field under ideal conditions	58
3.8	Squeezing vs. input pump power (P_{in}) for the pump field under ideal conditions	59

3.9	Squeezing vs. input pump power for three values of saturation power under ideal conditions.	60
3.10	Squeezing vs. quality factor (Q_0) for the pump field under ideal conditions	61
3.11	Squeezing vs. detection frequency for the pump field under realistic conditions	63
3.12	Squeezing vs. saturation power for the pump field under realistic conditions	64
3.13	Squeezing vs. input pump power for the pump field under realistic conditions	65
3.14	Squeezing vs. Q_0 for the pump field under realistic conditions	66
4.1	Waveguide coupling diagram	69
4.2	Technical drawings of mount	72
4.3	Mount holding prism and WGMR	72
4.4	Temperature controller schematic	73
4.5	Experimental schematic for WGMR coupling	74
4.6	WGM rim scattering	76
4.7	Transmission spectrum from LiNbO_3 WGMR	77
4.8	LiNbO_3 disk mounted in lathe	78
4.9	Side view of WGMR disk with indices of refraction	78
4.10	Two polishing stages.	79
4.11	Single WGM resonance	80
5.1	Schematic for second harmonic generation experiment	82
5.2	Photo of WGMR with and without SHG.	83

5.3	Photo of SHG from the WGMR	83
5.4	WGMR output with SHG vs. pump laser detuning.	85
5.5	Photo of different WGMR spatial modes	86
5.6	Feedback schematic for WGMR cavity	87
5.7	PI control schematic	88
5.8	SHG from WGMR while pump is locked.	89
5.9	SHG from WGMR before pump lock is lost.	90
5.10	SHG output vs. E-field detuning	94
5.11	Saturation power measurements by way of SHG Efficiency vs. input power.	96
6.1	Photodetector schematic	100
6.2	Pump laser noise with and without noise eater.	103
6.3	Spectrum analyzer traces showing 3 dB	105
6.4	Optical schematic for pump noise	105
6.5	Predicted pump noise variation as a function of saturation power	106
6.6	Extra noise in pump with SHG while pump was locked.	108
6.7	Pump noise measurement with strong SHG and extra noise	109
6.8	Example of second harmonic mode overlap	110
6.9	Pump noise measurement at 5.5 MHz	111
6.10	Optical schematic for SH noise	112
7.1	Raman scattering diagram	115
7.2	Schematics of hyper-Raman scattering	117

7.3	HRS experiment schematic	118
7.4	Output spectra of HRS emission	120
7.5	Wavelength shift for (<i>Top</i>) Raman scattering of 785 nm from a lithium niobate	121
8.1	VO ₂ has an insulating monoclinic structure	125
8.2	An ultrafast pulse can cause a phase transition in VO ₂	126
8.3	Photos of VO ₂ on rutile and sapphire	127
8.4	VO ₂ pump-probe with ultrafast probe	127
8.5	Pump-probe measurements of VO ₂	129
8.6	VO ₂ pump - CW probe experimental diagram	130
8.7	CW pump-probe measurements of VO ₂ on rutile	131
8.8	Metallic state relaxation time constant τ vs. pump fluence	132
8.9	Various substrate temperatures for the metallic state relaxation constant τ	133
A.1	Coherent Legend system schematic	142

WHISPERING-GALLERY MODE RESONATORS FOR NONLINEAR AND
QUANTUM OPTICAL APPLICATIONS

CHAPTER 1

Introduction

Quantum information is the next revolution in computation and communication. Many systems are being studied for their application as building blocks in a quantum information network. One of the central obstacles in this effort is decoherence of a quantum state as it interacts with its environment. Light can exhibit coherence over long distances, and provides a natural medium for communication. Thus the field of quantum optics is integral to the development of quantum communication technology.

Single-photon states are one type of quantum optical state. These are inherently nonclassical, and so possess the necessary properties for quantum information encoding and transport. However, they require extremely sensitive single-photon detection schemes. Another type of nonclassical state is squeezed light. These states can exist with large numbers of photons, and can be detected reliably through a variety of techniques. They have been used to demonstrate continuous-variable entanglement and quantum teleportation [1–5]. They can also be used to improve optical interferometers, such as in magnetometers [6] and in gravitational wave detection [7–10].

Squeezed states can be generated through a variety of processes including polarization self-rotation in a ^{87}Rb vapor (PSR), the Kerr effect, and optical nonlinear processes such as second harmonic generation (SHG) [11–18], optical parametric oscillation (OPO) [19–25], and four-wave mixing (FWM) [26–28]. PSR has been used to generate squeezed vacuum states [29–31], however this is restricted to the wavelengths corresponding to Rb transitions. OPO and FWM have produced vacuum and bright (non-vacuum) squeezed light. These processes are complex, requiring first the generation of multiple fields.

A compact, low-power source of squeezed light will be necessary to realize a future quantum communication infrastructure. The nonlinear processes described above are intensity dependent, and can require significant input power to achieve efficient nonlinear conversion and squeezing. Placing the nonlinear medium inside a cavity can greatly reduce the input power requirements, but this can add to the complexity and size of the system. Recently, whispering-gallery mode resonators (WGMRs), a type of monolithic optical cavity, have demonstrated significant advantages in a variety of optical applications. These include microlasers [32–37], biological sensors [38–42], electro-optic filters, efficient nonlinear conversion [43, 44]. In particular, a significant increase in the efficiency of second harmonic generation at low input power has been demonstrated using WGMRs [43, 45]. Thus can squeezed light be generated with very low input power using the advantages of efficient second harmonic generation in a WGMR?

We start this dissertation with a review of second harmonic generation and nonlinear optics, and a discussion of optical cavities and the properties of optical WGMRs. The next chapter discusses squeezed light, after a review of the quantization of the electromagnetic field. A quantum model of the propagation of light through a WGMR under the conditions of SHG is detailed, and the predictions of noise reduction are

given. In the next chapter, the WGMR apparatus and experimental procedures are explained. The following chapter describes the experimental realization of SHG from the WGMR. The next chapter details the experiments to detect the noise in the light transmitted from the WGMR. The next chapter contains the observation of another nonlinear phenomenon, hyper-Raman scattering, observed inside our WGMRs. Lastly, we examine the properties of the vanadium dioxide metal-insulator phase transition in relation to the application to ultrafast optical switching.

CHAPTER 2

Nonlinear optics and cavities

Propagation of light is described by solutions to Maxwell's equations [46, 47]

$$\nabla \cdot \vec{D} = 4\pi\rho \quad (2.1)$$

$$\nabla \cdot \vec{B} = 0 \quad (2.2)$$

$$\nabla \times \vec{E} = -\frac{1}{c} \frac{\partial \vec{B}}{\partial t} \quad (2.3)$$

$$\nabla \times \vec{H} = \frac{1}{c} \frac{\partial \vec{D}}{\partial t} + \frac{4\pi}{c} \vec{J} \quad (2.4)$$

where \vec{E} is the electric field, \vec{B} is the magnetic field, \vec{D} is the electric displacement field, \vec{H} is the magnetic auxiliary field, ρ is the free charge density, \vec{J} is the free current density, and c is the speed of light. We will consider solutions where there are no free charges, currents, or magnetic material, so

$$\rho = 0 \quad (2.5)$$

$$\vec{J} = 0 \quad (2.6)$$

$$\vec{B} = \vec{H} \quad (2.7)$$

Assuming propagation through a medium with polarization \vec{P} , the displacement and electric fields are related by

$$\vec{D} = \vec{E} + 4\pi\vec{P} \quad (2.8)$$

By taking the curl of \vec{E} and using equations 2.1–2.4, we arrive at

$$\nabla \times \nabla \times \vec{E} + \frac{1}{c} \frac{\partial^2}{\partial t^2} \vec{E} = -\frac{4\pi}{c^2} \frac{\partial^2 \vec{P}}{\partial t^2} \quad (2.9)$$

The vector calculus identity $\nabla \times \nabla \times \vec{E} = \nabla (\nabla \cdot \vec{E}) - \nabla^2 \vec{E}$ is used to simplify Equation 2.9. In linear, isotropic material $\nabla \cdot \vec{E} = 0$, while in nonlinear media this is not always true. However this term can be shown to be much smaller than the other term in Eq. 2.9 [48]. Then Eq.2.9 becomes

$$-\nabla^2 \vec{E} + \frac{1}{c} \frac{\partial^2}{\partial t^2} \vec{E} = -\frac{4\pi}{c^2} \frac{\partial^2 \vec{P}}{\partial t^2} \quad (2.10)$$

In the following sections we will assume there is an input laser field generated absent a nonlinear medium, such that $\vec{D} = \vec{E}$. We then take solutions of the free-space

wave equation

$$-\nabla^2 \vec{E} + \frac{1}{c} \frac{\partial^2}{\partial t^2} \vec{E} = 0 \quad (2.11)$$

of the form

$$\vec{E}(\vec{r}, t) = \hat{E}_0 e^{\vec{k} \cdot \vec{r} - \omega t} + c.c. \quad (2.12)$$

as the equation for a plane-wave of light, where E_0 is the amplitude, \hat{r} is the unit vector in the direction of propagation, ω is the frequency and \vec{k} is the wavevector.

2.1 Nonlinear optics

The development of the laser in the 1960's led to amazing advances in a nearly every field of physics. The field of experimental nonlinear optics would have been very difficult to pursue without it. Nonlinear optics encompasses phenomena that result from the electromagnetic response of a medium to an optical field, where the response has a nonlinear relationship to the applied electromagnetic wave. This includes a broad range of processes, and generally involves the creation of fields at frequencies different than the original frequency (The photo in Figure 2.1 is an example of frequency conversion).

When an incident electromagnetic wave $E(\omega)$ (which will be referred to as the *fundamental* or *pump*) enters a medium, the polarization $P(\omega)$ (dipole moment per unit volume) of the medium will depends on the incident wave [48, 49]:

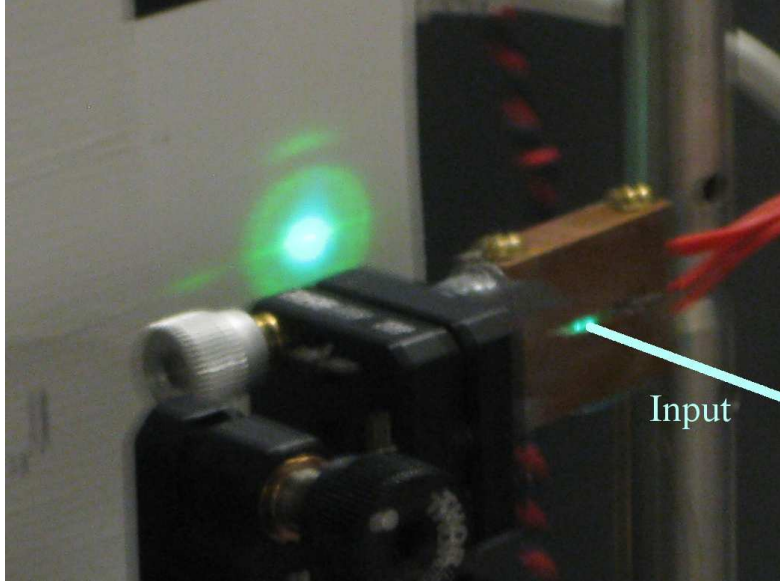


FIG. 2.1: Nonlinear generation photo using an ultrafast pump. Line *Input* is drawn to show direction of input pulses.

$$\vec{P}_i(\omega) = \epsilon_0 (1 + \chi_{ij}) \cdot \vec{E}_j(\omega) \quad (2.13)$$

where χ_{ij} is the susceptibility tensor of the medium. The electric field and polarization are vectors.

$$\vec{E} = E_1 \hat{x} + E_2 \hat{y} + E_3 \hat{z} \quad (2.14)$$

$$\vec{P} = P_1 \hat{x} + P_2 \hat{y} + P_3 \hat{z} \quad (2.15)$$

The electrons in the medium cannot follow the changing electric field perfectly, and there will in general be some anharmonicity in their response. Therefore the polarization is expanded in powers of the incident electric field [48]:

$$P_i = \sum_{j=1}^3 \chi_{ij}^{(1)} E_j + \sum_{j,k=1}^3 \chi_{ijk}^{(2)} E_j E_k + \sum_{j,k,l=1}^3 \chi_{ijkl}^{(3)} E_j E_k E_l + \dots \quad (2.16)$$

The $\chi^{(1)}$, $\chi^{(2)}$, and $\chi^{(3)}$, etc. are tensors of ascending rank. The first term in Eq. 2.16 is the linear polarization, and the other terms describe the higher-order nonlinear polarization that lead to nonlinear optical phenomena. The second-order susceptibility can lead to the generation of a new optical field with twice the frequency of the incident field. This is known as *second harmonic generation*. The reverse process, where an incident field is converted into two fields with frequencies that sum to the original frequency, is called *parametric down conversion*.

We will focus on the properties of second harmonic generation in Sec. 2.1.1 below. Another type of frequency conversion process that can occur in materials is Raman scattering. Raman scattering is the inelastic scattering of light with matter, where the scattered light either receives or gives up energy to vibrational energy states of molecules. Raman scattering is a linear effect, which depends on $\chi^{(1)}$. Higher-order Raman scattering is also possible, known as *hyper-Raman scattering*. Second-order hyper-Raman scattering, for instance, depends on the second-order nonlinearity. This will be discussed further in Chapter 7.

2.1.1 Second harmonic generation

Second harmonic generation (SHG) is a nonlinear process where energy from a beam of light of a given frequency ω_0 (referred to as the pump or fundamental) is transferred to a new beam of light with twice the frequency $\omega_s = 2\omega_0$ (the second harmonic or SH field) by interaction with a medium with a nonlinear susceptibility

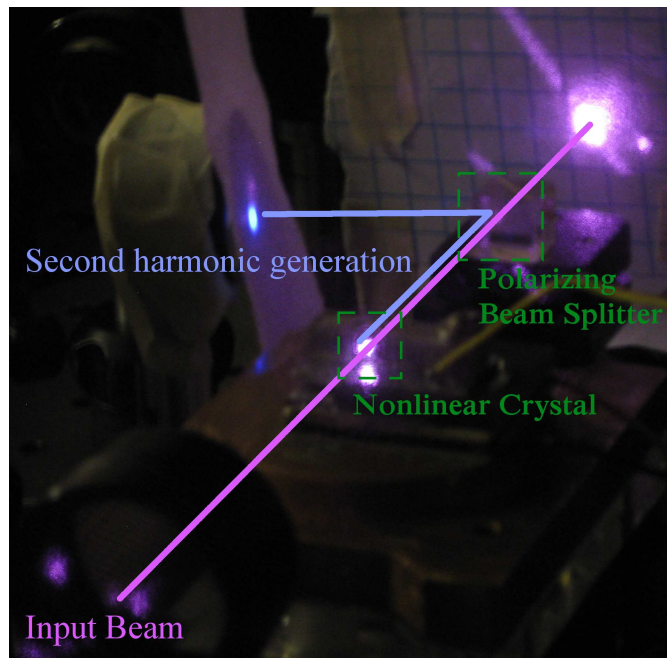


FIG. 2.2: Photo of second harmonic generation from 800 nm to 400 nm in a potassium lithium niobate crystal. Lines are drawn to show beam paths. The purple is the near-infrared pump (800 nm), which is seen as purple by the CCD camera.

(Fig. 2.3). The photo in Figure 2.2 shows an example of second harmonic generation of a 400 nm from an input laser at 800 nm. We consider the input electric field $\vec{E}(\omega_0)$ with linear polarization. First we demonstrate how the field with twice the frequency arises, then we will detail how the nonlinear susceptibility tensor mediates this generation.

To demonstrate how a new field with twice the frequency can arise, we will take a trivial example of a scalar χ , that does not depend of frequency. If the input field is $E_0(\omega_0) = |E_0| \cos \omega_0 t$, then the second-order polarization (P_{nl}) generates an optical field (\vec{E}_{nl}) through Eq. 2.20 (from Eq. 2.16) [48]:

$$E_{nl} = \epsilon P_{nl} \tag{2.17}$$

$$= \epsilon (\chi^{(2)} E_0(\omega_0) E_0(\omega_0)) \tag{2.18}$$

$$= \epsilon \chi^{(2)} |E_0|^2 \cos^2 \omega_0 t \tag{2.19}$$

$$E_{nl} \simeq \frac{1}{2} \epsilon \chi^{(2)} |E_0|^2 \cos(2 \omega_0 t) \tag{2.20}$$

Now the generated field has a component with twice the initial frequency.

The nonlinear susceptibility is a tensor that describes the coupling between the electric field and polarization oscillations in different directions in a medium. It is common to express the susceptibility tensor $\chi_{ijk}^{(2)}$ in terms of the tensor d_{ijk} [48]:

$$d_{ijk} = \frac{1}{2} \chi_{ijk}^{(2)} \tag{2.21}$$

The components of the second-order nonlinear polarization are then expressed as

$$P_i(\omega_s) = \sum_{j,k=1}^3 2 d_{ijk} E_j(\omega_0) E_k(\omega_0) \quad (2.22)$$

We will work with systems where the optical frequencies ω_0 , ω_s are much less than the absorption resonance frequencies of the material (which for optical crystals are typically in the UV range), so that the d_{ijk} is independent of frequency. Physically $E_j(\omega_0)E_k(\omega_0)$ is the same as $E_j(\omega_0)E_k(\omega_0)$ in Equation 2.22. Due to this symmetry, elements d_{ijk} are identical to d_{ikj} , and in practice the tensor is reduced to $d_{ijk} \rightarrow d_{il}$. The index l ranges from 1 – 6, encapsulating the indices j, k as given below.

$$\begin{aligned} j, k &\rightarrow l \\ 1, 1 &\rightarrow 1, \quad 2, 2 \rightarrow 2 \quad 3, 3 \rightarrow 3 \\ 2, 3 \ \& \ 3, 2 \rightarrow 4 \quad 3, 1 \ \& \ 1, 3 \rightarrow 5 \quad 1, 2 \ \& \ 2, 1 \rightarrow 6 \end{aligned} \quad (2.23)$$

The $d_{i,j,k}$ elements are invariant under any permutation of the indices (the Kleinman symmetry condition [48]). For example, the value of d_{211} is identical to the permutation d_{112} , so with the reduction above of $j, k \rightarrow l$ we have the identities $d_{211} \equiv d_{21}$ and $d_{112} \equiv d_{16}$, thus $d_{21} = d_{16}$. This reduces the independent elements further:

$$d_{il} = \begin{bmatrix} d_{11} & d_{12} & d_{13} & d_{14} & d_{15} & d_{16} \\ d_{16} & d_{22} & d_{23} & d_{24} & d_{14} & d_{12} \\ d_{15} & d_{24} & d_{33} & d_{23} & d_{13} & d_{14} \end{bmatrix} \quad (2.24)$$

Equation 2.22 is now re-written as

$$\begin{bmatrix} P_x(\omega_s) \\ P_y(\omega_s) \\ P_z(\omega_s) \end{bmatrix} = 2 \begin{bmatrix} d_{11} & d_{12} & d_{13} & d_{14} & d_{15} & d_{16} \\ d_{16} & d_{22} & d_{23} & d_{24} & d_{14} & d_{12} \\ d_{15} & d_{24} & d_{33} & d_{23} & d_{13} & d_{14} \end{bmatrix} \begin{bmatrix} E_x(\omega_0)^2 \\ E_y(\omega_0)^2 \\ E_z(\omega_0)^2 \\ E_y(\omega_0)E_z(\omega_0) \\ E_x(\omega_0)E_z(\omega_0) \\ E_x(\omega_0)E_y(\omega_0) \end{bmatrix} \quad (2.25)$$

This is general for second harmonic generation. Crystals are often used for SHG. Different crystal structures have symmetries that determine the specific composition of d_{il} .

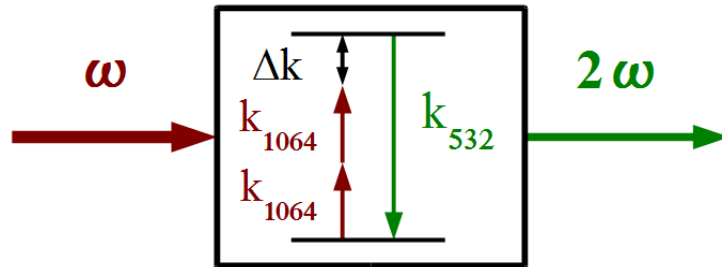


FIG. 2.3: Schematic of SHG inside nonlinear medium. Two photons of incident field (ω) combine into one photon with doubled frequency (2ω). Δk is the phase mismatch between the pump and SH fields.

2.1.2 Nonlinear crystals

Optical crystals provide a useful medium for producing nonlinear effects such as SHG as they are transparent to the optical spectrum and can have non-zero nonlinear tensors. The $\chi^{(2)}$ tensor is non-zero only in acentric crystals [50] – SHG is not feasible in centrosymmetric crystals. These crystals have inversion symmetry and

thus a center of inversion [48]. Uniaxial crystals have two distinct indices of refraction, an ordinary index (n_o) that is degenerate in two directions, and an orthogonal extraordinary index (n_e). Figure 2.4 shows a diagram of a uniaxial crystal.

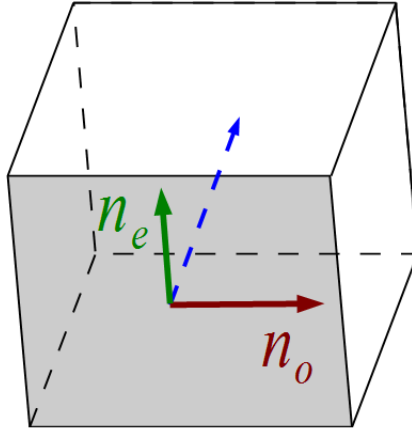


FIG. 2.4: Birefringent media have two distinct indices of refraction. The ordinary index of refraction (n_o) has two degenerate directions (red and blue arrows), and the extraordinary index has one direct perpendicular to the ordinary plane.

The choice of medium depends on the wavelengths of interest (as explained in Sec. 2.1.3). We used lithium niobate for our WGMR material because it is a uniaxial crystal that can phase-match second harmonic generation from 1064 nm to 532 nm by varying the temperature. We used several LiNbO_3 wafers with different stoichiometries: congruent LiNbO_3 (Nb rich), stoichiometric LiNbO_3 (equal parts Li and Nb), and magnesium oxide-doped lithium niobate ($\text{MgO}:\text{LiNbO}_3$) [51]. These crystals have different birefringence/dispersion, and therefore different phase-matching temperatures (shown in Table 2.1). Both LiNbO_3 and $\text{MgO}:\text{LiNbO}_3$ are trigonal and in the $3m$ space group. The crystal structure determines the elements and symmetries of the d_{ij} tensor. For the $3m$ group, the d_{ij} tensor is

LiNbO ₃ type:	congruent	stoichiometric	MgO:LiNbO ₃
Nonlinear coefficient d_{31}	-4.4 pm/V	-4.6 pm/V	-4.9 pm/V [†]
NCPM Temperature * (1064 nm – 532 nm)	-6°C	140°C	110°C

TABLE 2.1: Nonlinear optical properties of lithium niobate (LiNbO₃) in different compositions – congruent (Nb > Li), stoichiometric (Nb = Li) [50], and magnesium oxide doped [†][53]. * – our measurements.

$$d_{il} = \begin{bmatrix} 0 & 0 & 0 & 0 & d_{31} & -d_{22} \\ -d_{22} & d_{22} & 0 & d_{31} & 0 & 0 \\ d_{31} & d_{31} & d_{33} & 0 & 0 & 0 \end{bmatrix} \quad (2.26)$$

As we are investigating conversion from $E_1(\omega_0) \rightarrow E_3(\omega_s)$, we are interested in the values of the d_{31} element (Table 2.1). The indices of refraction of both LiNbO₃ and MgO:LiNbO₃ are similar, though the birefringence/dispersion is different. Therefore they have different phase-matching temperatures for a given pump wavelength. The MgO:LiNbO₃ is less susceptible to photorefractive damage [52], which is important as the WGMRs can build up very high intensities inside the crystal. The nonlinear coefficients d_{31} and phase-matching temperatures for these different crystals are in Table 2.1.

2.1.3 Phase-matching

Second harmonic generation must obey energy and momentum conservation. Energy conservation is met through the conversion of two photons of fundamental frequency ω_f into one photon of higher (second harmonic) frequency ω_s :

$$\omega_s = \omega_f + \omega_f = 2\omega_f \quad (2.27)$$

Momentum conservation occurs when the wavevectors of the fundamental field (\vec{k}_f) sum to the wavevector of the second harmonic frequency (\vec{k}_s):

$$\vec{k}_s = \vec{k}_f + \vec{k}_f \quad (2.28)$$

where $|\vec{k}_i| = \frac{\omega_i n(\omega_i)}{c}$, c is the speed of light, and n is the index of refraction. The momentum conservation condition is typically difficult to satisfy in ordinary materials due to dispersion. The different indices of refraction for different wavelengths lead to a phase shift of the generated frequency, ultimately preventing significant generation. The phase mismatch Δk :

$$\Delta\vec{k} = \vec{k}_{2f} - (\vec{k}_f + \vec{k}_f) \quad (2.29)$$

can be reduced through various mechanisms in different media, a process referred to as phase-matching. Crystals are useful systems for these processes when they have low optical absorption, as their regular structure allows for consistent dispersion compensation. We will focus on phase-matching in crystals. In some media, non-collinear wavevectors will sum to zero at a particular angle. This is referred to as *critical phase-matching* [50].

Another method of phase-matching flips the crystal domains periodically, thus inverting the phase of the generated light to match phase of light generated in the pre-

vious domain. This is called *quasi-phase-matching* [50]. In this method the wavevectors are typically collinear. Not all of the generated light will be phase-matched, so while it allows nonlinear generation in crystals where other phase-matching methods are not possible, it is not as efficient.

In anisotropic crystals (Figure 2.4), the birefringence can be tuned (using temperature or a DC electric field) to exactly cancel the dispersion, with the fundamental and second harmonic fields collinear. This is called *non-critical phase-matching* [50]. The pump field is polarized along one crystal axis (we will use the ordinary axis), and the generated second harmonic is polarized along an orthogonal direction with a different index (in our case the extraordinary axis). The temperature can be tuned to change the birefringence, and the phase mismatch between pump and SH fields is expressed as a function of refractive index:

$$\Delta k = |k_s| - 2|k_f| = \frac{2\omega_f}{c} (n(\omega_s, T) - n(\omega_f, T)) \quad (2.30)$$

The index of refraction is a function of temperature T and frequency ω . An example of non-critical phase-matching is shown in the plot in Figure 2.5. The ordinary and extraordinary refractive indices of lithium niobate are plotted versus temperature for 1064 nm and 532 nm wavelengths of light, respectively. The ordinary refractive index varies less than the extraordinary index with temperature. At a particular temperature (T_{pm}), the indices $n_o(1064 \text{ nm}, T_{pm}) = n_e(532 \text{ nm}, T_{pm})$ are equal. If the pump 1064 nm field is polarized along the ordinary axis, then the second harmonic 532 nm field will be generated with a polarization along the extraordinary axis, with a phase mismatch of $\Delta k = 0$ (Eq. 2.30).

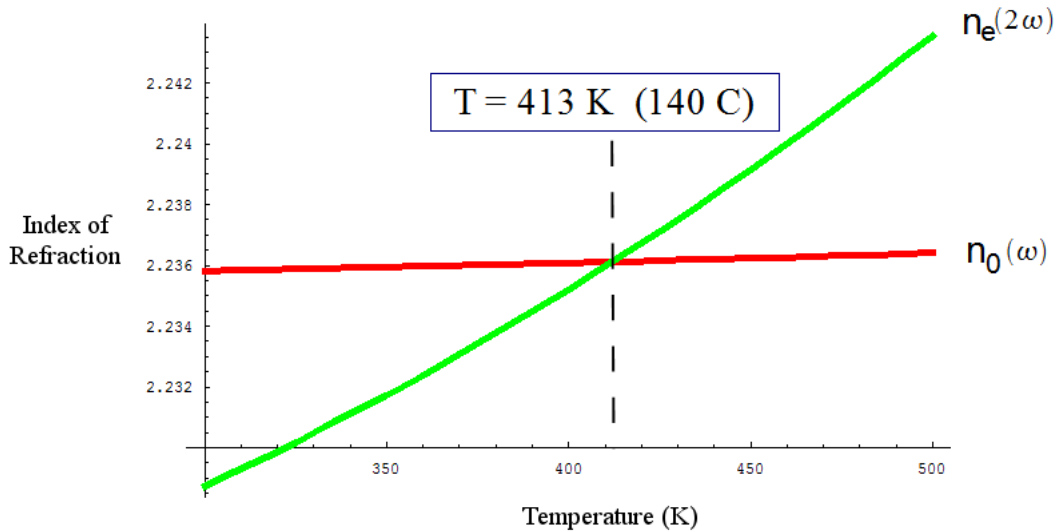


FIG. 2.5: Phase-matching curve for non-critical phase-matching in lithium niobate. The ordinary (n_0) and extraordinary (n_e) indices of refraction depend differently on temperature. The phase mismatch (ΔK) is minimized when $n_o(1064 \text{ nm}) = n_e(532 \text{ nm})$, which is at $T_c = 140 \text{ }^\circ\text{C}$ in LiNbO_3 .

2.1.4 Intensity dependence

As SHG couples the pump and generated field through the second-order electric field, it depends on the intensity of the incident field. The $\chi^{(2)}$ coefficient is typically small, so a very high intensity field is required for significant conversion. The first experimental observation of SHG, by a single-pass through a potassium dihydrogen phosphate (KDP) crystal, was famously omitted from the PRL article because the SHG in the photo was so small it appeared to be a stray spot [54].

One solution to this problem is to simply increase the power of the pump field. However this can be inefficient as it may be difficult to produce a sufficiently powerful fundamental field, it is more difficult to separate the left-over fundamental light, and the high-power can damage the crystal. Another solution is to compress the field temporally by using an ultrafast pulse [48]. This method has been useful for

producing many nonlinear optical effects (see Fig. 2.1). However this method has similar drawbacks to the first solution.

Another solution is to increase the conversion efficiency using an optical cavity. The cavity confines the field and allows the intensity to build up. By placing the nonlinear crystal inside the cavity, the increased intensity lowers the input power required for nonlinear conversion [55].

Nonlinear conversion inside optical cavities improve conversion efficiency and can thus improve the effects of conversion, such as quantum noise reduction. We explore using a type of monolithic cavity, a whispering-gallery mode resonator (WGMR), for the generation of squeezed states of light.

2.2 Optical cavities

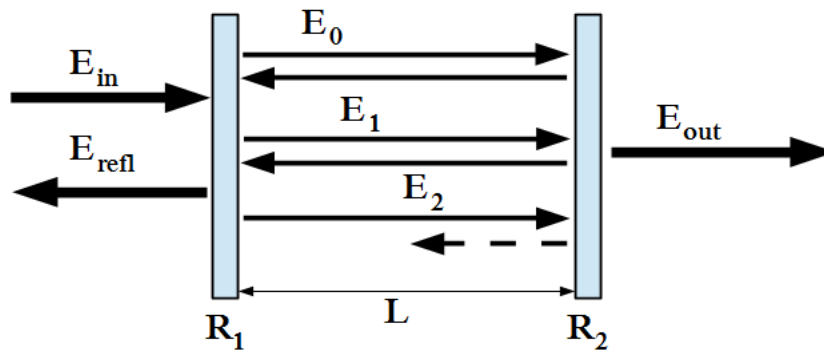


FIG. 2.6: Diagram of a two-mirror cavity.

Optical cavities serve a range of important roles in optical systems. The simplest model of an ideal optical cavity is two mirrors with reflectance R_1 and R_2 separated by a distance L (Figure 2.6). Transmission through the mirrors is related to the reflectance by $T = 1 - R$.

Now we put an input field \vec{E}_{in} incident on the input mirror. There will be a reflected beam $\vec{E}_r = \sqrt{R_1} \times \vec{E}_{in}$ outside and a field transmitted inside the cavity $\vec{E}_0 = \sqrt{1 - R_1} \times \vec{E}_{in}$. This intracavity field reflects off of mirror R_2 and makes a round-trip back to the input mirror. The intracavity field again reflects off of mirror R_1 and is now $\vec{E}_1 = \sqrt{R_1 R_2} \times \vec{E}_0$.

Realistically the field will encounter loss per unit length α as it travels through the cavity due to absorption in the cavity material, transmission through the mirrors, and diffractive losses transverse to the cavity. Then the intensity remaining after each round trip will be $e^{-\alpha p}$. Here p is the optical path length of the cavity, which is the physical path length multiplied by the index of refraction n (in this model $p = 2Ln$). Now the field after one round-trip, \vec{E}_1 , is

$$\vec{E}_1 = \sqrt{R_1 R_2 e^{-\alpha p}} \times \vec{E}_0 = g \times \vec{E}_0 \quad (2.31)$$

where $g = \sqrt{R_1 R_2 e^{-\alpha p}}$. This process continues and expressions for $\vec{E}_2, \vec{E}_3, \dots$ can be similarly written. As we assume the input is a continuous field, we sum these to obtain an expression for the total intracavity field \vec{E}_{cav} :

$$\vec{E}_{cav} = \vec{E}_0 + \vec{E}_1 + \vec{E}_2 + \vec{E}_3 + \dots \quad (2.32)$$

$$\vec{E}_{cav} = \vec{E}_0 (1 + g + g^2 + g^3 + \dots) \quad (2.33)$$

$$= \frac{\vec{E}_0}{(1 - g)} \quad (2.34)$$

Light that travels through the cavity undergoes a phase shift

$$\delta\phi = 2\pi(\Delta\nu)\frac{p}{c} \quad (2.35)$$

due to reflection off of the mirrors and the distance propagated (where $\Delta\nu = \nu_{in} - \nu_{cav}$). Only fields with frequencies that constructively interfere after a round trip through cavity can survive to build-up power. The interference condition (Eq. 2.35) defines the allowed frequencies (ν_{cav}) to be integer multiples (m_{opt}) of the fundamental frequency allowed (Eq. 2.36).

$$\nu_{cav} = m_{opt}\frac{c}{p} \quad (2.36)$$

The distance in frequency between adjacent modes is defined as the free-spectral range (FSR), Eq. 2.37.

$$FSR = \frac{c}{p} \quad (2.37)$$

With the phase shift per round trip included, Eq. 2.34 becomes:

$$\vec{E}_{cav} = \frac{\vec{E}_0}{(1 - ge^{-i\delta\phi})} \quad (2.38)$$

$$= \frac{\sqrt{T_1}\vec{E}_{in}}{(1 - ge^{-i\delta\phi})} \quad (2.39)$$

The power inside the cavity is given by Eq. 2.40.

$$P_{cav} \propto |E_{cav}|^2 = \frac{T_1 |E_{in}|^2}{|1 - g e^{-i\delta\phi}|^2} \quad (2.40)$$

$$= \frac{T_1 |E_{in}|^2}{(1 - g)^2 + 4g \sin^2(\delta\phi/2)} \quad (2.41)$$

The frequency dependence in Equation 2.41 can be separated out:

$$P_{cav} \propto \left(\frac{T_1 |E_{in}|^2}{(1 - g)^2} \right) \frac{1}{1 + (2F/\pi)^2 \sin^2(\delta\phi/2)} \quad (2.42)$$

where $F = \frac{\pi\sqrt{g}}{1-g}$ is the *finesse*, a measure of the potential power build-up. Figure 2.7 shows the effect of finesse on the cavity spectrum. The maximum power P_{max} is equal to the first term in Eq. 2.42, $P_{max} = \frac{T_1 |E_{in}|^2}{(1-g)^2}$. The finesse can be measured by $F = \frac{FSR}{FWHM}$.

The family of modes described above by the FSR are the longitudinal modes. There are also a set of transverse modes, defined by the different transverse paths that can be taken through the cavity, referred to as spatial modes. It is typically desired to couple to the fundamental transverse mode, though multiple spatial modes are often excited. To reduce loss into other spatial modes, the input field must be shaped to match the desired spatial mode, a process called mode-matching.

Another important measure of the cavity is the *quality factor*, or Q-factor. The Q-factor is defined as the ratio of energy stored to energy lost per round trip $Q \equiv 2\pi \times (\text{energy stored})/(\text{energy lost})$. The ratio of energy stored to energy lost is equal to the light frequency ν times the lifetime of a photon in the cavity τ , so $Q = 2\pi\nu\tau$ [56]. The lifetime τ is related to the full-width at half-max *FWHM* of the cavity resonance by $\tau = \frac{1}{2\pi FWHM}$. For example, with a 1 μm wavelength laser,

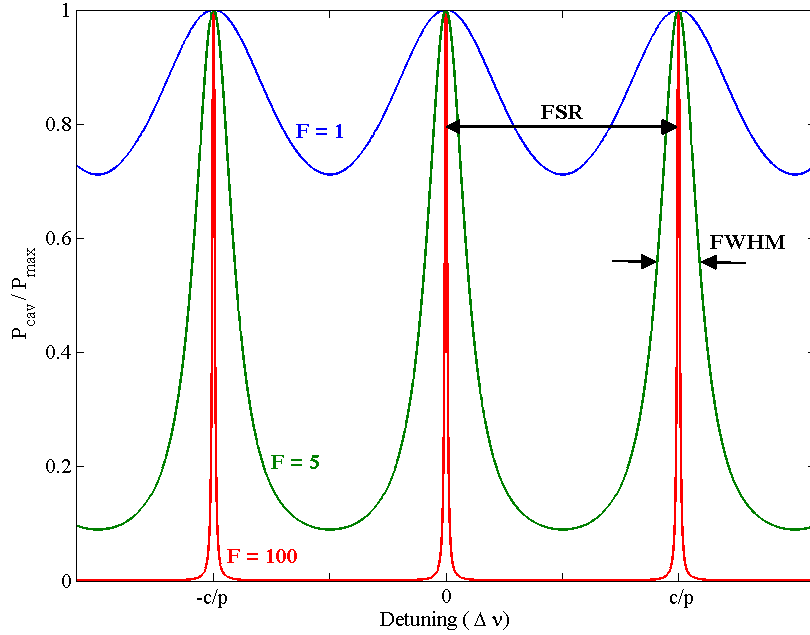


FIG. 2.7: Spectrum of a Fabry-Perot cavity.

a quality factor of $Q = 10^8$ corresponds to a photon lifetime of about 50 ns, and in a 1 cm cavity corresponds to about 1500 passes through the cavity. Q-factor can be measured experimentally by measuring the full-width at half-max of the cavity mode resonance with a laser of frequency ν :

$$Q = \frac{\nu}{FWHM} \quad (2.43)$$

High quality factors can be achieved in two-mirror cavities using mirrors with very high reflectivity. With such high reflectivity ($R > 0.999998$) [57], it is difficult to couple light into the cavity (because the corresponding transmission is so low), and they must often be enclosed inside many layers of material to maintain stability.

A different type of cavity, a whispering-gallery mode resonator, uses total internal reflection to achieve very high quality factors, and waveguide coupling techniques to more easily couple light into the cavity.

2.3 Whispering-gallery mode resonators

Whispering-gallery mode resonators borrow their name from the architectural phenomenon of whispering galleries, where a whisper can be heard at any point along a circular wall. The first study of this effect was done by Lord Rayleigh in St. Paul's Cathedral in London in the late 19th century [58, 59] (Figure 2.8). The frequencies of sound waves that can propagate in this manner are determined by the geometry of the gallery.



FIG. 2.8: The dome of St. Paul's Cathedral contains perhaps the most famous whispering gallery.

Optical whispering-gallery mode resonators are based on this idea, instead using a curved surface in an optically-transparent material with a high index of refraction to create total internal reflection.



FIG. 2.9: Lithium niobate WGMR disks were ~ 7 mm in diameter and 1 mm thick. *Left:* Disk mounted on brass post for polishing. *Right:* Disk mounted in apparatus for prism coupling.

2.3.1 Optical WGMRs

Whispering-gallery mode resonators have been made from a variety of different materials in different configurations. WGMRs have been made from amorphous materials (fused silica droplets), isotropic optical crystals such as calcium fluoride (CaF_2) and magnesium fluoride (MgF_2), nonlinear optical crystals such as lithium niobate (LiNbO_3 , Figure 2.9) and beta barium borate (BBO), IR waveguide material such as Si, as well as other materials such as polymethylmethacrylate (PMMA) [60]. They are used in many applications, ranging over laser cavities, biological and environmental sensors, electro-optic modulators, and optical switches [61–63].

Whispering-gallery mode resonators have many properties that make them advantageous over traditional cavity designs. Fundamentally, they rely on total internal reflection to form the cavity, which creates very high reflectivities compared to mirrored cavities. The high reflectivity leads to very high quality factors of $Q > 10^7$, where a high quality two-mirror cavity might have a $Q \sim 10^6$. The quality factor is a function of the surface quality, wavelength, and material absorption. In practice, the surface quality can be improved until the material absorption becomes the limiting factor. Table 2.2 shows Q -factor limits (both theoretical and experimental) for some typical WGMR materials.

Material	Q -factor (theoretical)	Q -factor (experimental)
CaF ₂	$\sim 10^{12}$	2×10^{10}
fused silica	0.9×10^{10}	0.8×10^{10}
sapphire	$\sim 10^{10}$	$\sim 1 \times 10^9$
LiNbO ₃	$\sim 10^8$	2×10^8

TABLE 2.2: Quality factors for different optical materials typically used for WGMRs, including CaF₂ [64], fused silica [65, 66], sapphire [64, 67], and LiNbO₃ [64],[experimental value in this work]. Theoretical limits are based on material absorption coefficients.

Whispering-gallery mode resonators have several other advantageous features. Coupling to a WGM requires waveguide coupling techniques. As opposed to a cavity that uses an input/output coupling mirror, where the coupling rate is physically fixed, the coupling rate to a WGMR can be controlled. Whispering-gallery mode resonators also have a small mode volume along the entire length of the cavity. This allows a much longer length where the intensity is a maximum. With a high quality factor and small mode volume the intensity can build-up several orders of magnitude compared to the input.

2.3.2 WGM spectral properties

Figure 2.10 shows the transmission from a whispering-gallery cavity for different frequencies. Compared with the one-dimensional cavity of Figure 2.7, a “forest” of many different spatial modes is visible. The modal frequencies are influenced by the boundary conditions of the shape of the resonator. The frequencies have been derived for a sphere in [68] from the solutions to the scattering of electromagnetic waves from a dielectric sphere (Mie scattering). Equations for the electric field inside a dielectric sphere are solutions to Equation 2.9 of the form [43, 47, 69]:

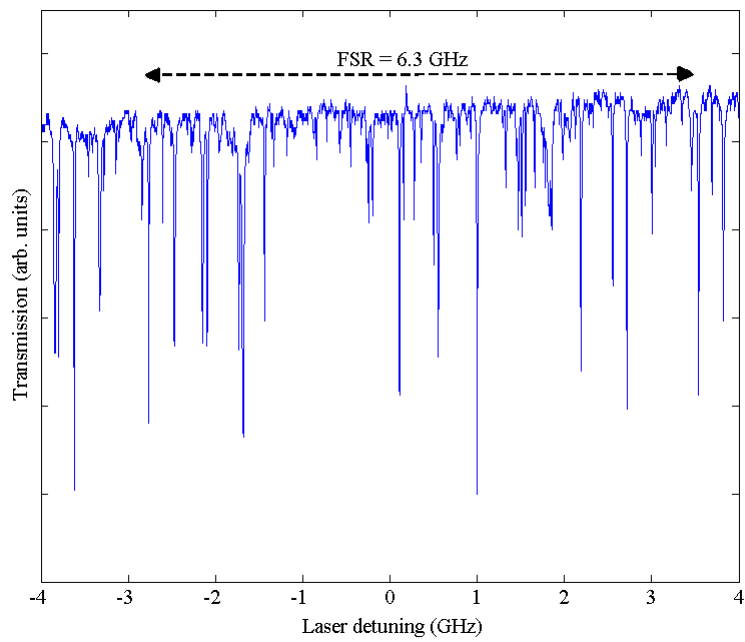


FIG. 2.10: Whispering-gallery mode resonator spectrum from a LiNbO₃ disk. Laser frequency is swept through one free spectral range of the cavity. Many different modes within one FSR are visible.

$$E_{lmi}(r, \theta, \phi) = E_0 Y_{lm}(\theta, \phi) j_l(k_l r) \quad (2.44)$$

where $Y_{lm}(\theta, \phi)$ are spherical harmonics describing the angular dependence, $j_l(k_l r)$ are spherical Bessel functions that give the radial dependence, and modes are indexed by radial mode number i and orbital and azimuthal mode numbers l, m .

The cavity the modes can be split into two polarizations – transverse electric modes (TE) where $\vec{r} \cdot \vec{E} = 0$, and transverse magnetic (TM) modes where $\vec{r} \cdot \vec{H} = 0$ [47, 69]. These frequencies can be expressed (for a sphere of radius R and $l \sim m$) as:

$$f_{i,l} = \frac{x_{i,l} c}{2 \pi R} \quad (2.45)$$

The parameter $x_{i,l}$ is a mode size parameter, which is derived in [68] and approximated by Eqs. 2.46, 2.47 for TE and TM modes, respectively:

$$n(\lambda) x_{i,l} \cong \left(l + \frac{1}{2} \right) + \alpha_i \left(\frac{l + \frac{1}{2}}{2} \right)^{1/3} + \frac{3\alpha_i^2}{20} \left(\frac{2}{l + \frac{1}{2}} \right)^{1/3} - \sqrt{\frac{n^2(\lambda)}{n^2(\lambda) - 1}} \quad (2.46)$$

$$n(\lambda) x_{i,l} \cong \left(l + \frac{1}{2} \right) + \alpha_i \left(\frac{l + \frac{1}{2}}{2} \right)^{1/3} + \frac{3\alpha_i^2}{20} \left(\frac{2}{l + \frac{1}{2}} \right)^{1/3} - \frac{1}{n(\lambda) (n^2(\lambda) - 1)^{1/2}} \quad (2.47)$$

where α_i are the roots of the Airy function and $n(\lambda)$ is the wavelength dependent index of refraction. For a spherical resonator, the frequencies for modes $m \neq l$ are degenerate. However, for resonators that deviate from a sphere, the degeneracy is broken, giving rise to a multitude of resonant frequencies for a given l [63, 70], (as seen in Fig. 2.10). These frequencies f_{lm} are approximated as a function of the amount of deviation of the minor axis from a sphere Δa [63]:

$$f_{lm} \simeq f_l \left[1 - \frac{\Delta a}{R} \left(2 + 3 \frac{l^2 - m^2}{l^2} \right) \right] \quad (2.48)$$

While it is possible to approximate these frequencies by Eq. 2.48, this requires accurate knowledge of the resonator shape, which is not always available. This makes identifying the observed modes difficult [70]. The relationship of the wavevectors of the modes to the cavity geometry change the phase-matching relationship from that of Eq. 2.30, which alters the phase-matching temperature for different pairs of pump and second harmonic modes, as will be seen in Chapter 5.

CHAPTER 3

Quantum model of light

To study the quantum mechanical properties of light, we must first quantize the electromagnetic fields. This procedure is similar to the second quantization of matter.

We begin with the vector potential of the electro-magnetic field $\vec{\mathcal{A}}$, and consider solutions to the wave equation (Eq. 3.1) [71].

$$\nabla^2 \vec{\mathcal{A}} - \frac{1}{c^2} \frac{\partial^2 \vec{\mathcal{A}}}{\partial t^2} = 0 \quad (3.1)$$

The vector potential is related to the electric (\vec{E}) and magnetic (\vec{B}) fields by Equations 3.2, 3.3.

$$\vec{B} = \nabla \times \vec{\mathcal{A}} \quad (3.2)$$

$$\vec{E} = -\frac{\partial}{\partial t} \vec{\mathcal{A}} \quad (3.3)$$

The spatial and temporal functions can be separated, and we use a spatial solu-

tion of the form in Eq. 3.4

$$\vec{\mathcal{A}}(\mathbf{r}, t) = \sum_j \left[\vec{\mathcal{A}}_k(t) e^{i\mathbf{k}\cdot\mathbf{r}} + \vec{\mathcal{A}}_k^*(t) e^{-i\mathbf{k}\cdot\mathbf{r}} \right] \quad (3.4)$$

If we consider a volume $V = L^3$, then \mathbf{k} are the normal modes that satisfy the periodic boundary conditions in Eq. 3.5 (where the m are integers).

$$k_x = \frac{2\pi}{L} m_x, \quad k_y = \frac{2\pi}{L} m_y, \quad k_z = \frac{2\pi}{L} m_z \quad (3.5)$$

We choose the Coulomb gauge (Eq. 3.6), so the temporal equation will take the form of Equation 3.7 [71], where the normal mode frequencies ω_k will be related to the mode wavevectors by $\omega_k = ck$.

$$\nabla \cdot \vec{\mathcal{A}} = 0, \quad \mathbf{k} \cdot \vec{\mathcal{A}}_k(t) = 0 \quad (3.6)$$

$$\frac{\partial^2 \vec{\mathcal{A}}}{\partial t^2} + \omega_j^2 \vec{\mathcal{A}}_k = 0, \quad \omega_k = ck \quad (3.7)$$

The solutions for the vector potential, as well as the electric and magnetic fields, are then given by:

$$\vec{\mathcal{A}}_k(t) = \vec{\mathcal{A}}_k e^{-i\omega_j t} \quad (3.8)$$

$$\vec{E}_k = i\omega_k \left[\vec{\mathcal{A}}_k e^{-i\omega_k t + i\mathbf{k}\cdot\mathbf{r}} - \vec{\mathcal{A}}_k^* e^{i\omega_k t - i\mathbf{k}\cdot\mathbf{r}} \right] \quad (3.9)$$

$$\vec{H}_k = i \frac{\mathbf{k}}{\mu_0} \times \left[\vec{\mathcal{A}}_k e^{-i\omega_k t + i\mathbf{k}\cdot\mathbf{r}} - \vec{\mathcal{A}}_k^* e^{i\omega_k t - i\mathbf{k}\cdot\mathbf{r}} \right] \quad (3.10)$$

The equation for the cycle-averaged energy in mode k is Eq. 3.11, which is then transformed into canonical coordinates p, q in Eq. 3.12 by defining $\vec{\mathcal{A}}, \vec{\mathcal{A}}^*$ (with polarization vector $\hat{\epsilon}_k$) as in Eq. 3.13.

$$\begin{aligned} U_k &= \frac{1}{2} \int (\epsilon_0 E_k^2 + \mu_0 H_k^2) dV \\ &= 2\epsilon_0 V \omega_k^2 \vec{\mathcal{A}}_k \cdot \vec{\mathcal{A}}_k^* \end{aligned} \quad (3.11)$$

$$U_k = \frac{1}{2} (p_k^2 + \omega_k^2 q_k^2) \quad (3.12)$$

$$\vec{\mathcal{A}}_k = \frac{(\omega_k q_k + i p_k) \hat{\epsilon}_k}{\sqrt{4\epsilon_0 V \omega_k}}, \quad \vec{\mathcal{A}}_k^* = \frac{(\omega_k q_k - i p_k) \hat{\epsilon}_k}{\sqrt{4\epsilon_0 V \omega_k}} \quad (3.13)$$

This transformation allows us to write an expression for energy under periodic boundary conditions that is equivalent to the simple harmonic oscillator, where each mode \mathbf{k} is an independent oscillator. These modes can be quantized by converting the canonical variables to operators (Eq. 3.14). Following the standard quantization procedure, we introduce the creation and annihilation operators, Equation 3.15.

$$q \rightarrow \hat{q}, \quad p \rightarrow \hat{p}, \quad [\hat{q}_k, \hat{p}_{k'}] = i\hbar \delta_{k,k'} \quad (3.14)$$

$$\hat{a} = \frac{(\omega_k q_k + i p_k)}{\sqrt{2\hbar\omega_k}}, \quad \hat{a}_k^\dagger = \frac{(\omega_k q_k - i p_k)}{\sqrt{2\hbar\omega_k}} \quad (3.15)$$

The energy (Eq. 3.12) can now be written as an operator \hat{H} in terms of $\hat{a}_k, \hat{a}_k^\dagger$ using Eqs. 3.14,3.15, which gives the Hamiltonian:

$$\hat{H} = \hbar\omega_k \left(\hat{a}_k^\dagger \hat{a}_k + \frac{1}{2} \right) \quad (3.16)$$

The field amplitudes are converted to operators (Eq. 3.17) in terms of the creation and annihilation operators.

$$\begin{aligned}\vec{\mathcal{A}}_k &\rightarrow \hat{\mathcal{A}}_k = \sqrt{\frac{\hbar}{2\epsilon_0 V \omega_k}} \hat{a}_k \hat{\epsilon}_k \\ \vec{\mathcal{A}}_k^* &\rightarrow \hat{\mathcal{A}}_k^\dagger = \sqrt{\frac{\hbar}{2\epsilon_0 V \omega_k}} \hat{a}_k^\dagger \hat{\epsilon}_k\end{aligned}\quad (3.17)$$

The vector potential is defined as an operator (Eq. 3.18).

$$\hat{\mathcal{A}}(\mathbf{r}, t) = \sum_k \sqrt{\frac{\hbar}{2\epsilon_0 V \omega_k}} \hat{\epsilon}_k \left[\hat{a}_k e^{-i\omega_k t + i\mathbf{k}_k \cdot \mathbf{r}} + \hat{a}_k^\dagger e^{i\omega_k t - i\mathbf{k}_k \cdot \mathbf{r}} \right] \quad (3.18)$$

The electric field and magnetic field operators are given by Eq. 3.19 and 3.20.

$$\hat{E}(\mathbf{r}, t) = \sum_k i \sqrt{\frac{\hbar \omega_k}{2\epsilon_0 V}} \hat{\epsilon}_k \left[\hat{a}_k e^{-i\omega_k t + i\mathbf{k}_k \cdot \mathbf{r}} - \hat{a}_k^\dagger e^{i\omega_k t - i\mathbf{k}_k \cdot \mathbf{r}} \right] \quad (3.19)$$

$$\hat{H}(\mathbf{r}, t) = \sum_k i \sqrt{\frac{\hbar c^2}{2\mu_0 V \omega_k}} \vec{k}_j \times \hat{\epsilon}_k \left[\hat{a}_k e^{-i\omega_k t + i\mathbf{k}_k \cdot \mathbf{r}} - \hat{a}_k^\dagger e^{i\omega_k t - i\mathbf{k}_k \cdot \mathbf{r}} \right] \quad (3.20)$$

It will also be useful to discuss the positive ($\hat{\mathcal{A}}^{(+)}(\mathbf{r}, t)$) and negative ($\hat{\mathcal{A}}^{(-)}(\mathbf{r}, t)$) frequency components separately, where

$$\hat{\mathcal{A}}^{(+)}(\mathbf{r}, t) = \sum_k \sqrt{\frac{\hbar}{2\epsilon_0 V \omega_k}} \hat{\epsilon}_k \hat{a}_k e^{-i\omega_k t + i\mathbf{k}_k \cdot \mathbf{r}} \quad (3.21)$$

$$\hat{\mathcal{A}}^{(-)}(\mathbf{r}, t) = \sum_k \sqrt{\frac{\hbar}{2\epsilon_0 V \omega_k}} \hat{\epsilon}_k \hat{a}_k^\dagger e^{i\omega_k t - i\mathbf{k}_k \cdot \mathbf{r}} \quad (3.22)$$

Similarly, the positive and negative frequency components can be written for the electric field ($\hat{\mathcal{E}}^{(+)}(\mathbf{r}, t)$, $\hat{\mathcal{E}}^{(-)}(\mathbf{r}, t)$) and magnetic field ($\hat{\mathcal{H}}^{(+)}(\mathbf{r}, t)$, $\hat{\mathcal{H}}^{(-)}(\mathbf{r}, t)$) operators.

3.1 Cavity vs. free-space operators

It is conventional to write the fields inside finite cavities with photon number operators in units of photons, while free-space fields are generally written so that their photon number operators have units of flux (photons/second). This is often confusing as it is assumed without comment.

So far we have assumed the fields exist in an effective cavity. In this dissertation we will need to connect intracavity fields to free-space fields. To determine the connection, we will consider the one-dimensional case where $\vec{r} \rightarrow z$, and $\vec{k} \cdot \vec{r} = kz$.

In free-space, the fields are represented in the form

$$\hat{A}(z, t) = \hat{a}e^{ikz - i\omega t} \quad (3.23)$$

This is analogous to a running EM wave. To connect these to the intracavity annihilation operators, we decompose them as a combination of intracavity modes:

$$\hat{A}(z, t) = \sum_k \hat{a}_k e^{ikz - i\omega_k t} \quad (3.24)$$

Then the commutator is

$$\left[\hat{A}(z, t), \hat{A}^\dagger(z, t) \right] = \sum_{k, k'} \left[\hat{a}_k e^{-i\omega_k t + ikz}, \hat{a}_{k'}^\dagger e^{i\omega_{k'} t' - ik' z'} \right] \quad (3.25)$$

$$= \sum_{k, k'} \left[\hat{a}_k, \hat{a}_{k'}^\dagger \right] e^{ikz - ik' z' - i\omega_k t + i\omega_{k'} t'} \quad (3.26)$$

The commutator $\left[\hat{a}_k, \hat{a}_{k'}^\dagger \right] = \delta_{k, k'}$, and frequency is related to the wavevector by $\omega = ck$, so Eq. 3.26 becomes (at $z' = z$):

$$\left[\hat{A}(z, t), \hat{A}^\dagger(z, t) \right] = \sum_{k, k'} \delta_{k, k'} e^{ikz - ik' z' - i\omega_k t + i\omega_{k'} t'} \quad (3.27)$$

$$= \sum_k e^{ik(z - z' - c(t - t'))} \quad (3.28)$$

$$= \sum_k e^{-ikc(t - t')} \quad (3.29)$$

Inside the cavity (of length L), the wavevectors allowed are $kL = 2\pi m$, where m is an integer [72]. The distance in k-space between adjacent modes is $dkL = 2\pi \rightarrow dk = \frac{2\pi}{L}$. In free space, the sum in Equation 3.28 can be replaced with an integral:

$$\left[\hat{A}(z, t), \hat{A}^\dagger(z, t) \right] = \sum_k e^{ik(z - z' - c(t - t'))} \cdot \frac{dk}{dk} \quad (3.30)$$

$$= \frac{1}{dk} \int_k e^{ik(z - z' - c(t - t'))} dk \quad (3.31)$$

$$= \frac{L}{2\pi} \int_k e^{-ikc(t - t')} dk \quad (3.32)$$

The integral $\int_k e^{-ikc(t - t')} dk = 2\pi\delta(c(t - t'))$, then

$$\frac{L}{2\pi} \int_k e^{-ikc(t-t')} dk = L\delta(c(t-t')) \quad (3.33)$$

$$= \frac{L}{c} \delta(t-t') \quad (3.34)$$

Comparing Eq. 3.29 and Eq. 3.34 we can connect the intracavity and free-space annihilation and creation operators by the normalization L/c , such that

$$\langle \hat{A}^\dagger \hat{A} \rangle = \frac{c}{L} \langle \hat{a}^\dagger \hat{a} \rangle \quad (3.35)$$

where $\hat{A}(z, t)$, $\hat{A}^\dagger(z, t)$ are the free-space operators, and \hat{a} , \hat{a}^\dagger are the intracavity operators. In the following chapters, all field operators inside the WGMR cavity (lowercase \hat{a}) will have units of photons, and field operators outside the cavity (uppercase \hat{A}) will have units of photon flux [73], connected by Eq. 3.35.

3.2 Coherent states

The eigenstates $|n_k\rangle$ of the Hamiltonian are also eigenstates of the number operator $\hat{a}_k^\dagger \hat{a}_k |n_k\rangle = n_k |n_k\rangle$, where n_k is the number of excitations in mode k . These are called *number* or *Fock* states, as they have a definite number of excitations. The creation and annihilation operators act on these states to increase or decrease the number of excitations, and therefore change the number state. While theoretically easy to work with, these states are not easily found in nature. A classical monochromatic electromagnetic field is most accurately represented by superposition of number states, called *coherent states* [74]. The representation of a single mode coherent state

is:

$$|\alpha\rangle_k = \sum_n \frac{\alpha_k^n}{\sqrt{n!}} e^{-\frac{1}{2}|\alpha_k|^2} |n\rangle \quad (3.36)$$

$$(3.37)$$

Note that they are eigenstates of the annihilation operator, so $\hat{a}|\alpha\rangle = \alpha|\alpha\rangle$. Also note that these states do not have a definite number of excitations, but only a mean excitation number. The number operator expectation value is $\langle\alpha|\hat{a}^\dagger\hat{a}|\alpha\rangle = \alpha$.

The ideal output of a laser is an example of a coherent state.

In order to examine the uncertainty relations, it is useful to define the *quadrature operator* $\hat{\mathbf{X}}(\phi)$ as a combination of the annihilation and creation operators:

$$\hat{\mathbf{X}}(\phi) = \hat{a}^\dagger e^{i\phi} + \hat{a} e^{-i\phi} \quad (3.38)$$

We further define the two orthogonal cases, where $\phi = 0$ and $\pi/2$, as $\hat{\mathbf{X}}\mathbf{1}$ and $\hat{\mathbf{X}}\mathbf{2}$, respectively.

$$\hat{\mathbf{X}}\mathbf{1} = \hat{a} + \hat{a}^\dagger \quad (3.39)$$

$$\hat{\mathbf{X}}\mathbf{2} = -i(\hat{a} - \hat{a}^\dagger) \quad (3.40)$$

These are known as the *amplitude quadrature* ($\hat{\mathbf{X}}\mathbf{1}$) and *phase quadrature* ($\hat{\mathbf{X}}\mathbf{2}$). This provides a useful basis for representing the properties of light. The equation for the electric field operator \hat{E} can be written as

$$\hat{E}(z, t) = \sqrt{\frac{\hbar\omega}{2\epsilon_0 V}} \left[\hat{\mathbf{X}}_1 \cos(\omega t - kz) + \hat{\mathbf{X}}_2 \sin(\omega t - kz) \right] \quad (3.41)$$

Figure 3.1 shows a coherent state displayed in quadrature space. The expectation value of the amplitude corresponds to the length of the line, and the phase is the angle relative to the $\hat{\mathbf{X}}_1$ quadrature. There is uncertainty in the absolute state, which is shown as a spread of points around the expectation value. Uncertainty is represented as $\Delta\hat{\mathbf{X}}$, and the quadrature operators obey the uncertainty principle, as they are hermitian:

$$\langle \Delta\hat{\mathbf{X}}_1^2 \rangle \langle \Delta\hat{\mathbf{X}}_2^2 \rangle = 1 \quad (3.42)$$

A coherent state has a minimum uncertainty, with equal uncertainty in each quadrature:

$$\langle \Delta\hat{\mathbf{X}}_1^2 \rangle = \langle \Delta\hat{\mathbf{X}}_2^2 \rangle = 1 \quad (3.43)$$

3.3 Squeezed light

Uncertainties below the quantum limit are allowed in one quadrature, so long as the uncertainty in the other quadrature increases to preserve the uncertainty inequality. This is known as a *squeezed state*. These states were first classified by D. F. Walls in 1983 [75]. Figure 3.2 shows a ball-and-stick model of a coherent state, amplitude

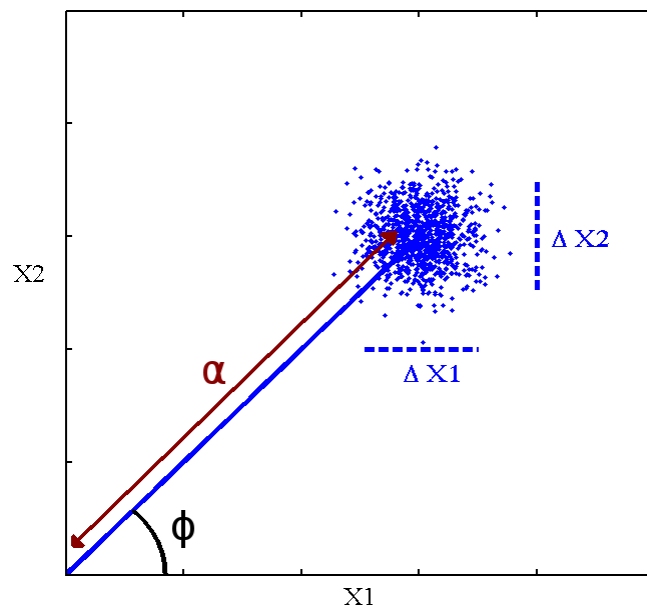


FIG. 3.1: Representation of light in quadrature space. The dots represent “measurements” of the light field. The length of the line shows the average amplitude, and the angle is the phase. The uncertainties in the quadratures $\Delta \hat{X}1$ and $\Delta \hat{X}2$ are indicated.

squeezed state, and a phase squeezed state.

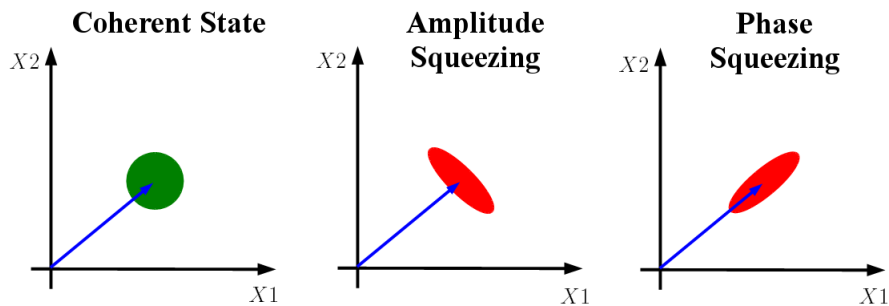


FIG. 3.2: Ball-on-stick representation of a laser in quadrature space. The arrow indicates the amplitude and the angle is the phase. Ball represents the uncertainty in amplitude and phase. *Left*: a *coherent* state, with an equal area of uncertainty. *Middle*: an *amplitude squeezed* state, where the amplitude uncertainty is below the standard quantum limit (SQL) and the phase uncertainty is above the SQL. The uncertainty area is the same as in the coherent case. *Right*: a *phase squeezed* state.

A squeezed state $|S\rangle$ can be described mathematically as a coherent state $(|\alpha\rangle)$ that has been acted upon by the squeezing operator (Eq. 3.44), which is defined in Eq. 3.45 [73]:

$$|S\rangle = \hat{S}|\alpha\rangle \quad (3.44)$$

$$\hat{S}(\eta) = e^{\frac{1}{2}\eta^* \hat{a}^2 - \frac{1}{2}\eta \hat{a}^{\dagger 2}} \quad (3.45)$$

where η is a complex parameter defining the amount (r_s) and angle (θ_s) of squeezing.

$$\eta = r_s e^{2i\theta_s} \quad (3.46)$$

The angle θ_s is the direction of maximum squeezing. For example, squeezing

along $\hat{\mathbf{X}}\mathbf{1}$ occurs when $\theta_s = 0$, then the variance is

$$Var(\hat{\mathbf{X}}\mathbf{1}) = \langle \Delta \hat{\mathbf{X}}\mathbf{1}^2 \rangle = e^{-2r_s} \quad (3.47)$$

This is less than 1, below the standard quantum limit exhibited by a coherent state (Eq. 3.43). With $\theta_s = 0$, the variance of the $\hat{\mathbf{X}}\mathbf{2}$ quadrature is

$$Var(\hat{\mathbf{X}}\mathbf{2}) = \langle \Delta \hat{\mathbf{X}}\mathbf{2}^2 \rangle = e^{2r_s} \quad (3.48)$$

Equation 3.48 shows the increase in uncertainty of the anti-squeezed quadrature.

A pure squeezing operator is difficult to realize experimentally. Generating squeezed light requires a process to have a Hamiltonian containing terms similar to the squeezing operator. The squeezing operator can be approximated (using the Baker-Hausdorff lemma [76]):

$$\hat{S}(\eta) = e^{\frac{1}{2}\eta^* \hat{a}^2} e^{-\frac{1}{2}\eta \hat{a}^{\dagger 2}} e^{-\frac{1}{4}|\eta|^2 [a^2, a^{\dagger 2}]} \quad (3.49)$$

$$\cong \left(1 + \frac{1}{2}\eta^* \hat{a}^2\right) \left(1 - \frac{1}{2}\eta \hat{a}^{\dagger 2}\right) \left(1 - \frac{1}{4}|\eta|^2 [\hat{a}^2, \hat{a}^{\dagger 2}]\right) \quad (3.50)$$

$$\cong 1 + \frac{1}{2}(\eta^* a^2 - \eta a^{\dagger 2}) \quad (3.51)$$

The nonlinear term \hat{a}^2 in Equation 3.51 corresponds to pair elimination, and the $\hat{a}^{\dagger 2}$ term to pair production. These are also present in the nonlinear processes second harmonic generation (SHG) and parametric down-conversion (PDC).

Both SHG [11–18] and PDC [19–25] have been used to generate squeezed light.

Second harmonic generation squeezing can produce bright (non-vacuum state), amplitude squeezed light. PDC-based squeezing is often used to produce squeezed vacuum states, with an arbitrary squeezing angle. Squeezed vacuum has been used to produce some of the largest squeezing [23, 25] of more than 10 dB. However, these systems require > 1 W of pump power. SHG-based squeezing requires fewer steps, as PDC-based systems usually first require the generation of a pump field (often through SHG).

Squeezed-vacuum states through PDC have been demonstrated using a whispering-gallery mode resonator[77]. We focus on the possibility of using whispering-gallery mode resonators to produce low-power bright squeezed light via second harmonic generation.

The Hamiltonian for second harmonic generation is [11, 73]

$$\mathcal{H}_{SHG} = \frac{i}{2} \hbar \varepsilon \left(\hat{a}^{\dagger 2} \hat{b} - \hat{a}^2 \hat{b}^{\dagger} \right) \quad (3.52)$$

where ε is the second harmonic conversion rate, the term $\hat{a}^{\dagger 2} \hat{b}$ says that the annihilation of two photons in one field ($\hat{a}\hat{a}$) is coupled with the creation of one photon in another field (\hat{b}), and the $\hat{a}^{\dagger 2} \hat{b}$ term captures the reverse process which must also occur – the destruction of one photon (\hat{b}) and the creation of two photons ($\hat{a}^{\dagger 2}$).

The quantitative demonstration of squeezing is derived in the following sections. Figure 3.3 gives a qualitative picture of the effect of second harmonic generation on the intensity fluctuations. Intensity fluctuations can be viewed as a fluctuation in photon density in time. Higher intensity corresponds to photons that are more closely spaced in time. Second harmonic generation is an intensity dependent process, so conversion is more likely to happen to more closely spaced photon pairs. These are removed

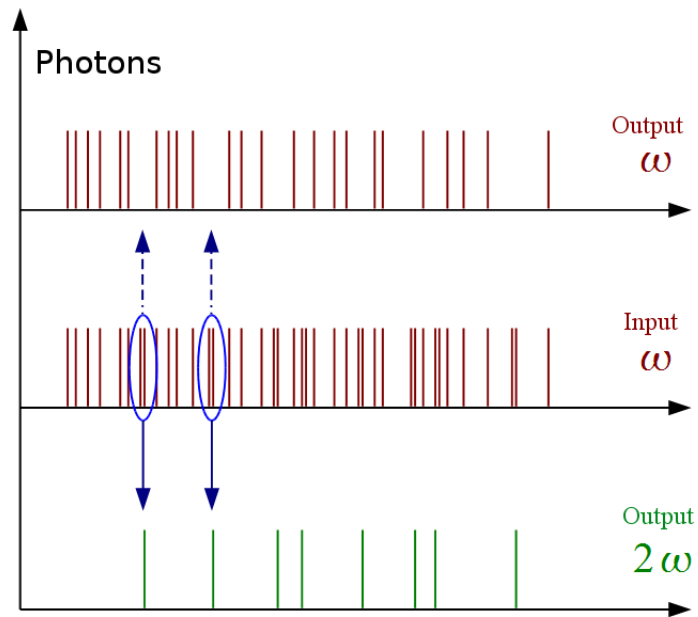


FIG. 3.3: Photon schematic of intensity noise reduction through SHG. *Middle axis* represents a stream of photons entering a nonlinear medium. As second harmonic generation is intensity dependent, the high-intensity fluctuations are more likely to be converted and removed from the output pump field (*top axis*). This has the effect of reducing the amount of fluctuations in intensity in both the output pump and SH fields – resulting in amplitude squeezing.

from the pump field, leaving behind a smaller range of fluctuations. Thus the output pump field has reduced uncertainty in amplitude; it is an amplitude squeezed state.

3.4 Quantum noise analysis of WG modes

We model our whispering-gallery mode resonator by comparing it to a two-mirror cavity (Fig. 3.4). One mirror is the input and output coupler, and the other is a high-reflector. In a high quality factor whispering-gallery mode resonator there is little loss as light travels around disk, so we take the cumulative effect and model it as single high-reflector mirror. It is important to note that we will consider the intracavity field to be traveling waves, and not stationary waves as is possible in a typical two mirror cavity. The output fields overlap with the reflected fields from the input. We define the input fields a_{in}, b_{in} , intracavity fields a, b , and output fields a_o, b_o for each mode. The intracavity Hamiltonian (Eq. 3.53) describes the fundamental field a (with frequency ω), the second harmonic field b (with frequency 2ω), and the interaction between them.

$$\hat{H}_{sys} = \hbar\omega_a \hat{a}^\dagger \hat{a} + \hbar\omega_b \hat{b}^\dagger \hat{b} + \frac{i}{2} \hbar\varepsilon (\hat{a}^\dagger \hat{a}^\dagger \hat{b} - \hat{a} \hat{a} \hat{b}^\dagger) \quad (3.53)$$

The interaction is mediated by the nonlinear conversion coefficient of the WGMR crystal ε . We model the flow through the coupler for each field with the cavity coupling rates γ_a^i, γ_b^i . Loss around the edge of the cavity (the high-reflector) is modeled using the coupling rates γ_a^u, γ_b^u , connecting the intracavity fields to the environmental fields u_a, u_b . The total coupling rates are $\gamma_a = \gamma_a^i + \gamma_a^u, \gamma_b = \gamma_b^i + \gamma_b^u$.

The rate of change of the fields inside the cavity is given by Heisenberg's equation of motion [71]:

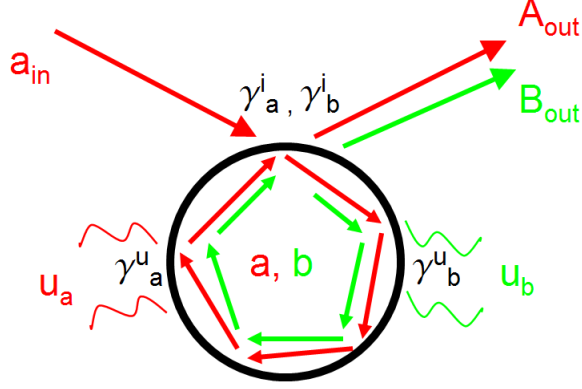


FIG. 3.4: Input/output diagram of WGMR and SHG fields. Pump field (\hat{a}_{in}) and output field (A_{out}) are coupled to WGMR intracavity field \hat{a} through the coupling rate γ_a^i . Loss inside the cavity is modeled as coupling (through γ_a^u) to an environmental field (\hat{u}_a). The same holds for the second harmonic field (\hat{b}).

$$\frac{d}{dt}\hat{a} = \frac{i}{\hbar} [\hat{H}, \hat{a}] \quad (3.54)$$

Following the input/output formalism of [78], we include the coupling rates to find Eqs. 3.55 and 3.56.

$$\dot{\hat{a}} = -\frac{i}{\hbar}[\hat{a}, \hat{H}_{sys}] - \frac{1}{2}\gamma_a^i\hat{a} - \frac{1}{2}\gamma_a^u\hat{a} + \sqrt{\gamma_a^i}\hat{a}_{in} + \sqrt{\gamma_a^u}\hat{u}_a \quad (3.55)$$

$$\dot{\hat{b}} = -\frac{i}{\hbar}[\hat{b}, \hat{H}_{sys}] - \frac{1}{2}\gamma_b^i\hat{b} - \frac{1}{2}\gamma_b^u\hat{b} + \sqrt{\gamma_b^i}\hat{b}_{in} + \sqrt{\gamma_b^u}\hat{u}_b \quad (3.56)$$

Applying these equations to Eq. 3.53 gives the dynamic equations for propagation of the field operators through the cavity Eqs. 3.57 and 3.58 [79]:

$$\dot{\hat{a}} = -i\omega_a \hat{a} - \frac{1}{2}\gamma_a \hat{a} + \varepsilon \hat{a}^\dagger \hat{b} + \sqrt{\gamma_a^i} \hat{a}_{in} + \sqrt{\gamma_a^u} \hat{u}_a \quad (3.57)$$

$$\dot{\hat{b}} = -i\omega_b \hat{b} - \frac{1}{2}\gamma_b \hat{b} - \frac{1}{2}\varepsilon \hat{a} \hat{a} + \sqrt{\gamma_b^i} \hat{b}_{in} + \sqrt{\gamma_b^u} \hat{u}_b \quad (3.58)$$

The frequencies ω_a, ω_b are detunings from the cavity resonance frequencies. We will assume these detunings are much less than the total loss rates, such that $\gamma_a - i\omega_a \cong \gamma_a, \gamma_b - i\omega_b \cong \gamma_b$. In order to simplify the calculations, we separate out the expectation value and the fluctuations around the mean by writing the field operators as $\hat{a} = \langle \hat{a} \rangle + \delta \hat{a}$ ($\langle \hat{a} \rangle = \bar{a}$). We can split the equations into coherent and fluctuation parts and solve separately.

3.4.1 Coherent Equations

We set aside the fluctuation operators ($\delta \hat{a}, \delta \hat{b}$) and first look at the steady-state average values ($\langle \dot{\hat{a}} \rangle = \langle \dot{\hat{b}} \rangle = 0$). Assuming unseeded SHG (where there is no input 2ω field $\bar{b}_{in} = 0$), the average value (time-independent) equations become

$$\frac{1}{2}\gamma_a \bar{a} = \varepsilon \bar{a}^* \bar{b} + \sqrt{\gamma_a^i} \bar{a}_{in} \quad (3.59)$$

$$\frac{1}{2}\gamma_b \bar{b} = -\frac{1}{2}\varepsilon \bar{a}^2 \quad (3.60)$$

as the environmental fields are taken to be in vacuum states $\langle \hat{u}_a \rangle = \langle \hat{u}_b \rangle = 0$. To determine the coherent intracavity fields, we first solve Eq. 3.60 for \bar{b} .

$$|\bar{b}|^2 = \frac{\varepsilon^2}{\gamma_b^2} |\bar{a}|^4 \quad (3.61)$$

Combining Eq. 3.61 with Eq. 3.59 we obtain an expression relating \bar{a} to the

input field, \bar{a}_{in} . This cubic equation can be solved, and there is one real root.

$$|\bar{a}|^3 + \frac{\gamma_a \gamma_b}{2\varepsilon^2} |\bar{a}| - \frac{\gamma_b \sqrt{\gamma_a^i}}{\varepsilon^2} |\bar{a}_{in}| = 0 \quad (3.62)$$

$$\bar{a} = \left(\frac{\gamma_b}{2\varepsilon^2} \right)^{1/3} \left[\left(\sqrt{\gamma_a^i} |\bar{a}_{in}| + \sqrt{\gamma_a^i |\bar{a}_{in}|^2 + \frac{\gamma_a^3 \gamma_b}{54\varepsilon^2}} \right)^{1/3} + \left(\sqrt{\gamma_a^i} |\bar{a}_{in}| - \sqrt{\gamma_a^i |\bar{a}_{in}|^2 + \frac{\gamma_a^3 \gamma_b}{54\varepsilon^2}} \right)^{1/3} \right] \quad (3.63)$$

3.4.2 Fluctuation Equations

To determine the effect of the nonlinear conversion inside the cavity on the quantum noise of the fields, we remove the average values from Equations 3.57 and 3.58, and obtain equations for the fluctuation operators (Eq. 3.64).

$$\begin{aligned} \dot{\delta\hat{a}} &= -\frac{1}{2}\gamma_a \delta\hat{a} + \varepsilon \bar{a}^* \delta\hat{b} + \varepsilon \bar{b} \delta\hat{a}^\dagger + \sqrt{\gamma_a^i} \delta\hat{a}_{in} + \sqrt{\gamma_a^u} \delta\hat{u}_a \\ \dot{\delta\hat{b}} &= -\frac{1}{2}\gamma_b \delta\hat{b} - \varepsilon \bar{a} \delta\hat{a} + \sqrt{\gamma_b^i} \delta\hat{b}_{in} + \sqrt{\gamma_b^u} \delta\hat{u}_b \\ \dot{\delta\hat{a}^\dagger} &= -\frac{1}{2}\gamma_a \delta\hat{a}^\dagger + \varepsilon \bar{a} \delta\hat{b}^\dagger + \varepsilon \bar{b}^* \delta\hat{a} + \sqrt{\gamma_a^i} \delta\hat{a}_{in}^\dagger + \sqrt{\gamma_a^u} \delta\hat{u}_a^\dagger \\ \dot{\delta\hat{b}^\dagger} &= -\frac{1}{2}\gamma_b \delta\hat{b}^\dagger - \varepsilon \bar{a}^* \delta\hat{a}^\dagger + \sqrt{\gamma_b^i} \delta\hat{b}_{in}^\dagger + \sqrt{\gamma_b^u} \delta\hat{u}_b^\dagger \end{aligned} \quad (3.64)$$

We solve these equations by transforming to the frequency domain $\hat{a}(t) \rightarrow \tilde{a}(\Omega)$ by:

$$\hat{a}(t) = \int d\Omega \tilde{a}(\Omega) e^{i\Omega t} \quad (3.65)$$

Equations 3.64 can be combined into matrices in Eq. 3.66, with the matrices and vectors as defined in Eqs. 3.67 - 3.69.

$$i\Omega \tilde{x}_c = M_c \tilde{x}_c + M_{in} \tilde{x}_{in} + M_u \tilde{x}_u \quad (3.66)$$

$$\tilde{x}_c \equiv \begin{pmatrix} \delta \tilde{a} \\ \delta \tilde{a}^\dagger \\ \delta \tilde{b} \\ \delta \tilde{b}^\dagger \end{pmatrix}, \quad \tilde{x}_{in} \equiv \begin{pmatrix} \delta \tilde{a}_{in} \\ \delta \tilde{a}_{in}^\dagger \\ \delta \tilde{b}_{in} \\ \delta \tilde{b}_{in}^\dagger \end{pmatrix}, \quad \tilde{x}_u \equiv \begin{pmatrix} \delta \tilde{u}_a \\ \delta \tilde{u}_a^\dagger \\ \delta \tilde{u}_b \\ \delta \tilde{u}_b^\dagger \end{pmatrix} \quad (3.67)$$

$$M_c \equiv \begin{pmatrix} -\frac{1}{2}\gamma_a & \varepsilon \bar{b} & \varepsilon \bar{a}^* & 0 \\ \varepsilon \bar{b}^* & -\frac{1}{2}\gamma_a & 0 & \varepsilon \bar{a} \\ -\varepsilon \bar{a} & 0 & -\frac{1}{2}\gamma_b & 0 \\ 0 & -\varepsilon \bar{a}^* & 0 & -\frac{1}{2}\gamma_b \end{pmatrix} \quad (3.68)$$

$$M_{in} \equiv \text{diag} \left(\sqrt{\gamma_a^i}, \sqrt{\gamma_a^i}, \sqrt{\gamma_b^i}, \sqrt{\gamma_b^i} \right) \quad (3.69)$$

$$M_u \equiv \text{diag} \left(\sqrt{\gamma_a^u}, \sqrt{\gamma_a^u}, \sqrt{\gamma_b^u}, \sqrt{\gamma_b^u} \right) \quad (3.70)$$

We solve for the intracavity fields \tilde{x}_c in Eq. 3.71. The output fluctuations \tilde{x}_o are found as functions of \tilde{x}_c , \tilde{x}_{in} , and M_{in} in Eq. 3.72. Combining these two equations we arrive at Eq. 3.73. We used *Mathematica* to solve this equation for an analytic

expressions of the elements of \tilde{x}_o .

$$\tilde{x}_c = (i\Omega I - M_c)^{-1} (M_{in}\tilde{x}_{in} + M_u\tilde{x}_u) \quad (3.71)$$

$$\tilde{x}_o \equiv \begin{pmatrix} \delta A_o \\ \delta A_o^\dagger \\ \delta B_o \\ \delta B_o^\dagger \end{pmatrix} \quad (3.72)$$

$$\begin{aligned} \tilde{x}_o &= M_{in}\tilde{x}_c - \tilde{x}_{in} \\ &= M_{in} (i\Omega I - M_c)^{-1} (M_{in}\tilde{x}_{in} + M_u\tilde{x}_u) - \tilde{x}_{in} \\ &= [M_{in} (i\Omega I - M_c)^{-1} M_{in} - I]\tilde{x}_{in} + M_{in} (i\Omega I - M_c)^{-1} M_u\tilde{x}_u \end{aligned} \quad (3.73)$$

Qualitatively, we expect to detect squeezing in the amplitude quadrature of both the fundamental and second harmonic. Using a direct detection scheme we will only measure the amplitude quadrature, regardless of the phase. We simplify and only solve for the amplitude quadrature $\delta A_1 = \delta A_o + \delta A_o^\dagger$ with $\phi = 0$. The noise we measure is related to the variance $Var(\delta A_1) = \langle |\delta A_1|^2 \rangle$.

3.4.3 Experimental variables

Detection frequency

Noise is detected by measuring the power at different frequencies using a spectrum analyzer. These detection frequencies f are connected to the fourier components Ω from Equation 3.65 by $f = \Omega/2\pi$.

Saturation power

It is convenient to parameterize the SHG coupling coefficient as a quantity that is more easily measured, the saturation power P_{in} [45]. The saturation power is a function of the nonlinear coupling, both pump and SH mode quality factors, and the mode overlap. This parameter is measured in the lab by measuring the SHG conversion efficiency as a function of the pump power. We find the equations for the saturation power by calculating the SHG efficiency P_{SH} / P_{in} .

The input power is the input field a_{in} times the photon energy, $P_{in} = \frac{1}{4}\hbar\nu_p|a_{in}|^2$. The output second harmonic power P_{SH} is obtained by connecting the intracavity SH field from Equation 3.61 to the output field b_{out} through the coupling rate γ_b^i .

$$\begin{aligned}
 |b_{out}|^2 &= \gamma_b^i |b|^2 = \gamma_b^i \frac{\varepsilon^2}{\gamma_b^2} |a|^4 \\
 &= \gamma_b^i \frac{\varepsilon^2}{\gamma_b^2} \left(\frac{\gamma_b}{2\varepsilon^2}\right)^{4/3} \left[\left(\sqrt{\gamma_a^i} |\bar{a}_{in}| + \sqrt{\gamma_a^i |\bar{a}_{in}|^2 + \frac{\gamma_a^3 \gamma_b}{54\varepsilon^2}} \right)^{1/3} \right. \\
 &\quad \left. + \left(\sqrt{\gamma_a^i} |\bar{a}_{in}| - \sqrt{\gamma_a^i |\bar{a}_{in}|^2 + \frac{\gamma_a^3 \gamma_b}{54\varepsilon^2}} \right)^{1/3} \right]^4 \tag{3.74}
 \end{aligned}$$

Then the output SH power ($P_{SH} = \frac{\hbar\nu_s |b_{out}|^2}{4}$) is given by Eq. 3.76.

$$P_{SH} = \frac{\hbar\nu_s \gamma_b^i}{(4\gamma_b \varepsilon)^{4/3}} \left[\left(\sqrt{\gamma_a^i} |\bar{a}_{in}| + \sqrt{\gamma_a^i |\bar{a}_{in}|^2 + \frac{\gamma_a^3 \gamma_b}{54\varepsilon^2}} \right)^{1/3} \right. \tag{3.75}$$

$$\left. + \left(\sqrt{\gamma_a^i} |\bar{a}_{in}| - \sqrt{\gamma_a^i |\bar{a}_{in}|^2 + \frac{\gamma_a^3 \gamma_b}{54\varepsilon^2}} \right)^{1/3} \right]^4 \tag{3.76}$$

We write the efficiency as a function of the ratio of the input power to a constant

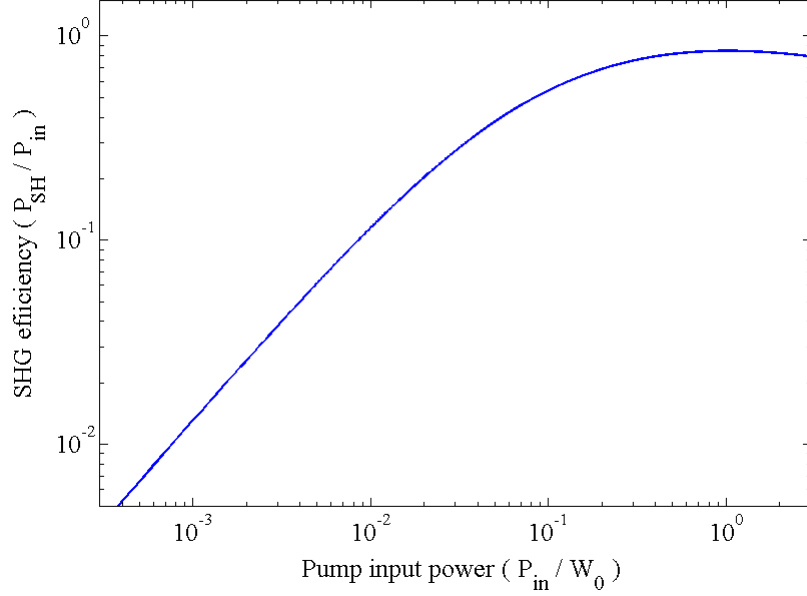


FIG. 3.5: Output second harmonic generation efficiency versus input pump power normalized by saturation power W_0 .

(P_{in}/W_0) . The constant W_0 is the saturation power, defined in Equation 3.77. By measuring the saturation power we can measure our effective conversion coefficient ε , as in Equation 3.78.

$$W_0 = \frac{\hbar\nu_p \gamma_a^3 \gamma_b}{4 \varepsilon^2 \gamma_a^i} \quad (3.77)$$

$$\varepsilon = \sqrt{\frac{\hbar\nu_p \gamma_a^3 \gamma_b}{4 W_0 \gamma_a^i}} \quad (3.78)$$

Cavity loss rates

The cavity loss rates (γ_a^u, γ_b^u) are measures of the loss as the field travels through the WGMR. As seen in Sec. 2.2, the quality factor is also a measure of the loss. We

use our measurements of the quality factor Q_0 to set the cavity loss rates (Eq. 3.79).

$$\gamma^i = \frac{2\pi\nu}{Q_0} \quad (3.79)$$

Non-ideal WGM coupling

We must also take into account any deviation from ideal (impedance-matched) coupling. The quality factor measured in the experiment is the coupling (or loaded) Q-factor (Q_c), which is a function of the intrinsic Q-factor (Q_0), the WGM coupling efficiency, and the input-to-cavity mode-matching (Γ_M). Deviations from impedance-matching reduce the fractional mode depth (K) which is seen in the transmission spectrum. The fractional depth dependence on Q_0 , Q_c , and the mode-matching (Γ_M) has been calculated in Ref. [80], as shown in Eq. 3.80.

$$K = \frac{4 Q_0 Q_c \Gamma_M^2}{(Q_0 + Q_c)^2} \quad (3.80)$$

The parameters Q_c and K are measured experimentally. We use Eq. 3.81 to estimate the intrinsic quality factor to use in the fluctuation calculations. This equation holds for the over-coupling regime. For our calculations we assume perfect mode-matching ($\Gamma_M = 1$) to get Equation 3.82.

$$Q_0 = Q_c \left[\frac{2\Gamma_M^2}{K} - 1 + \frac{2\Gamma_M}{\sqrt{K}} \sqrt{\frac{\Gamma_M^2}{K} - 1} \right] \quad (3.81)$$

$$Q_0 = \frac{Q_c}{K} \left[2 - K + 2\sqrt{1 - K} \right] \quad (3.82)$$

3.5 Model predictions

The output variances are determined by solving the matrix Eq. 3.73 and putting the results into quadrature form ($\delta A_1 = \delta A_o + \delta A_o^\dagger$). Shot noise from the laser is ideally $V1 = 1$ (a coherent state). We use this as our input noise, so \tilde{x}_{in} (Eq. 3.67) obeys Equation 3.83, where $\delta a_1^{in} = \delta a_{in} + \delta a_{in}^\dagger$.

$$Var(\delta a_1^{in}) = 1 \tag{3.83}$$

Our solution to Eq. 3.73 depends on the following variables: input power (W_0), saturation power (W_{sat}), coupling Q-factors for the pump and SH fields ($Q_{a,c}$ and $Q_{b,c}$), the coupling efficiency (K), and the detection frequency (Ω). We have control over these variables, to varying degrees, in the experiment. We anticipate that squeezing will be optimal at low detection frequency, high quality factor and low saturation power. We suspect squeezing will be optimal at a pump power near the saturation power.

As an initial test, we used the undepleted pump approximation. In this assumption, second harmonic generation is small enough that the pump field is not attenuated by conversion. We expect that under this assumption, there should be no predicted squeezing.

3.5.1 Undepleted pump approximation

Second harmonic generation is often studied in the limit where the generated field doesn't significantly reduce the pump field. This is known as the undepleted pump approximation. We first solved the fluctuations equations in this limit to test our

qualitative expectations. As we interpret the intensity-dependent conversion process as selectively removing high-intensity fluctuations from the pump field and therefore reducing the intensity noise in both fields, we expect to find no noise reduction in the undepleted pump case.

$$M_c(\bar{b} \rightarrow 0) = \begin{pmatrix} -\frac{1}{2}\gamma_a & 0 & \varepsilon\bar{a}^* & 0 \\ 0 & -\frac{1}{2}\gamma_a & 0 & \varepsilon\bar{a} \\ -\varepsilon\bar{a} & 0 & -\frac{1}{2}\gamma_b & 0 \\ 0 & -\varepsilon\bar{a}^* & 0 & -\frac{1}{2}\gamma_b \end{pmatrix} \quad (3.84)$$

$$\begin{aligned} \delta A_1 = & (4|a|^2\varepsilon^2 + \gamma_a\gamma_b)^{-1} \left[(2\gamma_b\gamma_a^i - \gamma_a\gamma_b - 4|a|^2\varepsilon^2) \delta a_1^{in} \right. \\ & + 2\gamma_b\sqrt{\gamma_a^i\gamma_a^u}\delta u_1^a + 4\varepsilon\sqrt{\gamma_a^{in}\gamma_b^{in}} \left(\bar{a}^*\delta b_i + \bar{a}\delta b_i^\dagger \right) \\ & \left. + 4\varepsilon\sqrt{\gamma_a^{in}\gamma_b^u} \left(\bar{a}^*\delta b_u + \bar{a}\delta b_u^\dagger \right) \right] \end{aligned} \quad (3.85)$$

With no pump depletion we take Equation 3.68 and set $\bar{b} \rightarrow 0$ (Eq. 3.84). Then we solved Eq. 3.73 for the intensity quadrature fluctuations of the pump field δA_1 (Eq. 3.85). The variance $Var(\delta A_1)$ is then determined in terms of the variances of the other fields (Eq. 3.87). We find that if the variances of the other fields are unity (they are coherent states) then we expect no effect on the variance of the pump field.

$$\begin{aligned}
Var(\delta A_1) &= \langle |\delta A_1|^2 \rangle \\
&= (4|a|^2 \varepsilon^2 + \gamma_a \gamma_b)^{-2} \times \left[(2\gamma_b \gamma_a^i - \gamma_a \gamma_b - 4|a|^2 \varepsilon^2)^2 Var(\delta a_1^{in}) \right. \\
&\quad + 4\gamma_b^2 \gamma_a^i \gamma_a^u Var(\delta u_1^a) + 4\varepsilon^2 \gamma_a^{in} \gamma_b^{in} (X_{1a}^2 Var(\delta b_1^{in}) + X_{2a}^2 Var(\delta b_2^{in})) \\
&\quad \left. + 4\varepsilon^2 \gamma_a^{in} \gamma_b^u (X_{1a}^2 Var(\delta u_1^b) + X_{2a}^2 Var(\delta u_2^b)) \right] \tag{3.86} \\
&= 1 \tag{3.87}
\end{aligned}$$

3.5.2 Transmitted pump noise analysis

We now solve the fluctuation equations using the full matrix in Eq. 3.68. We used *Mathematica* to solve for δA_o , δA_o^\dagger , δB_o , and δB_o^\dagger . The resulting equations were put into quadrature analytically. The resulting variances of the output intensity quadratures $Var(\delta A_1)$ and $Var(\delta B_1)$ was a function of the experimental variables and the input/environment variances ($Var(\delta a_1^{in})$, $Var(\delta a_2^{in})$, $Var(\delta b_1^{in})$, $Var(\delta b_2^{in})$, $Var(\delta a_1^u)$, \dots). As the environment fields are vacuum fields we set their variances $Var(\delta a_1^u) = Var(\delta b_1^u) \rightarrow 1$. We are modeling our system with a coherent pump, so we set $Var(\delta a_1^{in}) \rightarrow 1$.

The solution for $Var(\delta A_1)$ represents the noise in the amplitude quadrature of the pump field. It depends on the input pump power (P_{in}), the saturation power (W_0), the intrinsic and coupling quality factors of the resonator (Q_0 , Q_c), and the detection bandwidth (f_{det}). This large parameter space is constrained by considering the limits to independent variables.

Table 3.1 shows the constraints we used. To find the conditions for optimal squeezing, we limited the variables to values that could in principle be reached (*ideal conditions*). For example, there may be squeezing at a detection bandwidth near DC.

Variable	Ideal conditions	Experimental conditions
	min – max	min – max
Q_0	$1 - 10^8$	$10^6 - 10^8$
Q_c	$1 - 10^8$	$10^5 - 10^8$
P_{in}	$0 - \infty$	$1 \mu\text{W} - 20 \text{mW}$
f_{det}	DC – ∞	1 MHz – 6 MHz
W_0	$\sim \mu\text{W} - \sim \text{W}$	3 mW – 10 W

TABLE 3.1: Constraints on independent variables for theory predictions. *Ideal conditions* column shows the ranges we could search for ideal squeezing conditions. *Experimental conditions* column shows ranges that have can be realized experimentally.

However it is very difficult experimentally to detect quantum noise at low frequencies, as the detection electronics noise in this region is very large. The *experimental conditions* column shows the ranges of values that have been experimentally realized. Our particular experiment is limited further; this is discussed in Sec. 6.5.1.

Additionally, some of the variables possible values depend on the values of other variables. The saturation power is partially inversely related to the quality factors. The minimum saturation power is limited by the maximum intrinsic quality factor.

Ideal conditions

To find the ideal squeezing conditions, we varied the parameters and observed how the variance changed. The vertical axes show the variance of the amplitude quadrature of the pump output ($Var(\delta A_1) = \langle |\delta A_1|^2 \rangle$), in log scale. The noise reduction is relative to the shot noise level, which is set to 0 dB.

Figure 3.6 shows the pump noise as a function of detection frequency for two different intrinsic quality factors ($Q_0 = 5 \times 10^7$ and 1×10^8). This is important as noise is detected by measuring the power spectrum using a spectrum analyzer,

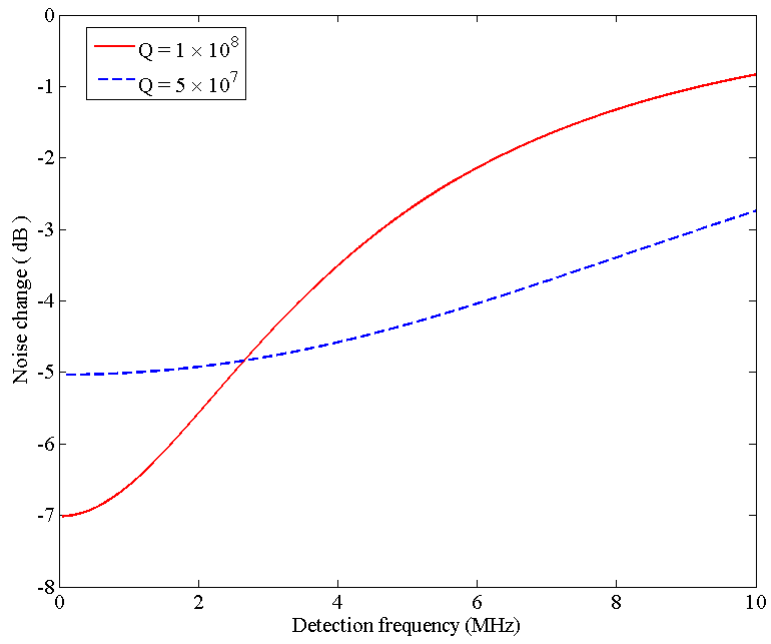


FIG. 3.6: Squeezing vs. detection frequency for the pump field under ideal conditions for two intrinsic quality factors (Q_0). Saturation power $W_0 = 3$ mW, input pump power $P_{in} = 200$ μ W, coupling $Q_c = 1 \times 10^7$.

and the detection spectrum is limited by the detection electronics. Squeezing is a maximum at low detection frequencies, below ~ 1 MHz. Squeezing is reduced at detection frequencies larger than the bandwidth of the WGM resonance. There is not much change below 1 MHz, so we set the detection frequency to 100 kHz as we varied the saturation power and input power.

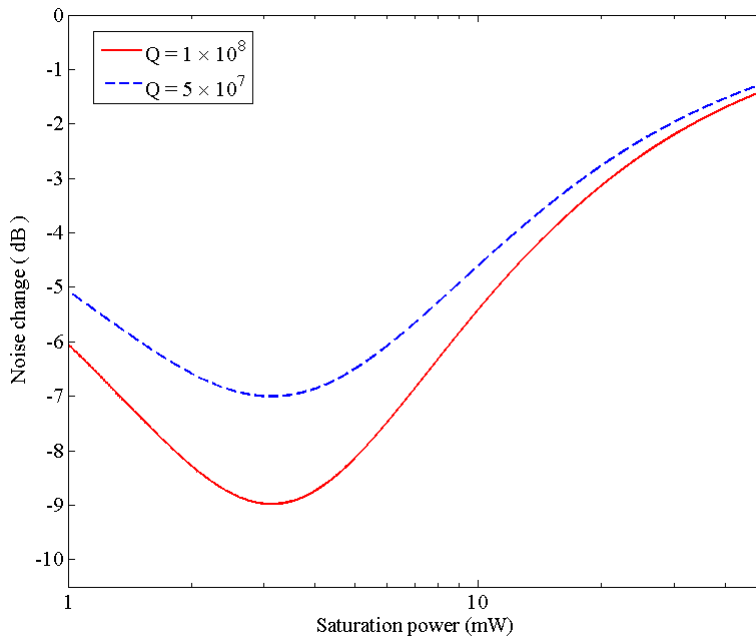


FIG. 3.7: Squeezing vs. saturation power (W_0) for the pump field under ideal conditions for two values of Q_0 . Detection frequency $f = 100$ kHz, input pump power $P_{in} = 200 \mu\text{W}$, coupling $Q_c = 1 \times 10^7$.

The saturation power is a measure of the second harmonic generation efficiency – it represents the input power that results in maximum conversion efficiency. Figure 3.7 shows the noise reduction as a function of the saturation power (W_0) with a fixed input power, for two values of intrinsic quality factor.

The effect is also related to the input power. Figure 3.8 shows the variation with input power (P_0) for two different quality factors. We would expect squeezing to degrade at input powers above the saturation power, as the SHG process will

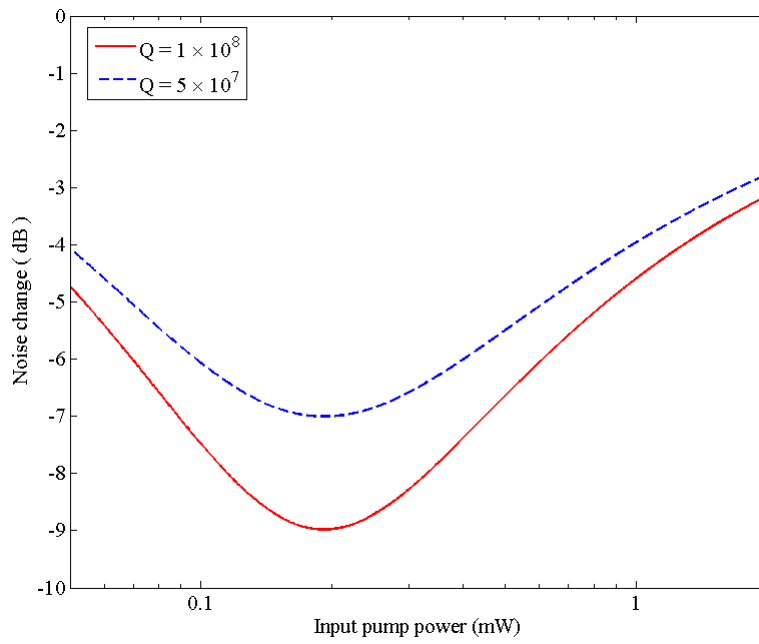


FIG. 3.8: Squeezing vs. input pump power (P_{in}) for the pump field under ideal conditions for two values of Q_0 . Detection frequency $f = 100$ kHz, saturation power $W_0 = 3$ mW, coupling $Q_c = 1 \times 10^7$.

become less efficient. At sufficiently small input powers, the efficiency is likewise lower. Maximum squeezing does not occur at the saturation power, but at a lower input power. This is consistent with our understanding, though it is somewhat lower than anticipated.

Optimal pump power should also depend on the saturation power. In Figure 3.9 we varied the input pump power, with different saturation powers for each trace. There is an input power that minimizes the noise (maximizes squeezing). This input power minimum depends on the saturation power. The amount of noise reduction is independent of the absolute input power, and only depends on the ratio of input power to saturation power. The ratio for maximum squeezing is $P_{in} = 0.067 W_0$.

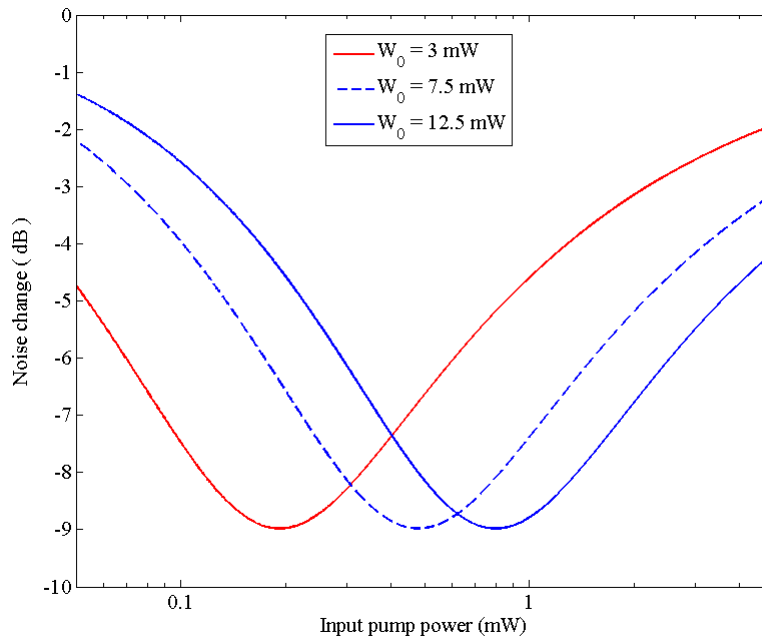


FIG. 3.9: Squeezing vs. input pump power for three values of saturation power under ideal conditions. Detection frequency $f = 100$ kHz, coupling $Q_c = 1 \times 10^7$.

Lastly we examined the effect of the WGMR quality factor on the noise reduction. We expect that squeezing will disappear at low quality factors, due to the extra

loss. Figure 3.10 shows squeezing increasing with increasing Q-factor. The maximum quality factor achievable in lithium niobate (Sec. 2.3.1) is about 10^8 . Squeezing is significantly reduced below a Q_0 of 10^6 .

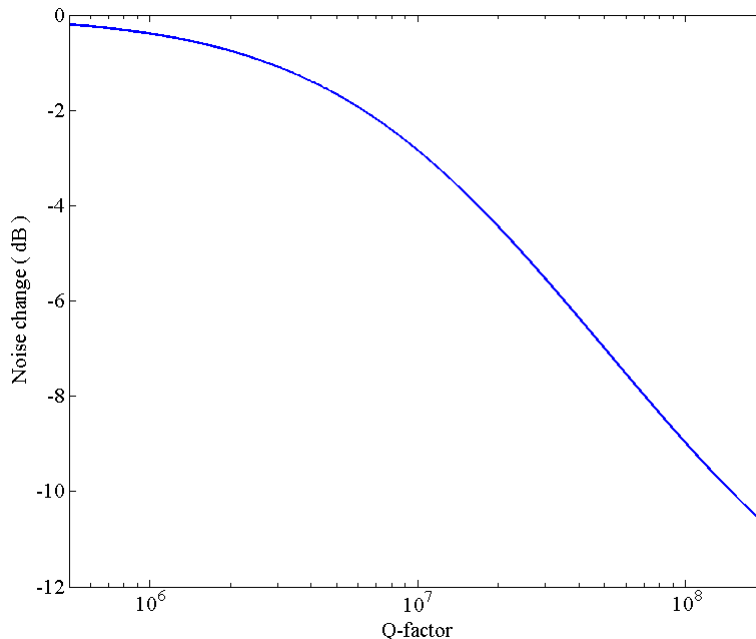


FIG. 3.10: Squeezing vs. quality factor (Q_0) for the pump field under ideal conditions. Detection frequency $f = 100$ kHz, input pump power $P_{in} = 200 \mu\text{W}$, saturation power $W_0 = 3$ mW, coupling $Q_c = 1 \times 10^7$.

Ideal squeezing is achieved with the maximum quality factor, a minimum detection frequency, and a fixed input power to saturation power ratio. For reasonable values ($Q_0 = 10^8$, $f = 100$ kHz, $W_0 = 3$ mW, $P_{in} = 0.2$ mW) the maximum squeezing is around 9 dB.

In the theoretical treatment in [12], they find that the expected squeezing in the pump field increases indefinitely with pump power. However they used a semiclassical model of a single-pass through a crystal, with small pump depletion. A better comparison is found in the doubly-resonant, high-Q (non-WGMR) cavity model of [14].

This is again a semiclassical treatment, but they find that there is an optimum input pump power for squeezing in the pump field, similar to our predictions.

Here we will also note some experimental results for comparison. In [81] they used a single-pass through a LiNbO₃ waveguide to produce 0.8 dB of squeezing in the pump field (1.2 dB inferred). This was done through quasi-phase-matching, and using a mode-locked (pulsed) input field. In [18] a singly-resonant cavity (only on resonance for the pump) was used to produce 0.6 dB of squeezing in the pump field, with 10 mW of pump power.

More work has been done recently with optical parametric oscillation to create vacuum squeezing. In [23] a vacuum squeezing of 10 dB was achieved, and 11.5 dB was reached in [25]. However, they required a total input power of 2 W. In [77], PDC in a WGMR is used to produce 1.2 dB of squeezing, with a pump power of tens of μ W. This scheme still requires an extra step and extra power to first produce SHG. A WGMR-based, all-SHG squeezing could provide significant squeezing at very low input powers, provided some experimental challenges are met (Chapter 6).

In practice, there are other experimental limits to these parameters. The quality factor is limited by the material absorption (and polishing techniques). The detection bandwidth is limited by the detection electronics and classical laser noise. The input power is limited by the locking electronics and the Kerr effect inside the cavity due to the high intensity build-up. In particular, we were limited by the saturation power in our experiment, so we will next examine how this affects our expected squeezing.

Realistic conditions

In our experiment (Chapter 6), the minimum saturation power is 4 W. This is unfortunately higher than previously observed [43, 45], and reduces our expected squeezing significantly. We are also limited to detection bandwidths between 3 \sim

5 MHz. Figure 3.11 shows the expected noise reduction versus detection frequency for saturation powers of 1 and 4 W. The possible squeezing is reduced greatly from the theoretical limit, from ~ 9 dB to < 1 dB.

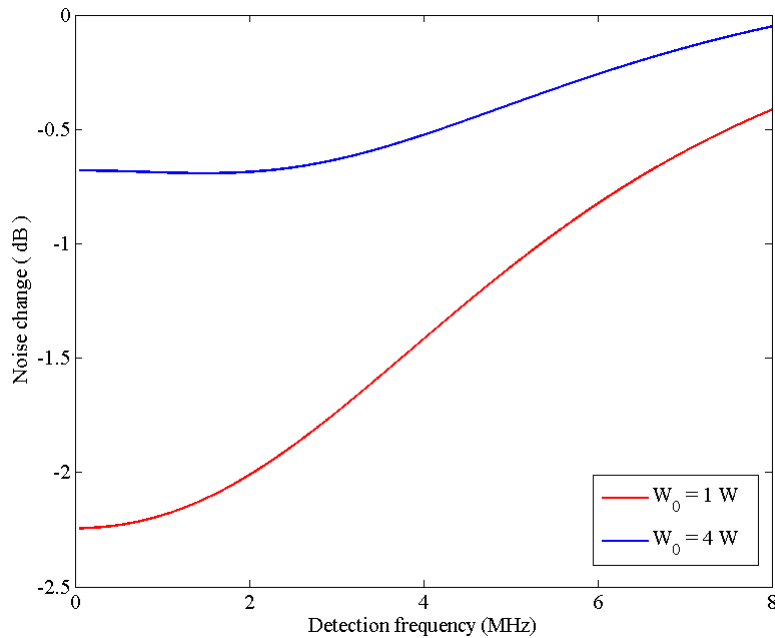


FIG. 3.11: Squeezing vs. detection frequency for the pump field under realistic conditions for two saturation powers (W_0). Input pump power $P_{in} = 10$ mW, $Q_0 = 1 \times 10^8$, coupling $Q_c = 4 \times 10^7$.

With a high saturation power, the optimal input power is too high to be reached experimentally. Above ~ 20 mW of input pump power the cavity becomes unstable. The intensity builds up to the point where the Kerr effect shifts the mode resonance. As the resonance frequency shifts away from the laser frequency, the intracavity intensity drops, reducing the Kerr effect and thus shifting the cavity resonance frequency back. The locking electronics cannot respond fast enough to counteract this effect. This limits the pump power to < 20 mW. Figure 3.12 shows the noise reduction versus saturation power with a fixed input power (10 mW). With this input power, the maximum squeezing occurs near a $W_0 = 100 \sim 200$ mW. Since we were limited

to a saturation power of ~ 4 W, our expected squeezing was limited to < 1 dB. Figure 3.13 shows the dependence on input power.

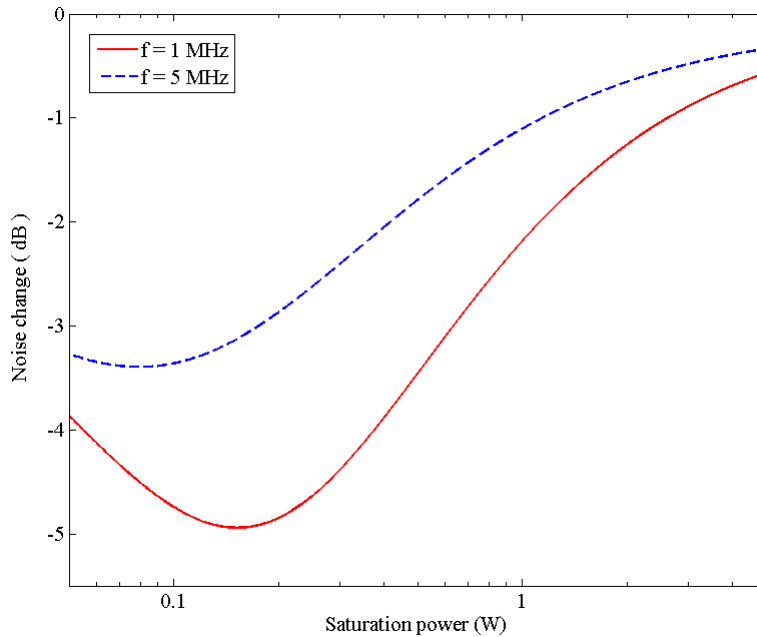


FIG. 3.12: Squeezing vs. saturation power for the pump field under realistic conditions for two detection frequencies. Input pump power $P_{in} = 10$ mW, $Q_0 = 1 \times 10^8$, coupling $Q_c = 4 \times 10^7$.

Lastly, Figure 3.14 shows the dependence on the intrinsic quality factor. Again, the higher the Q , the more squeezing we expect. In Sec. 4.3 we were able to achieve an absorption-limited Q of 10^8 . With our experimental parameters ($Q_0 = 10^8$, $f = 5$ MHz, $W_0 = 4$ W, $P_{in} = 10$ mW), we expect squeezing of ~ 0.5 dB. This is significantly lower than the theoretical maximum, and may be below our ability to resolve. The experimental attempts at detection are detailed in Chapter 6.

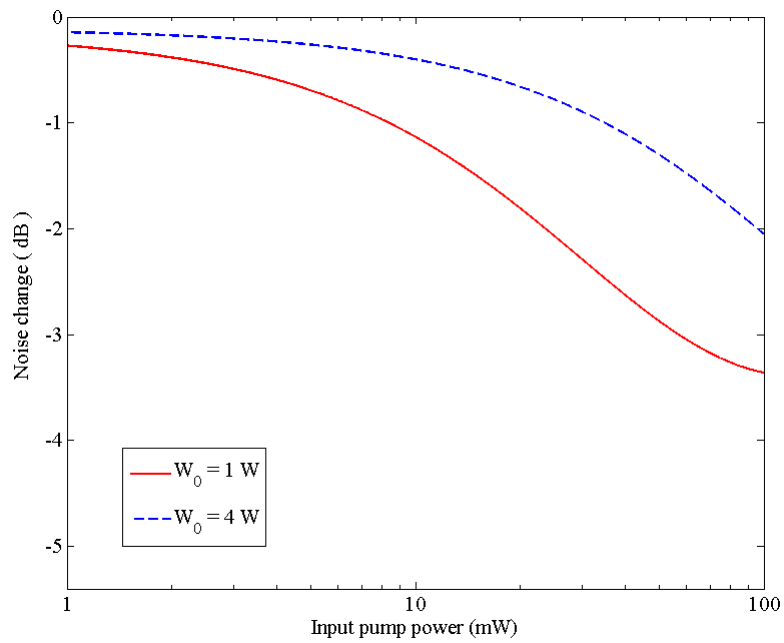


FIG. 3.13: Squeezing vs. input pump power for the pump field under realistic conditions for two saturation powers (W_0). Detection bandwidth $f = 5$ MHz, $Q_0 = 1 \times 10^8$, coupling $Q_c = 4 \times 10^7$.

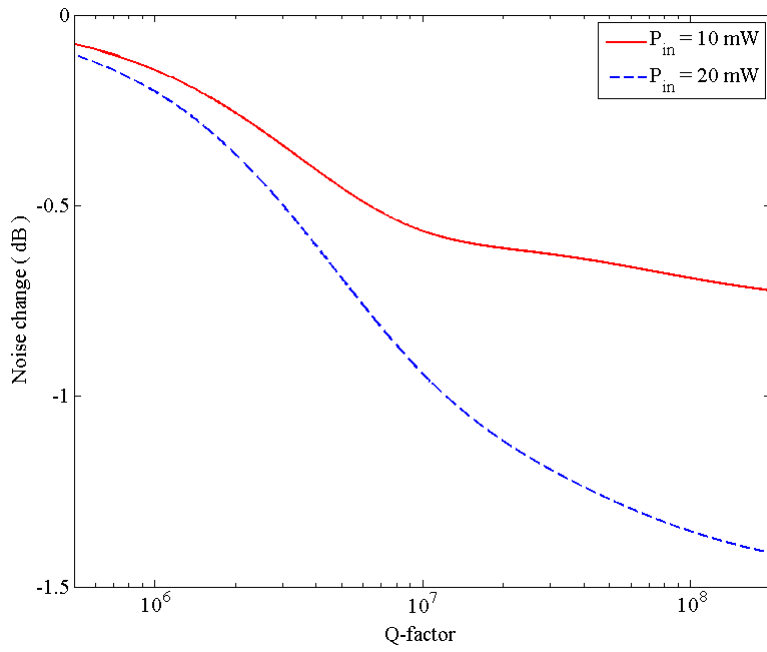


FIG. 3.14: Squeezing vs. Q_0 for the pump field under realistic conditions for two input pump powers (P_{in}). Detection bandwidth $f = 5$ MHz, saturation power $W_0 = 4$ W , coupling $Q_c = 4 \times 10^7$.

CHAPTER 4

Whispering-gallery mode resonator experiment

Whispering-gallery mode resonators have been made from many different materials, using different techniques. WGMR cavities made from Si can be fabricated by etching, while others, made from optical crystals, have used diamond turning. We used nonlinear optical crystal (lithium niobate) and diamond polishing to make millimeter sized WGMR disks. In this chapter we explain our techniques for polishing WGMR disks to achieve a high quality factor and how light is coupled into them to measure their optical properties.

Whispering-gallery mode resonators are a type of cavity that use total internal reflection to achieve very high reflectivity. Two-mirror cavities can be made using mirrors with very high reflectivity, but these cavities are more susceptible to vibrations that change the cavity length and are difficult to couple light into. Whispering-gallery mode resonators are a single, solid structure, and can use evanescent wave-guide coupling for efficient coupling. The relatively small size and the curvature of the

resonators lead to a small mode size inside the disk. Therefore a very high intensity can be built up in a small region, which makes whispering-gallery mode resonators especially useful for nonlinear optical processes.

The quality factor (Q) of the cavity is a measure of how long energy remains in the cavity, and limits the intensity gain. The quality factor is determined by the losses through the cavity. There are four sources of loss that can limit the Q in a whispering-gallery mode resonator. These are scattering on the surface (Q_σ), absorption in the material (Q_α), coupling to the external field (Q_C), and radiative losses (Q_R) [67]. Scattering is controlled by polishing the rim of the disk. Absorption is fixed by the material used to form the cavity. Radiative losses (loss due to the curvature of the cavity) depend on the wavelength and the size of the cavity (because our radii are much larger than the wavelength, these losses are orders of magnitude smaller than scattering, absorption, and coupling losses) [67].

4.1 WGMR coupling

Coupling light into the whispering-gallery mode resonator disk requires evanescent coupling. We used rutile and diamond prisms, both with a higher index of refraction than LiNbO_3 , to create an evanescent wave through total internal reflection along one side of the prism. Bringing the disk in range of the evanescent wave allows the light to enter the disk at an angle θ_{disk} such that it totally internally reflects inside the disk. The beam then exits through the prism at the same point and continues along with the reflected portion of the incident beam. Figure 4.1 shows the prism-WGMR coupling scheme.

4.1.1 Prism geometry

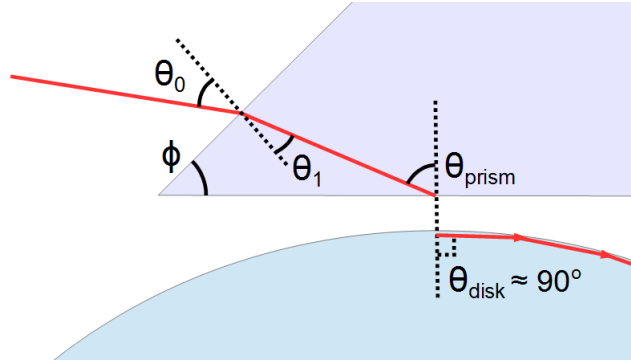


FIG. 4.1: Waveguide coupling diagram showing beam path in prism and disk.

Figure 4.1 shows the prism-disk coupling scheme. The beam entering the disk must travel nearly parallel to the surface ($\theta_{disk} \simeq 90^\circ$) in order to couple to a whispering-gallery mode. This puts a condition on the angle of the beam inside the prism as expressed through Snell's Law:

$$n_{disk} \sin \theta_{disk} = n_{prism} \sin \theta_{prism} \quad (4.1)$$

$$\sin \theta_{disk} = 1 \quad (4.2)$$

$$\theta_{prism} = \arcsin \left(\frac{n_{disk}}{n_{prism}} \right) \quad (4.3)$$

This angle may limit the prism geometries available (depending on the material). For a lithium niobate ($n_{disk} \approx 2.36$) disk and a rutile ($n_{prism} \approx 2.5$) prism, the angle inside the prism with respect to the normal of the disk-face is $\theta_{prism} = 69.5^\circ$. Tracing the ray back to the incident-face of the prism we find the incident angle (θ_o) in terms of the prism's physical angle (ϕ). The angle θ_1 is the angle of the beam inside the prism with respect to the normal of the incident-face.

Material	n_o	n_e	wavelength (nm)
Prisms			
Rutile [82]	2.479	2.74	1064 nm
	2.67	2.98	532 nm
Diamond [83]	2.419	N/A	
WGMR Disks			
LiNbO ₃			
- Stoichiometric [50]	2.234	2.155	1064 nm
	2.325	2.233	532 nm
- Congruent [50]	2.232	2.156	1064 nm
	2.234	2.323	532 nm
- MgO-doped (3 %) [84]	2.229	2.149	1064 nm
	2.318	2.224	532 nm

TABLE 4.1: Refractive indices of prism and disk material used in this dissertation. Values are given for the ordinary (n_o) and extraordinary (n_e) indices of refraction for pump (1064 nm) and second harmonic (532 nm) wavelengths of light. Diamond is isotropic and has only one index of refraction.

$$\theta_1 = \theta_{prism} - \phi = \arcsin\left(\frac{n_{disk}}{n_{prism}}\right) - \phi \quad (4.4)$$

$$\theta_o = \arcsin\left(\frac{n_{prism}}{n_{air}} \sin \theta_1\right) \quad (4.5)$$

$$= \arcsin\left[\frac{n_{prism}}{n_{air}} \sin\left(\arcsin\left(\frac{n_{disk}}{n_{prism}}\right) - \phi\right)\right] \quad (4.6)$$

Table 4.1 shows relevant indices of refraction for materials used in this research. We used several types of lithium niobate crystals for our WGMR disks. Our initial work was done using a rutile 45–45–90 prism with dimensions 5 mm × 5 mm × 5 mm, and a very high index of refraction. We later switched to a smaller, equilateral diamond prism with an anti-reflective coating for both 1064 nm and 532 nm wavelengths, with 1 mm sides. The diamond is more resistant to damage, and the smaller size and anti-reflective coating results in less loss for our noise measurements (Chapter 6).

4.1.2 Coupling mount

Evanescent coupling requires the prism and disk to be within the skin depth (δ_p) of the evanescent wave, as the intensity falls off outside the prism as $I(z) \propto \exp(-z/\delta_p)$. The skin depth depends on refractive index (n_{prism}), incident angle (θ_{prism}), and wavelength (λ) [85]:

$$\delta_p = \frac{\lambda \cos \theta_{prism}}{\sqrt{4\pi^2 (n_{prism}^2 \sin^2(\theta_{prism}) - 1)}} \quad (4.7)$$

In our system δ_p is on the order of $\delta_p < 100nm$. However the coupling Q-factor (Q_c) increases with larger prism-disk separation (d), as $Q_c \propto \exp(d \frac{4\pi}{\lambda \sqrt{n_{disk}^2 - 1}})$ [86]. Thus precise control over the prism-disk separation is necessary to balance these. We designed a mount to hold both the prism and disk at a variable distance (Figure 4.2). The distance was controlled using a lever arm cut into the aluminum mount, and adjusted with a screw (photograph in Fig. 4.3). The prism and disk were both mounted on removable trays to allow them to be replaced. We attached the prism to the tray using a high-temperature epoxy. We attached the disks to the trays using a clamp so they could be removed easily in case they needed repolishing.

4.1.3 Temperature control

To stabilize the WGMR cavity at the optimal phase-matching temperature, we used two heaters and a feedback controller. The heaters were ThorLabs HT15W resistive cartridge heaters set inside holes in the mount below the WGMR disk. One heater was set to constant power, while the second was connected to the feedback controller (schematic in Fig. 4.4). The disk and prism were covered with an acrylic

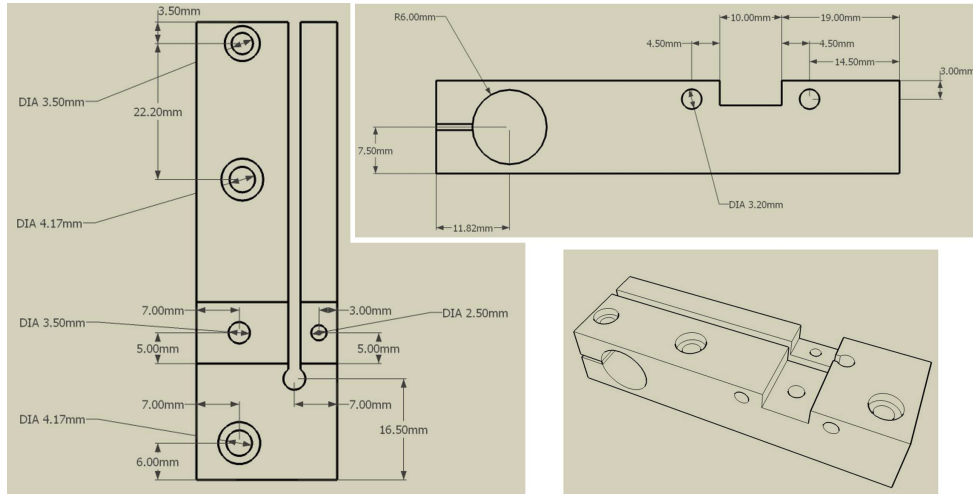


FIG. 4.2: Technical drawings of mount holding WGMR disk and prism.

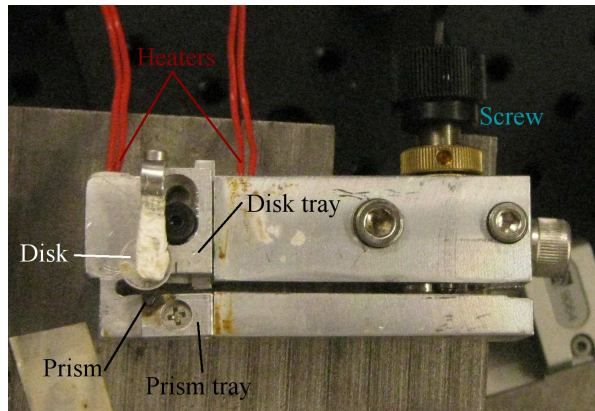


FIG. 4.3: Mount holding prism and WGMR disk. Distance between them is set with a screw. Heaters are located underneath disk tray.

box with ports to allow laser input and output, and the entire apparatus was covered with another box to reduce instability due to air currents.

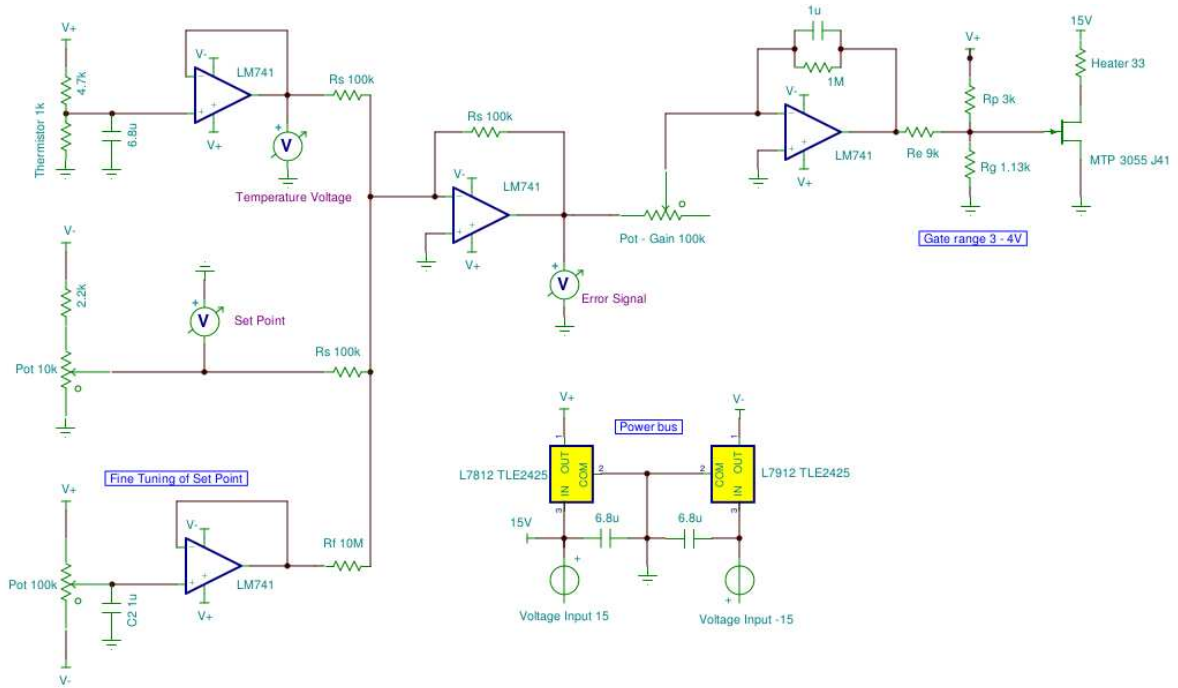


FIG. 4.4: Temperature controller schematic for mount heater.

4.2 Experimental setup

The laser output is sent through an optical diode to prevent reflection back into the laser, then through a polarizing beam cube to ensure polarization along the ordinary axis (n_o) of the disk. Two mirrors steer the beam to adjust the height and level. A lens is used to focus the beam to match the effective size of the resonator at the interface between the prism and disk. The disk and prism are mounted on a rotation stage (for tuning of the incident angle) and a 2-axis translation stage (for tuning the horizontal position of the beam relative to the prism and the position of

the prism-disk interface relative to the focus of lens). The divergent output beam from the prism is collimated by a lens and sent to a photodetector (Figure 4.5).

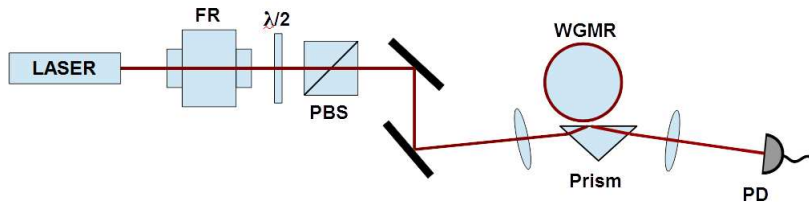


FIG. 4.5: Experimental schematic for WGMR coupling detection.

4.2.1 Equipment

We used different pump lasers for characterization and the second harmonic generation experiment. For characterization and testing of our disks, we used a tunable 795 nm external cavity diode laser. The frequency could be tuned over a range of 70 GHz by scanning the PZT that holds the internal diffraction grating, allowing us to probe the entire free-spectral range of our disks. This was scanned using a function generator.

For the second harmonic generation experiment, we used an InnoLight Mephisto diode-pumped solid-state (DPSS) 1064 nm laser, with both fast frequency tuning using a PZT and slow tuning using the laser crystal temperature. The fast PZT-tuning was limited to 100 MHz, while the slower (< 1 Hz response rate) crystal temperature tuning allowed us to scan over 30 GHz. This made the 1064 nm laser more difficult to use for characterization, however the two-channel tuning allowed for better feedback control of the frequency.

4.2.2 CCD camera and scattering detection

Aligning the pump beam to couple to the WGMR cavity can be challenging, as the focussed beam must hit the spot where the disk is closest to the prism face. The relevant parameters are the vertical angle and position of the beam relative to the prism, the horizontal angle and position of the beam, and the focal position relative to the disk-prism interface. In order to monitor the progress of alignment, a CCD camera (with no infrared filter) was mounted above the apparatus with a slight angle to view the disk-face of the prism. When the laser focal spot is close to the face, it can be seen with the camera. However, more than one reflection is visible, so the proper initial spot must be located by moving the beam horizontally to find the spot with the correct behavior. After aligning the beam so that it totally internally reflects inside the prism near the disk, the disk's rim will illuminate (Fig. 4.6). A detector is placed in the path of the resulting transmitted beam, and the coupling optimized. The process of observing scattering is necessary for initial alignment, as the scattered light is more easily observed by eye (camera) than the transmitted power drop by detector for very low coupling.

Issues that arise during this initial process include aligning the incorrect beam spot and prism surface imperfections. If a secondary reflection is chosen instead of the initial internal reflection on the prism disk-face, some coupling may be visible through scattering losses. However, as the coupling is not in the main beam, there will be no coupling visible in the transmission. Second, there may be imperfections on the prism face that cause the beam to refract out of the prism, instead of maintaining total-internal reflection. This will cause the prism to illuminate, even though none of the beam is coupled into a whispering-gallery mode. This can sometimes be distinguished visibly, as more than just the rim will illuminate, or the disk will illuminate unevenly.

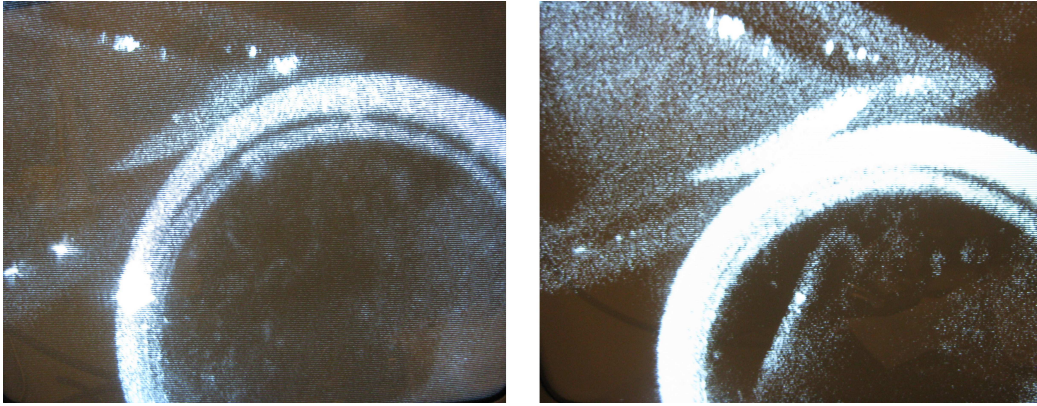


FIG. 4.6: WGM rim scattering is visible with a CCD camera. When light enters a whispering-gallery mode, the intensity builds up and light is scattered as it travels along the rim of the disk. *Left:* Disk-prism separation is just close enough for coupling. *Right:* Disk is brought closer to prism for stronger coupling.

It can also be detected if the frequency-sweep of the laser is reduced to a few Hz. If the disk illumination does not flash, but remains constant, then the illumination is not from scattering out of a whispering-gallery mode.

4.2.3 WGM spectrum

The transmission/reflection from the WGMR cavity gives more detailed information about the WG modes. To see coupling in the transmitted beam, the input laser frequency is scanned. Coupling is observed as a decrease in transmitted power for certain frequencies. Figure 4.7 shows a typical frequency scan and several whispering-gallery modes peaks.

A resonator that is both mode-matched and impedance-matched will show no transmission at the resonance frequencies. Mode-matching requires the shape of the input beam match the shape of the cavity mode. This is more difficult for evanescently-coupled circular WGMRs than mirrored Fabry-Perot cavities, as the beam will enter a prism, hit the coupling spot at an angle, and enter the cavity

through a curved surface. Impedance-matching is easier to control in the WGMR case, as the cavity coupling rate can be controlled by the prism-disk separation distance. We control the separation using a lever design and fine-threaded screw.

By measuring the full-width at half-maximum of the resonances, we can measure the quality factor of the resonator, by Eq. 2.43. In Fig. 4.7 the FWHM is 36 MHz, for a Q of 1×10^7 (with a 795 nm laser).

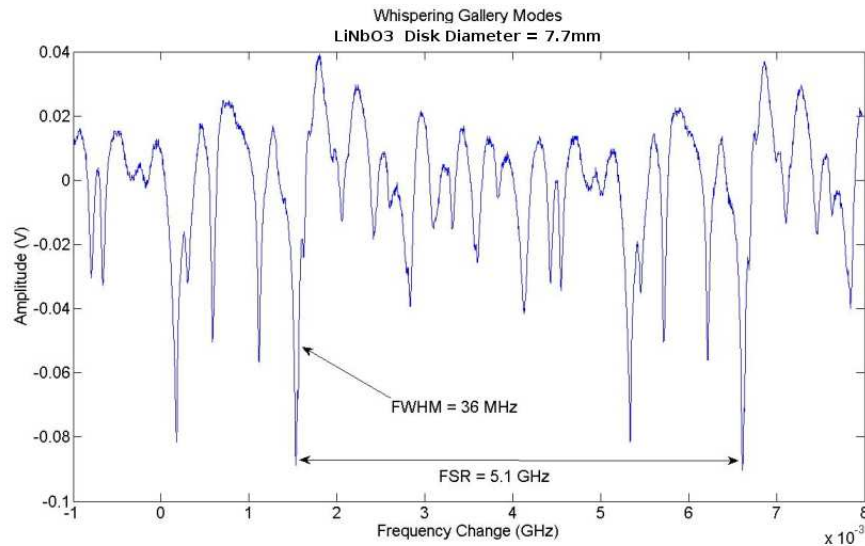


FIG. 4.7: Transmission spectrum from LiNbO₃ WGMR disk. Laser frequency was swept through the free-spectral range. Drops in the transmission are the whispering-gallery mode resonances. Multiple spatial modes within an FSR are visible.

4.3 Whispering-gallery mode resonator polishing

We formed whispering-gallery mode resonators from wafers of crystalline lithium niobate (LiNbO₃). We used a diamond-tipped hole bit to cut out a circular piece. The wafers are cut such that the extraordinary axis (c-axis or z-axis) is oriented along the thin section of the disk, and the ordinary axes are in the circular plane of the disk

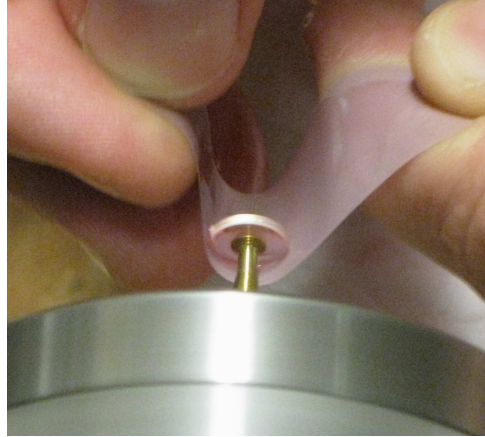


FIG. 4.8: $LiNbO_3$ disk mounted in lathe for polishing. Diamond-grit sandpaper was used to polish the rim of the disk.

(Figure 4.9).

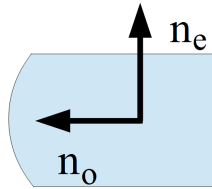


FIG. 4.9: Side view of WGMR disk with indices of refraction directions shown. The ordinary index (n_o) is in the plane of the disk. The extraordinary index (n_e) is along the vertical direction (out of the plane of the disk).

We attached the circular piece to a post using heat-wax, and turned it on a lathe. We used aluminum oxide sandpaper to reduce the diameter and to shape the rim to create a curved surface. However the particles in aluminum oxide sandpaper are too irregular in size for polishing. Diamond lapping paper provides more uniform and smaller size particles, which are necessary for a high-quality optical polish. We stepped down through several grits of diamond lapping paper to polish the rim, from $9\ \mu\text{m}$ down to $0.1\ \mu\text{m}$. Figure 4.8 shows a photo of the hand-polishing technique.

Polishing lubricant is necessary to keep removed material away from the area being polishing.

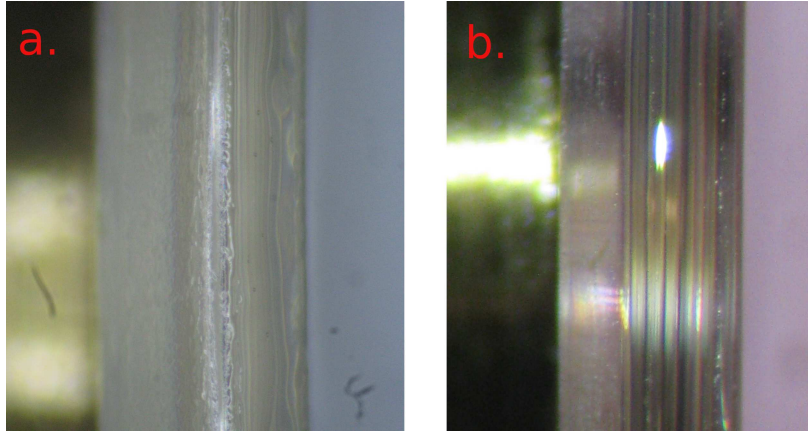


FIG. 4.10: Two polishing stages. Photo *a.* shows the disk after polishing with no cleaning in between the final three stages. Photo *b.* shows the disk after being re-polished and cleaned with acetone in between the final stages. There are still visible scratches on the top and bottom edges (right and left in the photo), but the center strip where the WGMs will propagate is now clear.

The quality of the polish is the main limiting effect of the quality factor of the resonator. With this polishing regimen we produced disks with quality factors around 10^6 , while the absorption-limited Q for LiNbO_3 is around 10^8 . In order to reach an absorption-limited Q -factor we had to add several improvements. First, we cleaned the disk using acetone in between polishing stages to prevent removed material from causing scratches. This improved the Q -factor by a factor of ten, to 10^7 . Figure 4.10 shows how the disk looks with or without acetone cleaning. We next used a diamond slurry in the final two stages (0.5 and $0.1 \mu\text{m}$). This improved the polishing material contact with the surface as compared to the paper, as well as helping prevent scratching. We were able to achieve a Q -factor of 10^8 with these improvements (Fig. 4.11).

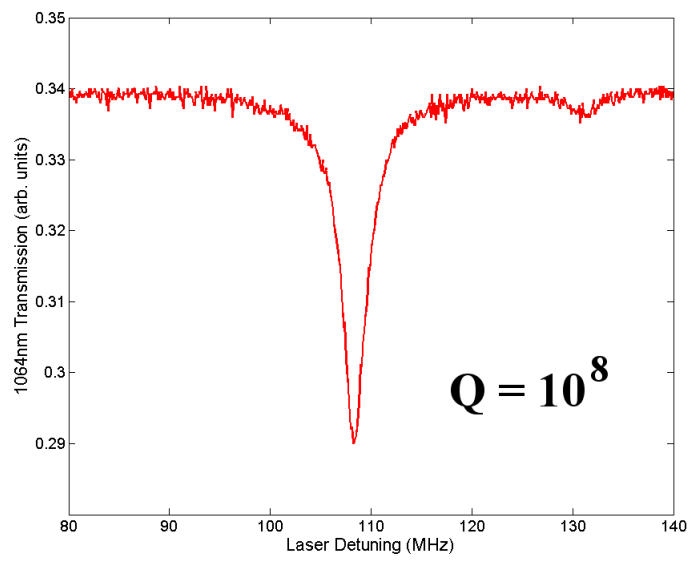


FIG. 4.11: Single WGM resonance with a full-width half-max of 3 MHz for a Q-factor of 10^8 (with a 1064 nm laser).

CHAPTER 5

Second harmonic generation inside a WGMR

In this section we detail our experiments to produce non-critically phase-matched second harmonic generation inside our crystalline whispering-gallery mode resonators.

5.1 SHG Experiment

We coupled our 1064 nm DPSS laser to a MgO:LiNbO₃ disk using an anti-reflection coated diamond prism as described in Sec. 4.1. The pump field was linearly polarized and parallel to the ordinary axis (n_o) of the disk, as required for phase-matching for SHG (Sec. 2.1.3). We heated the disk to achieve phase-matched second harmonic generation. Inside the disk a second harmonic (SH) field with a wavelength of 532 nm was generated. With the pump field polarized along the ordinary axis (n_o) of the disk (Fig. 4.9, the phase mismatch Δk is a minimum when the SH field is polarized along the extraordinary axis (n_e), and the temperature T_{pm} is such that

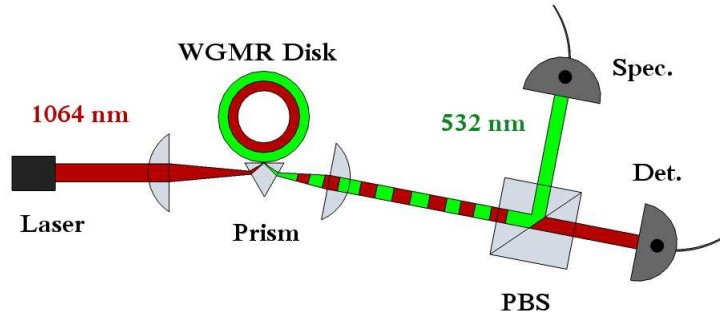


FIG. 5.1: Schematic for second harmonic generation experiment with WGMR disk.

$n_o(1064 \text{ nm}) = n_e(532 \text{ nm})$ (as in 2.5). For $\text{MgO}:\text{LiNbO}_3$, this temperature is $T_{pm} = 89^\circ \text{ C}$ (for a WGMR geometry).

Both the pump 1064 nm and SH 532 nm beams exit the prism, with a small separation due to dispersion in the prism. A lens is placed after the prism to approximately collimate both fields. A polarizing beam splitter (PBS) is placed after the lens to separate the two fields, as shown in the experimental diagram in Figure 5.1.

Maximum SHG efficiency in a crystalline WGMR requires optimal phase-matching conditions and optimal mode overlap. The phase-matching is controlled by the temperature of the crystal, which tunes the birefringence. A temperature controller is used to maintain a constant temperature. The pump field is tuned to a WGM resonance by tuning the laser frequency. Feedback from the transmission photodetector is used to keep the pump laser locked on resonance.

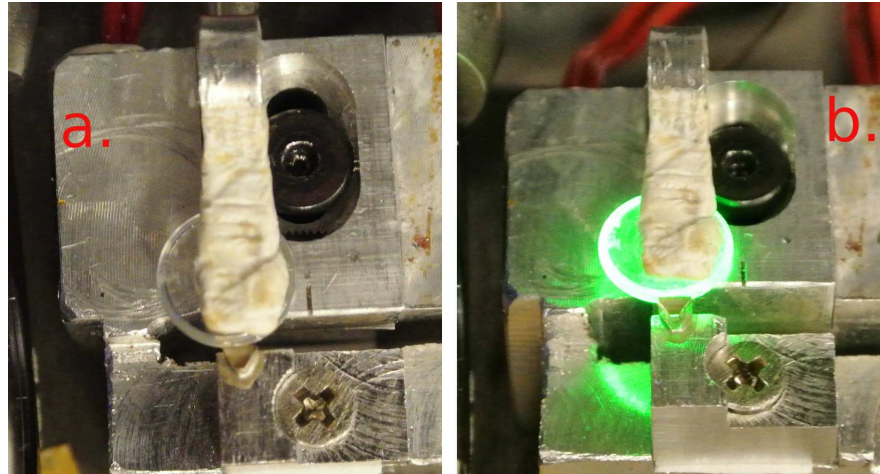


FIG. 5.2: Photo of WGMR with and without SHG. *Left* shows photo where disk temperature was far from phase-matching temperature. *Right* shows photo of the scattering of the second harmonic WG field when disk temperature was near phase-matching temperature.

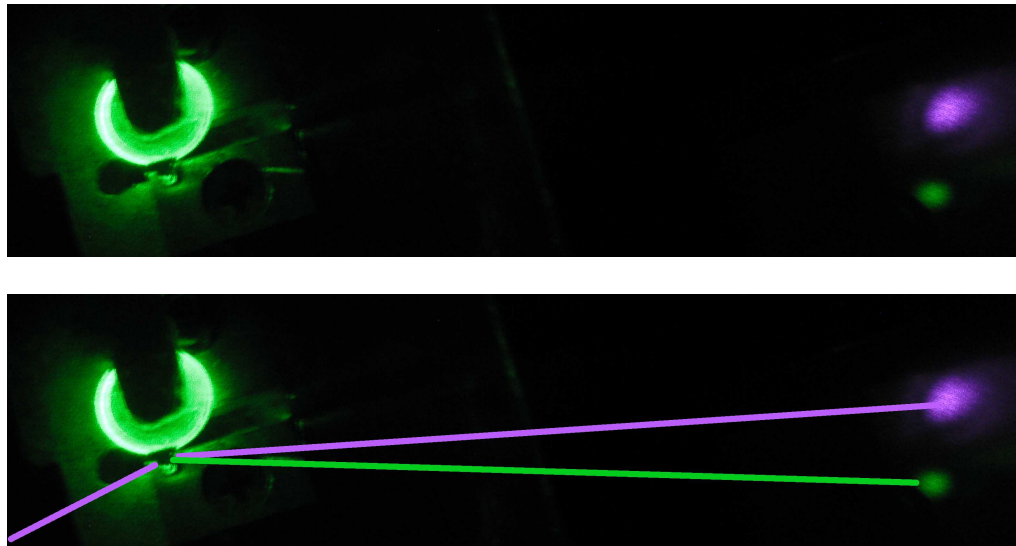


FIG. 5.3: Photo of SHG from the WGMR and pump transmission through the disk. Both the 532 nm second harmonic (green) and 1064 nm infrared pump (purple) spots are visible. They have been separated by dispersion in the coupling prism. *Bottom* is same photo with lines drawn to illustrate beam paths.

5.2 Detection of SHG

We detected the generated second harmonic on photodetector after separating it from the transmitted pump using a polarizing beam splitter. We used different photodetectors for initial detection/efficiency measurements and for noise measurements. For efficiency measurements we used a silicon Hamamatsu S7686 photodiode with a reverse bias, connected to a current preamplifier (*SRS SR570*). The S7686 is most sensitive around 532 nm, and is coated to reduce sensitivity to infrared. This was useful when our SH output was low. However it has a large area and high capacitance (200 pF), which reduces the detection bandwidth (Sec. 6.1). For noise measurements, we switched to a smaller photodiode with lower capacitance (Hamamatsu S1337).

Maximum SHG efficiency occurs where the temperature, pump laser frequency, and crystal indices of refraction are such that there is maximal pump-SH WG mode overlap and the dispersion between the pump and SH modes is minimized. However, these parameters are not independent. Temperature affects both dispersion and the cavity mode frequencies. This requires three tuning controls (temperature, pump laser frequency, external E-field) to be able to find the highest efficiency point.

Additionally, there are many families of whispering-gallery modes, and thus many local maxima (Sec. 2.3.2). Due to this large parameter space, finding the point with the maximum second harmonic conversion efficiency is very difficult. Because of the large modal number and the uncertainty in the absolute modal number, this point cannot be determined *a priori*.

We began the experimental search at the single-pass phase-matching temperature we found for our MgO:LiNbO₃ crystal, $T_{pm} = 110^\circ \text{C}$. There are many spatial modes that can be supported by the whispering-gallery mode resonator. As seen in Sec. 2.3.2, these modal frequencies are determined by the geometry of the resonator.

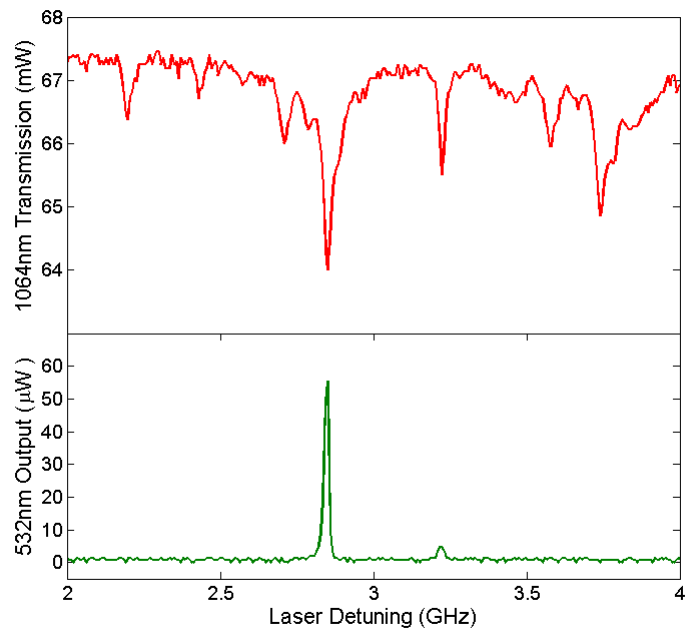


FIG. 5.4: WGMR output with SHG vs. pump laser detuning. *Top*: pump transmission with several modes. *Bottom*: SHG output occurs when the pump frequency is tuned to WGM resonance that overlaps with a second harmonic WG mode.

The wavevector k depends on the mode, which changes the phase-matching conditions. This effectively reduced our phase matching temperature to $T_{pm} \rightarrow 89^\circ \text{ C}$.

These modes also have different amounts of overlap with each other. However, if there is some overlap it is possible to generate the SH field in that mode. The 1064 nm WG mode that shares the same frequency with a 532 nm mode may not have the same spatial characteristics. The higher frequency mode will be confined closer to the edge of the disk - and the overlap will be less than unity.

The spatial modes are visible at the output. Figure 5.5 shows the SH output for different pump WG modes.

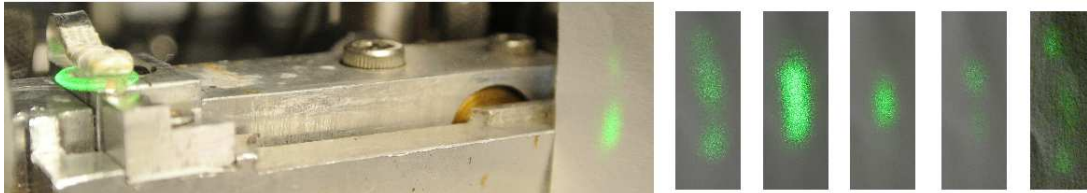


FIG. 5.5: Photo of different WGMR spatial modes of the second harmonic field. The pump frequency was tuned to different pump whispering-gallery modes within one FSR.

5.3 Whispering-gallery cavity locking

To keep the laser in resonance with a whispering-gallery mode, the laser frequency must remain matched with the resonance frequency. Both the laser frequency and the cavity mode frequencies can drift over time. We monitor the pump transmission through the WGMR and use feedback to control the pump laser frequency. There are two frequency controls on the DPSS 1064 nm laser. The Nd:YAG crystal temperature can vary the frequency over 30 GHz at a slow rate. The laser cavity also has a PZT, which can tune the frequency over shorter range ($< 1 \text{ GHz}$) though at a higher rate

(100 kHz). The feedback control system is shown in Fig. 5.6.

5.3.1 Pump laser frequency locking

The pump laser frequency was dithered with a function generator at 100 kHz using the PZT-tuning. The signal from the 1064 nm transmission photodetector was sent to a lock-in amplifier, with the dither signal as the reference. We adjusted the pump laser crystal temperature (LCT) to tune to a whispering-gallery mode. The lock-in produced an error signal relative to the center frequency of the mode. The error signal was fed to a PI feedback controller (schematic in Fig. 5.7). The proportional feedback was used to control the PZT-tuning of the pump laser, while the integral feedback was used to control the LCT.

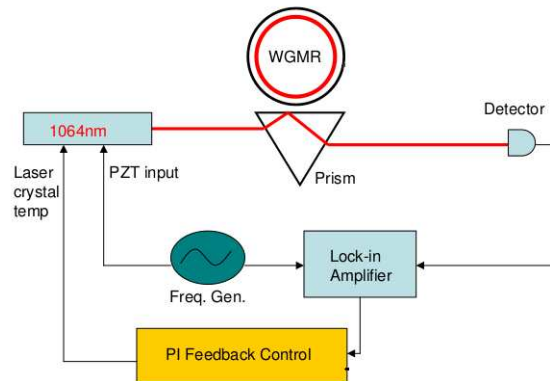


FIG. 5.6: Feedback schematic for WGMR cavity locking. Frequency generator modulated pump laser frequency and was used for the lock-in amplifier reference. Lock-in error signal is sent into feedback circuit, which is used to control the pump laser frequency.

The lock responds to drifts in WGMR temperature, drifts in the pump laser frequency, and changes in the cavity modes due to the Kerr effect. As more pump energy enters the cavity, the intensity shifts the whispering-gallery mode. This puts an upper limit on the pump power. Additionally, as the second harmonic is generated,

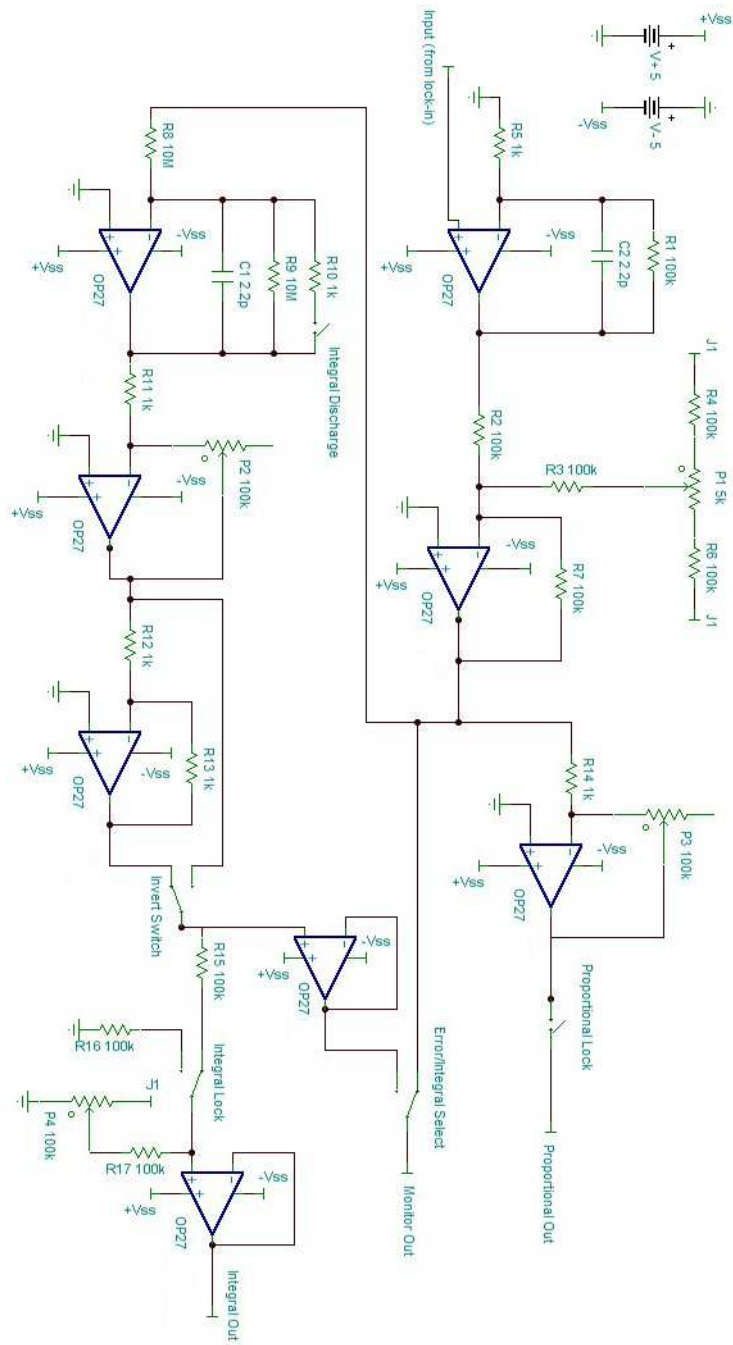


FIG. 5.7: PI control schematic for WGMR cavity locking. Input is from the lock-in amplifier, which is from the transmitted pump detector. The *proportional out* is sent to the pump laser PZT voltage. The *integral out* controls the pump laser crystal temperature voltage.

the energy in the pump mode is reduced, again shifting the frequency. An example of SHG with the pump locked to a WGM is shown in Fig. 5.8.

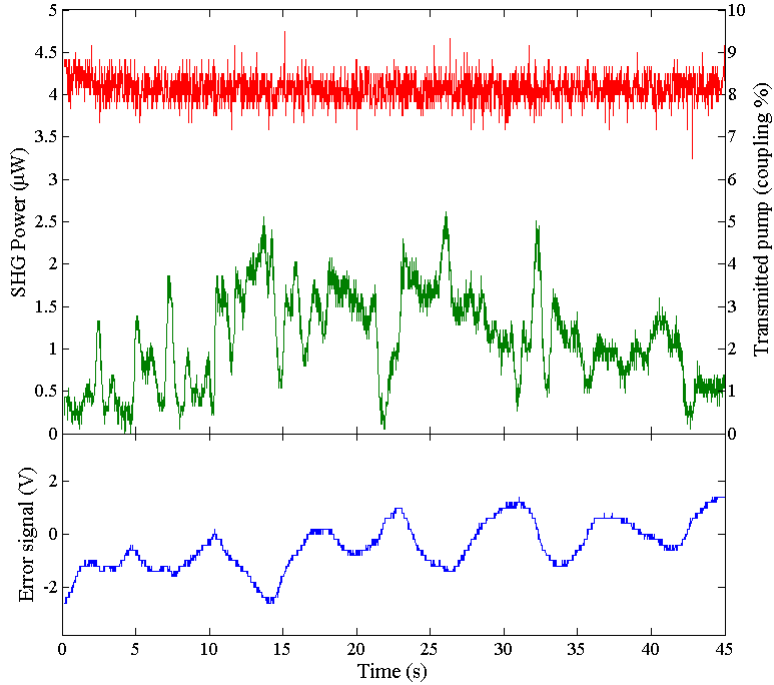


FIG. 5.8: SHG from WGM while pump is locked. Top axes show transmitted pump (*top line*) and SHG (*middle line*). Transmitted pump is measured by the amount of coupling as a percentage of the transmitted field. The optical power of the SHG is measured in μW . The lower axes show the error signal from the lock-in amplifier. Pump input power $P_{in} = 6.2\text{ mW}$ before coupling.

With increasing pump power the laser becomes more difficult to lock to a whispering-gallery mode. Fig. 5.9 shows the SHG output, transmitted pump, and lock-in amplifier error signal as a function of time. The input pump power was 8 mW, compared with 6.2 mW in Fig. 5.8. Around 20 s the lock was unable to continue to hold the pump laser on resonance.

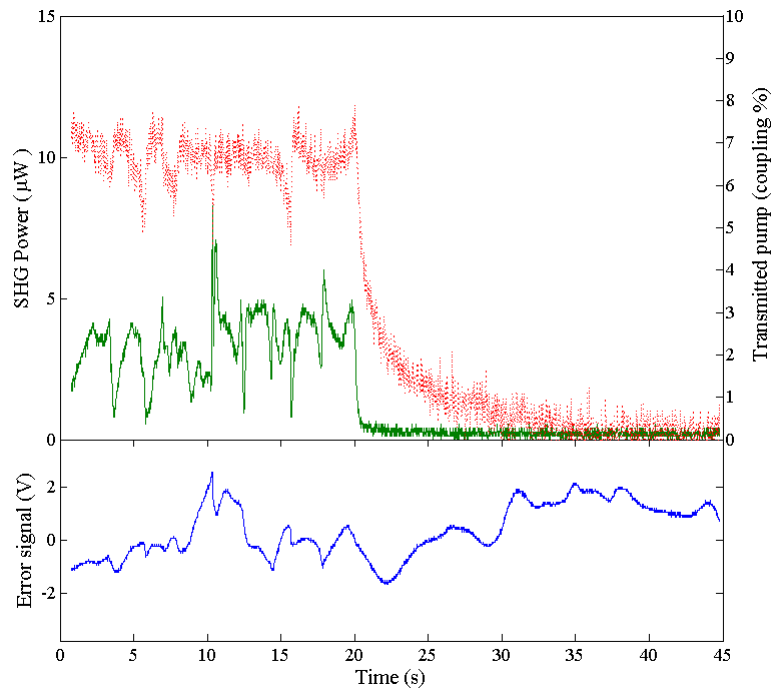


FIG. 5.9: SHG from WGMR before pump lock is lost. Even a small amount of extra pump power is enough to kick the laser out of lock. Top axes show transmitted pump (*top line*) and SHG (*middle line*). Transmitted pump is measured by the amount of coupling as a percentage of the transmitted field. The optical power of the SHG is measured in μW . The lower axes show the error signal from the lock-in amplifier. Pump input power $P_{in} = 8\text{ mW}$ before coupling.

5.3.2 Electric field tuning

Control of the second harmonic (SH) modes is provided by an electric field placed across the WGMR disk. The electric field interacts with the crystal and shifts the resonances. This is due to the electro-optic effect, where the index of refraction is a function of an applied electric field (Eq. 5.2) [48]. The electric impermeability tensor η_{ij} relates the electric field \vec{E} and electric displacement field \vec{D} inside a medium:

$$E_i = \sum_j \eta_{ij} D_j \quad (5.1)$$

The electric impermeability tensor η_{ij} is the inverse of the electric permeability tensor ϵ_{ij} , which is real and symmetric, and depends on the electric field:

$$\eta_{ij}(\vec{E}) = \eta_{ij}(0) + \sum_k r_{ijk} E_k \quad (5.2)$$

where r_{ijk} is the linear electro-optic (or Pockels) coefficient tensor. Since η_{ij} must also be real and symmetric, the tensor r_{ijk} must be symmetric in the indices i, j . Therefore they can be combined into one index l , in the same manner as Equations 2.23, such that $r_{ijk} \rightarrow r_{lk}$. The symmetry conditions are the same as in Sec. 2.1.1, so that the r tensor for lithium niobate has the form:

$$r_{lk} = \begin{bmatrix} 0 & -r_{22} & r_{13} \\ 0 & r_{22} & r_{13} \\ 0 & 0 & r_{33} \\ 0 & r_{51} & 0 \\ r_{51} & 0 & 0 \\ -r_{22} & 0 & 0 \end{bmatrix} \quad (5.3)$$

The impermeability tensor elements are related to the indices of refraction by $\eta_i = (\frac{1}{n^2})_i$. We apply a field along the extraordinary axis of the crystal, so $\vec{E} = (0, 0, E)$. Then Equation 5.2 simplifies to Eq. 5.4.

$$\eta_{jk}(E) = \begin{bmatrix} \frac{1}{n_o^2} + r_{13}E & 0 & 0 \\ 0 & \frac{1}{n_o^2} + r_{13}E & 0 \\ 0 & 0 & \frac{1}{n_e^2} + r_{33}E \end{bmatrix} \quad (5.4)$$

The ordinary and extraordinary indices of refraction are both tuned by the applied field but both remain independent. We are interested in how the second harmonic modes are affected by the external electric field. These modes are polarized in the direction of the extraordinary axis. To determine how the extraordinary index of refraction varies with the applied field we study η_{33} in Eq. 5.4 and in the limit when $r_{33}En_e^2 \ll 1$ (Eq. 5.5).

$$\frac{1}{n_e^2(E)} = \frac{1}{n_e^2} + r_{33}E \quad (5.5)$$

$$n_e(E) = \left(\frac{1}{n_e^2} + r_{33}E \right)^{-\frac{1}{2}} = n_e \left(1 + n_e^2 r_{33} E_{ext} \right)^{-\frac{1}{2}} \quad (5.6)$$

$$\approx n_e - \frac{1}{2} n_e^3 r_{33} \quad (5.7)$$

Thus the change in n_e due to E is $\Delta n_e = -\frac{1}{2} n_e^3 r_{33} E$. Next we calculate the change in the mode frequency in the WGMR disk due to this change in the index of refraction (Eq. 5.8):

$$\begin{aligned} \nu_{cav} &= \frac{m_{opt}c}{OPL} = \frac{m_{opt}c}{2\pi R n_e} \\ \Delta \nu_{cav} &= \frac{m_{opt}c \Delta n_e}{2\pi R n_e^2} \\ &= \frac{c n_e r_{33} E}{2\lambda} \end{aligned} \quad (5.8)$$

where $m_{opt} = 2\pi R n_e / \lambda$ is the mode number, R is the radius of the disk, and λ is the wavelength. The electric field is approximately the applied voltage (V_{DC}) divided by the distance between the electrodes (which is the thickness of the disk, 1 mm). The frequency shift is then given by Eq. 5.9. For our MgO:LiNbO₃ WGMRs the electro-optic coefficient is $r_{33} \sim 28$ pm/V (from Table 2.1), and we obtain a frequency shift per volt of ~ 18 MHz/V (Eq. 5.10).

$$\Delta\nu_{cav} = \frac{c n_e r_{33} V_{DC}}{2 \lambda d} \quad (5.9)$$

$$\Delta\nu_{cav} = V_{DC} \times 18 \frac{\text{MHz}}{\text{V}} \quad (5.10)$$

To apply a field along the c-axis, we placed a flat, circular electrode directly on top of the disk (between the disk and the clamp). A variable voltage was applied between the top electrode and the mount (serving as the bottom electrode) using a ThorLabs Piezo Controller. The voltage could be varied between 0 ~ 100 V, to give us a tuning range of ~ 1.8 GHz. Figure 5.10 shows the SHG output of the WGMR disk as the voltage across the disk is swept to change the SH mode frequency over ~ 1 GHz, while the pump mode was locked.

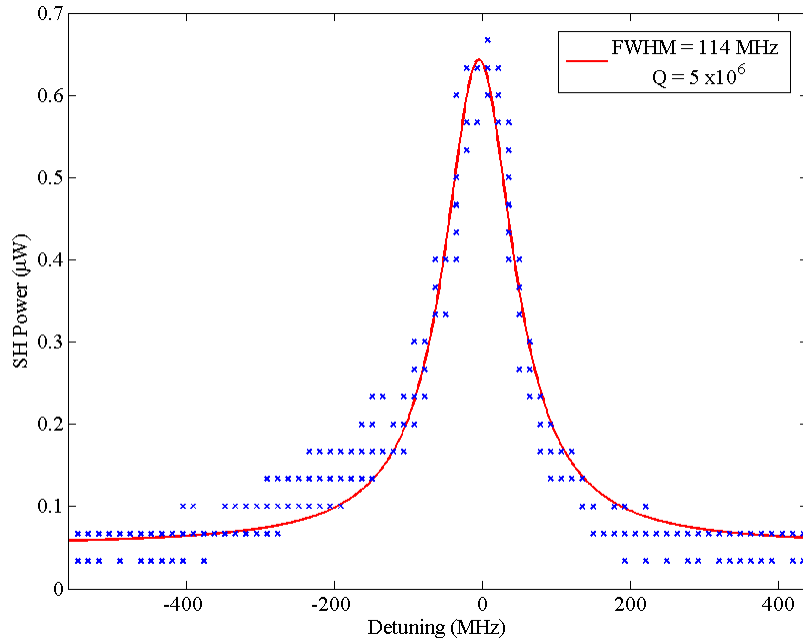


FIG. 5.10: SHG output vs. E-field detuning demonstrates a full-width half-max of 114 MHz, and a Q-factor of 5×10^6 .

5.4 SHG Efficiency measurements

Second harmonic output is significant only when the laser is in resonance with a fundamental mode that also overlaps with an available SH mode. The SHG efficiency then depends not only on the quality factors of the two optical fields, but also on the geometrical overlap of their modes inside the resonator. The expression for the efficiency (Equation 3.76) can be re-written in terms of the normalized saturation power $S = 54P_{in}/W_0$ [45]:

$$\frac{P_{SH}}{P_{in}} = \frac{6}{S} \left[\sqrt[3]{1 + S + \sqrt{S(1+S)}} + \sqrt[3]{1 + S - \sqrt{S(1+S)}} - 2 \right]^2, \quad (5.11)$$

where P_{in} and P_{SH} are the powers of the input fundamental and output second harmonic optical fields, respectively. Our derived saturation power W_0 is Equation 3.77, and is dependent on the nonlinear conversion rate and the cavity loss rates.

Fig. 5.11 shows measured SHG conversion efficiency as a function of the pump field power for two different separations between the disk and the prism. Increasing the disk-prism separation increased the conversion efficiency, as the Q increased by a factor of 1.55 from $Q = 4.6 \times 10^6$ to $Q = 7.0 \times 10^6$. We extracted the value of the saturation parameter W_0 by fitting the SHG efficiency measured experimentally using Eq.(5.11). For $Q = 7.0 \times 10^6$ we fit to $W_0 = 900$ W, for the $Q = 4.6 \times 10^6$ we found $W_0 = 2200$ W. The ratio between the two saturation powers is consistent with $W_0 \sim \frac{1}{Q^2}$ predicted by Equation 3.77.

However, these saturation powers are much lower than expected from Equation 3.77, and previous experiments [43], which found an experimental saturation power of $W_0 \simeq 3$ mW. Our model did not take into account the whispering-gallery

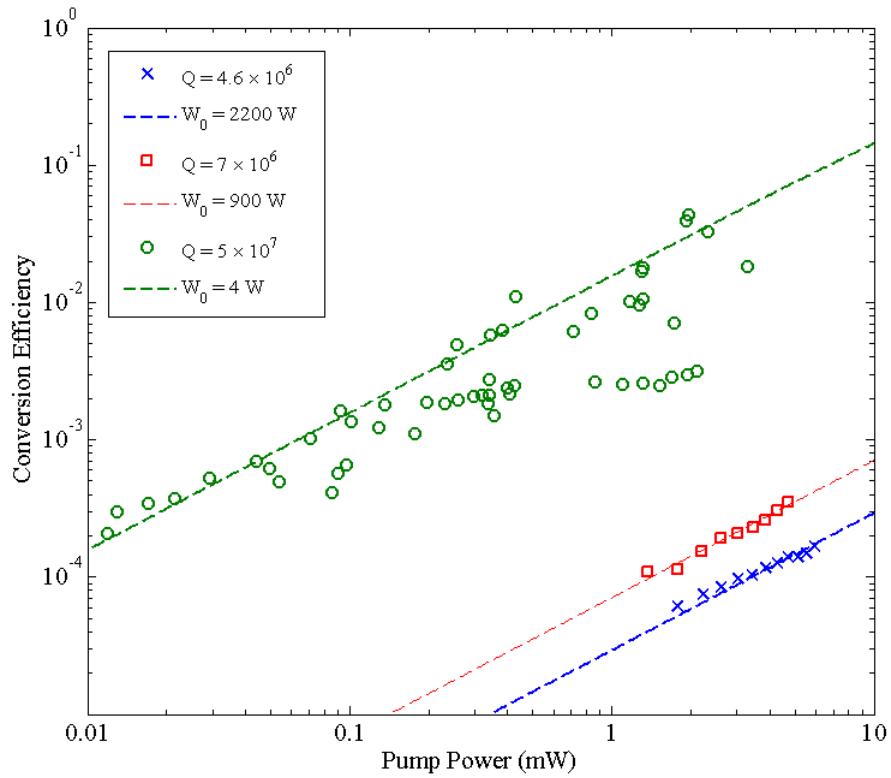


FIG. 5.11: Saturation power measurements by way of SHG Efficiency vs. input power. Lines show efficiency vs. input power for the closest saturation powers. Saturation power scales by Q^3 as predicted. Quality factor was varied by moving the disk away from the prism to lower the coupling.

mode volumes ($V^{(\omega)}$, $V^{(2\omega)}$) or spatial mode overlap ($V^{overlap}$) between the pump and second harmonic modes. The saturation power has been found to depend on these variables as [45]:

$$W_0 \propto \left(\frac{V^{(\omega)}}{V^{over}} \right)^2 V^{(2\omega)} \quad (5.12)$$

A low mode-overlap explains why we observed much larger saturation powers. This effectively reduces the conversion rate.

CHAPTER 6

Quantum noise measurements

This chapter introduces the tools for detecting quantum noise and the details of their operation. I address the experimental considerations that constrain our ability to measure the quantum noise. I present the experimental method, and examine the measurements of the quantum noise associated with second harmonic generation inside whispering-gallery mode resonator.

With second harmonic generation from a whispering-gallery mode resonator demonstrated, the next step is to measure the effect on the quantum fluctuations. Fluctuations give rise to noise in amplitude and phase measurements. Measurements are carried out using photodetection electronics. As predicted in Chapter 3, noise reduction due to second harmonic generation should be visible in the amplitude quadrature. A photodetector (usually a photodiode) itself produces a current proportional to the intensity of the light. The noise on this measurement will be related to the amplitude quadrature noise of the light $\sim \langle |\Delta X_1|^2 \rangle$.

The measured noise is a combination of the quantum noise, electronics noise (thermal noise, amplifier noise) in the detection apparatus, and any other classical

noise affects the field (such as laser pump noise). It is necessary to minimize the effects of all other sources of noise in order to measure the quantum noise. The quantum noise is intrinsic to the light and cannot be removed by classical means. It is related to the uncertainty in the photon flux, and for a coherent state (such as a laser) with minimum uncertainty this noise is referred to as the *shot noise*.

There are many difficulties in measuring the quantum noise. The efficiency with which photodiodes convert light into an electric current immediately limits the ability to detect quantum noise. This is called the *quantum efficiency* (or Q.E.), and depends on the photodiode material, size, and construction. We measure the noise by measuring the power at different frequencies using a spectrum analyzer. The bandwidth of frequencies we can measure reliably depends on the gain and bandwidth of our photodetector amplifiers. As gain and bandwidth are often inversely related, this limits our ability to measure small signals at sufficient bandwidth.

6.1 Photodetectors

In order to detect the quantum noise accurately, the photodiodes must be efficient at converting photons to photoelectrons. This conversion ratio is the *quantum efficiency* (Q.E.). Photodiode material is critical in determining the quantum efficiency, and Q.E. will vary with light frequency. For 1064 nm, indium gallium arsenide (InGaAs) photodiodes have the highest quantum efficiency. We used JDSU ETX-500 photodiodes, which have a quantum efficiency of $\sim 85\%$. For the 532 nm second harmonic, the highest quantum efficiency photodiodes are made of silicon (Si). We used Hamamatsu S1337 photodiodes for our SH photodetector, with a Q.E. of $\sim 80\%$.

The photodetector circuit for the pump beam measurements is shown in Fig. 6.1. Detection sensitivity and speed are always opposing each other. High sensitivity is

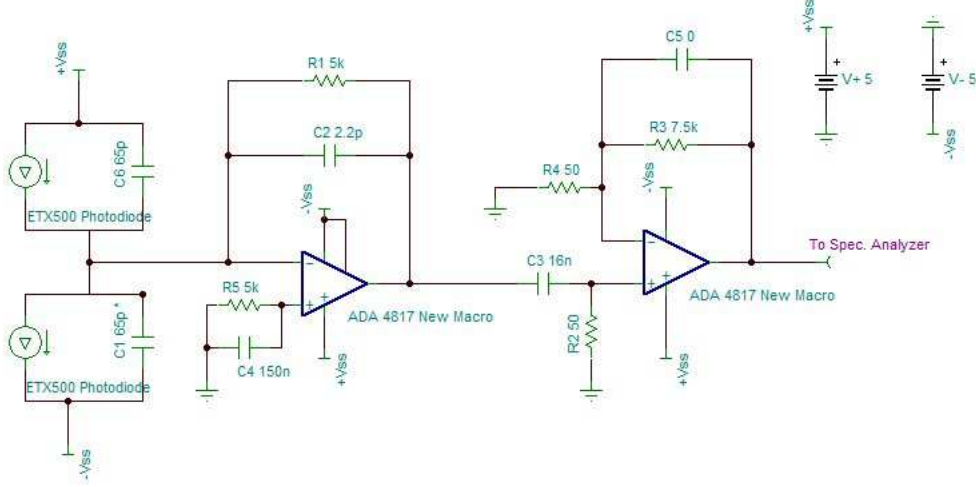


FIG. 6.1: Photodetector schematic for the fundamental laser. The photodiodes are JDSU ETX500.

achieved with large feedback resistor ($R_f = R1$). A high resistance reduces the detector bandwidth, resulting in a slower detector response. This can be compensated by lowering the capacitance ($C_f = C2$). It is limited, however, by the photodiode capacitance (C_{PD}). Photodiode capacitance is primarily a function of size – the smaller the active photodiode area, the lower the capacitance. Too small an area and it becomes difficult to capture the entire beam on the detector.

The formula to determine the optimal feedback resistance (C_f) for the preamplifier (an op-amp with gain-bandwidth product GBP) is Eq. 6.2. We used AD4817 for our amplifier op-amps, which have a gain-bandwidth product of $GBP = 410$ MHz [87].

$$\frac{1}{2 \pi R_f C_f} = \sqrt{\frac{GBP}{4 \pi R_f C_{PD}}} \quad (6.1)$$

$$C_f = \sqrt{\frac{C_{PD}}{\pi R_f GBP}} \quad (6.2)$$

For the SH detector, the S1337 photodiodes have a capacitance of $C_{PD} = 65$ pF, and the feedback capacitance should be around 4.5 pF. Practically, if C_f is too small the amplifier will oscillate, so we tested a few small capacitors (from 0 – 7 pF) and found $C_f = 2$ pF to be optimal. For the pump detector, the ETX-500 photodiodes have a capacitance of $C_{PD} = 44$ pF each. With both connected, Eq. 6.2 gives a feedback capacitance of ~ 3.7 pF. In practice we found 2.2 pF to be optimal.

6.2 Electronics noise

Detection of the quantum noise of light begins with the conversion of photons to electrons by way of a photodiode. This element creates a current proportional to the intensity of the light. The fluctuations in intensity will be transferred to the photocurrent I_{ph} , and is described by the variance of the shot noise current i_{ph} (in A/Hz).

$$\langle i_{ph}^2 \rangle = 2 e I_{ph} \quad (6.3)$$

The photocurrent will be detected by a resistor R , and the resulting noise voltage v_{ph} (in V/ $\sqrt{\text{Hz}}$) is given by Eq. 6.4.

$$v_{sh} = \sqrt{2 e I_{ph}} R \quad (6.4)$$

Johnson-Nyquist noise (also called thermal noise) is introduced by the resistor R . As current is converted to voltage, thermal fluctuations affect the voltage noise.

This noise scales by the square-root of the temperature and resistance, and is given by Eq. 6.5:

$$v_{johnson} = \sqrt{4 k T R} \quad (6.5)$$

with units of V/\sqrt{Hz} , where k is the Boltzmann constant (1.38×10^{-23} J/K). For a reliable quantum noise measurement, the optical signal must be above the Johnson noise level, such that

$$I_{ph} > \sqrt{\frac{2 k T}{e R}} \quad (6.6)$$

There is also 1/f noise from the amplification in the photodetector (Sec. 6.1). For our op-amps (ADA4817) this is 4 nV/ \sqrt{Hz} . This is important to keep in mind, as we saw in Sec. 5.4 that our SHG efficiency was lower than expected. In order to measure noise in the second harmonic field, we have to have a high enough signal to get above the electronics noise.

6.3 Laser noise

Laser noise can arise from the pumping mechanism and the lasing action itself.

In a diode-pumped solid state laser, there is excess noise produced by a relaxation oscillation. This is an oscillation of energy between the light intensity and the population inversion when cavity decay rate is much greater than the spontaneous decay rate. In our Nd:YAG 1064 nm laser, this oscillation creates a noise peak around 770 kHz. An intensity noise eater, which monitors the laser output signal and sends feedback to the pump laser diode, was used to reduce this noise. Fig. 6.2 shows the

effect of the noise eater circuit on the measured noise.

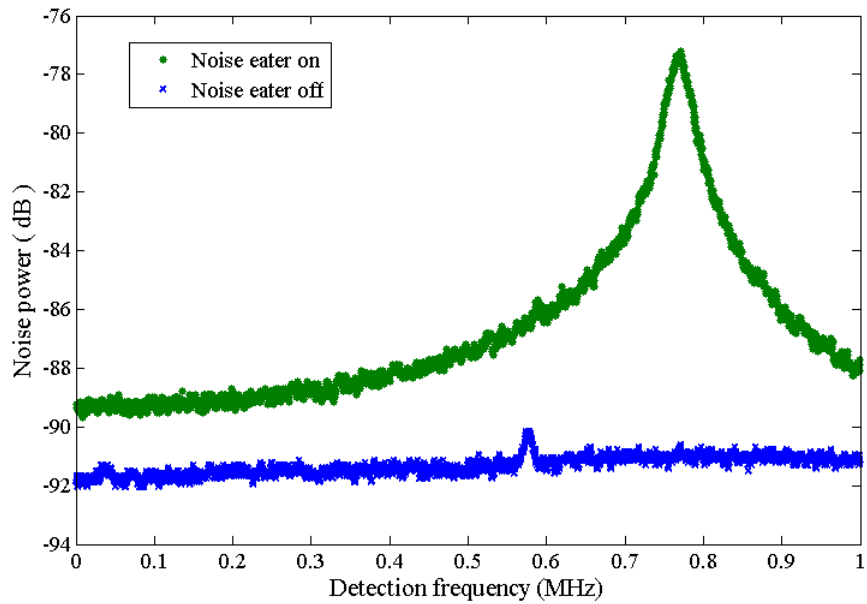


FIG. 6.2: Pump laser noise with and without noise eater. Intensity noise measured using the spectrum analyzer. Noise eater suppresses the relaxation oscillation in the Nd:YAG laser cavity.

6.4 Shot noise

As discussed in Sec. 3.3, a coherent state has minimum uncertainty in both amplitude and phase quadratures (Eq. 3.43). Amplitude noise is proportional to the variance of the fluctuation in the \hat{X}_1 quadrature with a phase of $\phi = 0$, such that $Var(\hat{X}_1) = \langle \Delta \hat{X}_1^2 \rangle$. For a coherent state, this noise is equal to unity

$$Var(\hat{X}_1) = 1 \tag{6.7}$$

This is called the *shot noise* or *standard quantum limit* (SQL). Noise measure-

ments are made in reference to this level. A photodiode itself measures the intensity, and the intensity noise is equivalent to $\hat{\mathbf{X}}\mathbf{1}^2$ with a phase of $\phi = 0$.

Our noise measurements were done by direct detection, using one photodiode. Shot noise power varies linearly with optical power (Sec. 6.4), so a doubling of the optical power increases the shot noise by 3 dB. Fig. 6.3 shows noise traces from the spectrum analyzer for a doubling of the laser power. The difference between the top two traces is 3 dB (for frequencies between 3 and 9 MHz), indicating that our laser is shot noise limited in this region. We verified this by balancing the photodetector. By balancing, all other noise effects are cancelled out, leaving only shot noise. We used a polarizing beam splitter to send the beam to two photodiodes. The photodiodes were physically connected to the same preamplifier. One was biased with a positive voltage, while the other was biased with a negative voltage, resulting in the subtraction of their signals at the pre-amp stage.

We then calibrated the shot noise (again with direct detection) by varying the optical power, obtaining a relationship between the DC voltage measured and shot noise power. This was necessary as our second harmonic was not stable, but varied in time, so we could not actively measure the shot noise.

6.5 Experimental results

Using our WGMR apparatus, we set up to measure the effect of second harmonic generation inside the WGMR disk on the quantum noise level of both the pump and second harmonic fields. For measurements of the transmitted pump intensity noise, we used the set up in Fig. 6.4. The 1064 nm laser was linearly polarized along the direction of the WGMR ordinary axis (horizontal) and directed through a focussing lens to the coupling prism. Coupling was achieved as in Sec. 4.1. Conditions were

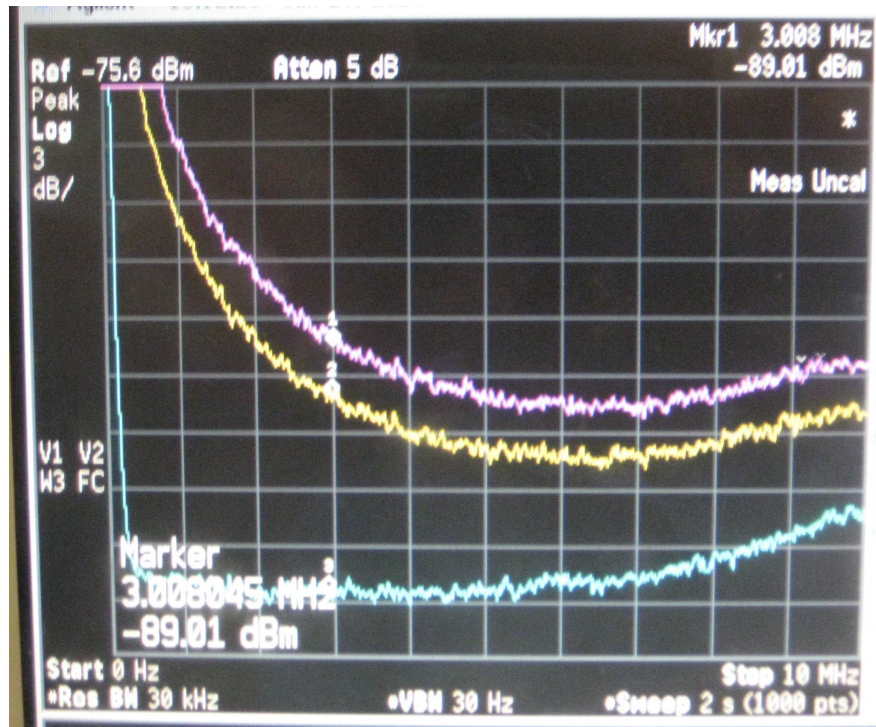


FIG. 6.3: Spectrum analyzer traces showing 3 dB increase with a doubling of laser power above a detection frequency of 3 MHz. Bottom trace (blue) shows the electronics noise.

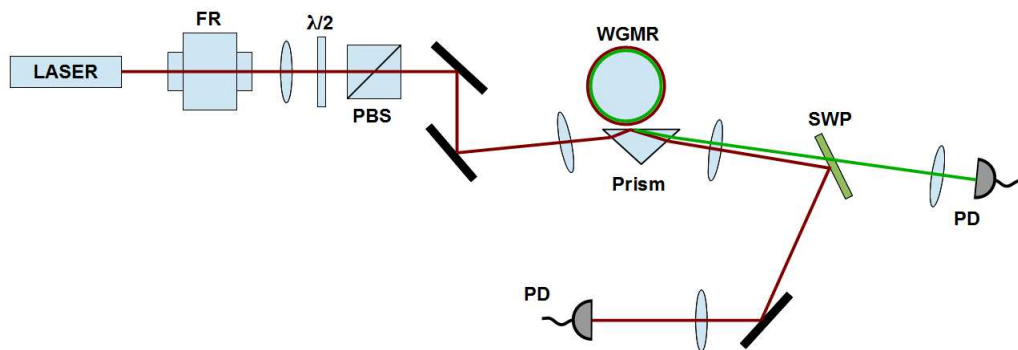


FIG. 6.4: Optical schematic for pump noise detection.

met for second harmonic generation as in Chapter 5. The output was collimated and the pump and SH fields were separated by a 45° short-wave pass filter. The SH field was focussed on an amplified photodetector. The transmitted pump was focussed onto one channel of the balanced photodetector (Fig. 6.1). We measured the noise level of the laser by direct detection.

6.5.1 Transmitted pump noise measurements

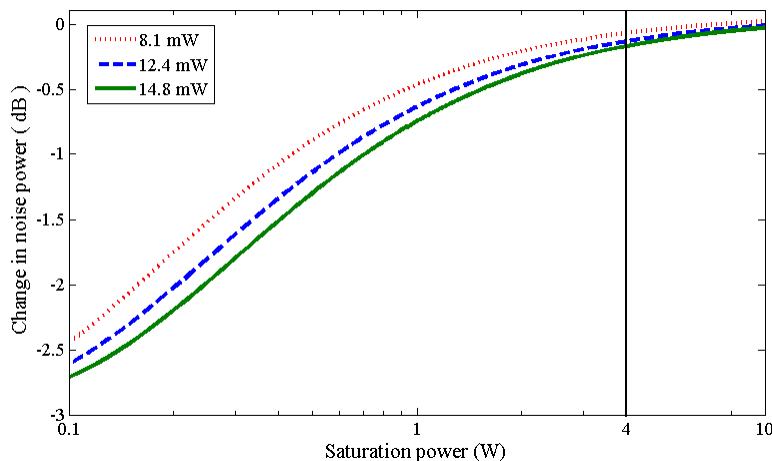


FIG. 6.5: Predicted pump noise variation as a function of saturation power relative to shot noise for experimental pump input powers. Detection frequency of 5.5 MHz, Q-factor of 4×10^7 . The line at 4 W shows our experimental saturation power.

We tuned the pump laser frequency to a whispering-gallery mode that overlapped with a second harmonic whispering-gallery mode, and set the laser lock (Sec. 5.3.1). The spectrum analyzer was set to monitor a single frequency, with a resolution bandwidth of 30 kHz and a video bandwidth of 30 Hz. An oscilloscope monitored four channels: the transmitted pump DC level, the spectrum analyzer (from the transmitted pump AC signal), the second harmonic field, and the WGMR temperature.

While the pump laser frequency was locked to a mode the second harmonic

modes were free to drift. In the following data the E-field tuning (Sec. 5.3.2) was not implemented, so we were unable to stabilize the second harmonic generation. We observed the noise at a set detection frequency over time. As the SH modes drifted into coincidence with the locked pump WG mode, the SH field was generated, and we measured the effect on the noise level.

We determined in Sec. 5.4 that we had not found the optimal parameters for second harmonic generation in our system. Our measured saturation power was several orders of magnitude higher than previous experimental work. This reduced the possible magnitude of noise reduction of the system. Fig. 6.5 shows the predicted noise reduction from shot noise for varying saturation powers. In Sec. 5.4 we measured our experimental saturation power to be near 4 W. In Fig. 6.5 we would expect to see less than 0.1 dB of squeezing, less than we could reliably resolve.

There were signs that the noise level was increased above shot noise in the presence of second harmonic generation. Fig. 6.6 shows a trace where the pump is locked to a WGM and the second harmonic field drifts. Without significant SHG, the measured noise is near shot noise. As the second harmonic is generated, the pump noise increases above shot noise. This is due to a process (or combination of processes) not accounted for in our theoretical predictions. One suspect is FM-to-AM conversion (frequency modulation to amplitude modulation).

Fig. 6.7 shows another trace where the pump noise increased with the presence of second harmonic generation. One interesting note here is that the noise, after increasing while the pump was locked, decreased when the second harmonic power peaked. The second harmonic trace suggests that the SH mode initially had poor overlap with the pump mode, and the SH generation was initially very low. This poor overlap would correspond to a high slope mode amplitude vs. frequency. Any small frequency shift (or noise) would then result in a larger amplitude change (or

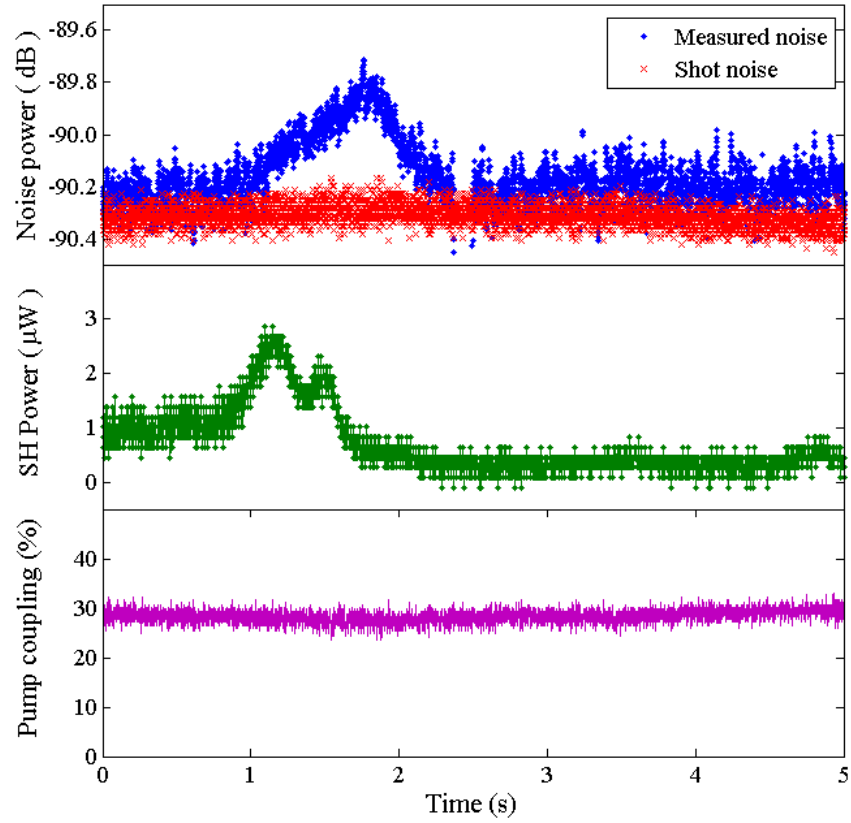


FIG. 6.6: Extra noise in pump with SHG while pump was locked. 5.5 MHz detection frequency. *Top* plot shows measured noise from direct detection (blue dots) and shot noise (red \times s). The shot noise was calculated from the DC voltage, using calibration by balanced detection. *Middle* plot shows the second harmonic power, and *bottom* is the transmitted pump coupling. Input pump power was 8.1 mW. The gap in the measured noise trace is due to the spectrum analyzer refresh.

noise). Figure 6.8 demonstrates good mode overlap and poor mode overlap. Once the SH mode shifts to overlap more closely with the pump mode, the noise is less affected by the frequency-to-amplitude conversion noise.

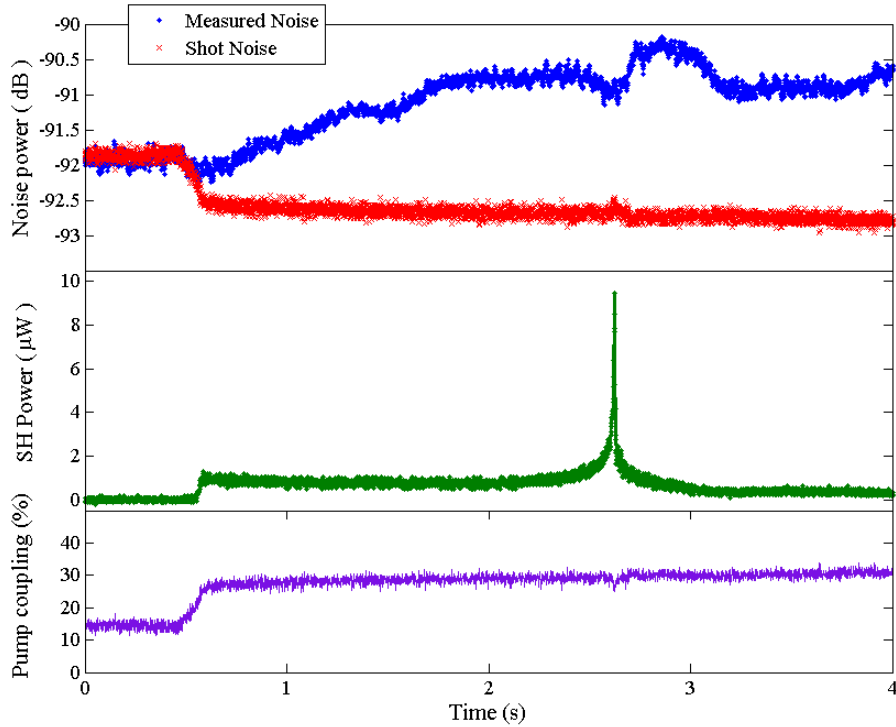


FIG. 6.7: Pump noise measurement with strong SHG and extra noise while pump was locked to a WGM. Detection frequency was 5.5 MHz. *Top* plot shows measured noise from direct detection (blue dots) and shot noise (red \times s). The shot noise was calculated from the DC voltage, using calibration by balanced detection. *Middle* plot shows the second harmonic power, and *bottom* is the transmitted pump coupling. Input pump power was 12.4 mW.

Another possible case of noise reduction with second harmonic generation is shown in Fig. 6.9. In this trace there was more pump coupled into the whispering-gallery mode (45 % compared to 30 %), the pump lock remained stable. The measured pump noise was stable but slightly above shot noise. When the second harmonic was generated, there is a very small dip in the noise.

We did not observe any significant evidence of squeezing from our experiment.

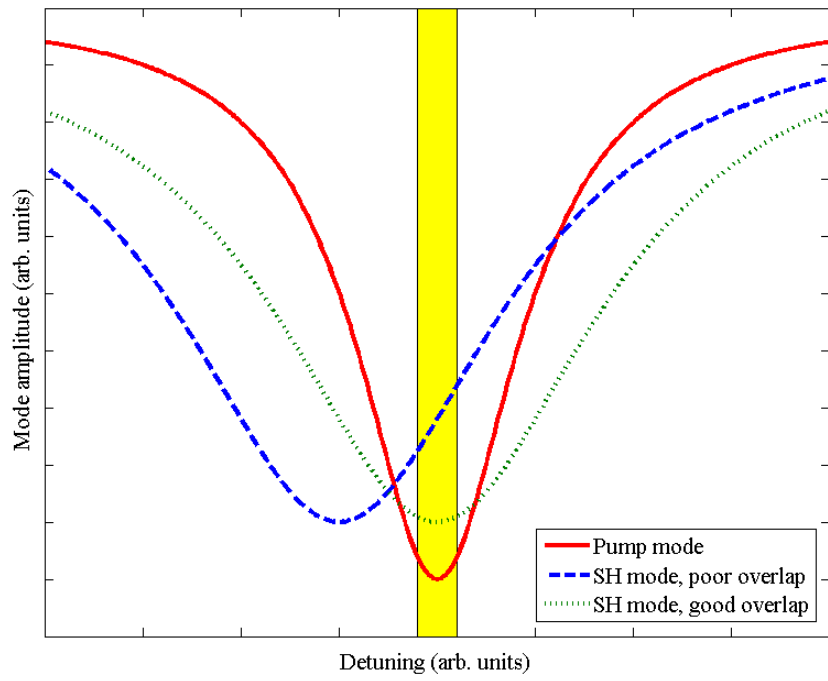


FIG. 6.8: Example of second harmonic mode overlap to show FM-to-AM conversion. The highlighted band represents the pump frequency lock.

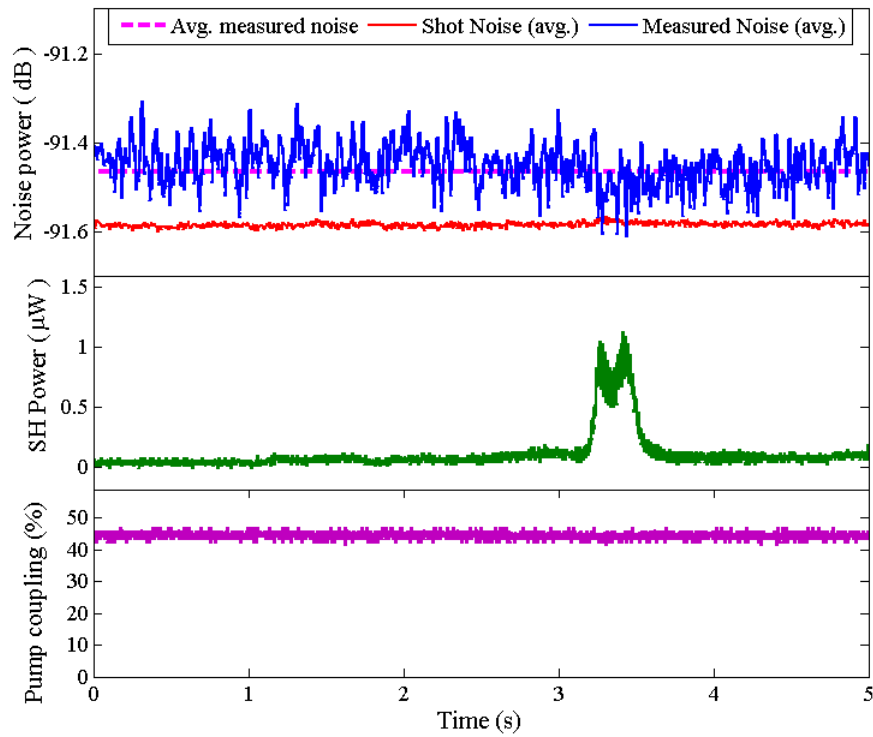


FIG. 6.9: Pump noise measurement at 5.5 MHz detection frequency. *Top* plot shows measured noise from direct detection (blue dots) and shot noise (red \times s), both smoothed with a moving average. The shot noise was calculated from the DC voltage, using calibration by balanced detection. *Middle* plot shows the second harmonic power, and *bottom* is the transmitted pump coupling. Input pump power was 14.8 mW.

This matches with our predictions from Sec. 3.5.2 (Fig. 6.5), as our second harmonic efficiency was less than in prior work [43, 45]. We also observed increases in noise in some data. We attribute this to FM-to-AM conversion noise. This arises due to the cavity spectrum and the mismatch between pump and SH modes, and must be minimized in future squeezing experiments.

6.5.2 Second harmonic noise measurements

We also attempted to measure the noise of the generated second harmonic (SH) field. The temperature of our WGMR was set to 89° C for phase-matching. We tuned the pump laser to a whispering-gallery mode that overlapped with a second harmonic whispering-gallery mode, and set the laser lock (Sec. 5.3.1). The schematic for our experimental setup is in Fig 6.10. The SH field was detected by the balanced photodetector (BPD) and the transmitted pump was monitored by another photodetector. The BPD signal was sent to an electronic spectrum analyzer.

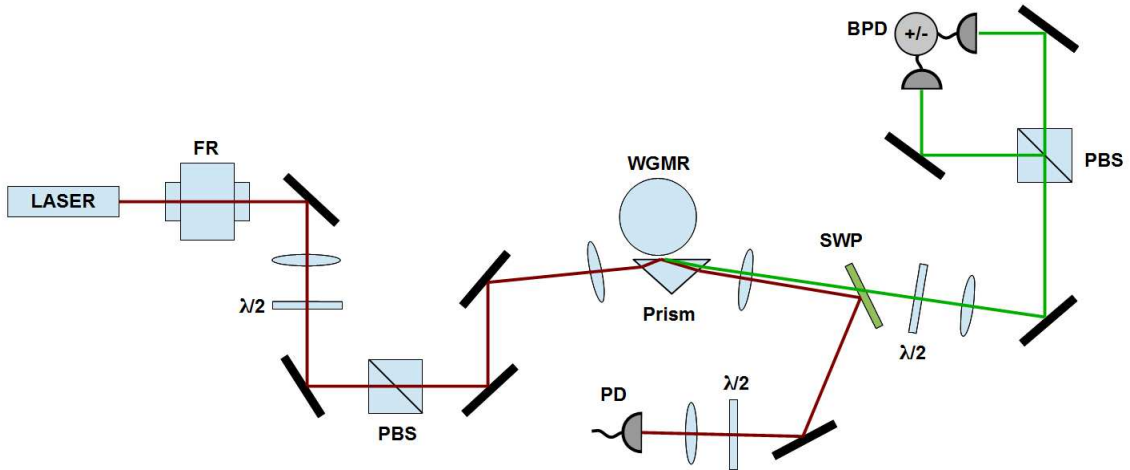


FIG. 6.10: Optical schematic for SH noise detection.

We found that with our high saturation power, we needed too much pump power

to produce enough SHG signal for detection. With high input power, our cavity became unstable. With a lower input power, we could stabilize our cavity, but could only produce a few μW of SHG. While we were able to detect the DC level with a high-gain amplifier, the high gain reduced our bandwidth, and at low detection frequencies, the noise was dominated by classical noise.

CHAPTER 7

Hyper-Raman scattering in a WGMR

While working on observing second harmonic generation from the LiNbO_3 WGMR, we noticed that in addition to the 532 nm SH field, the disk was also emitting yellow light. Using a spectrometer to detect the transmitted beam, we found that the disk was producing light at several frequencies near 532 nm. We determined that this must be due to hyper-Raman scattering, a process usually observed using high-intensity pulsed lasers. The combination of the high-intensity reached inside the WGMR, along with the scattering geometry of the crystal allowed this process to occur for our continuous-wave (CW) pump laser.

7.1 Raman scattering

Raman scattering occurs when light is inelastically scattered off of a material such that the scattered light has shifted frequencies by losing/gaining energy to/from

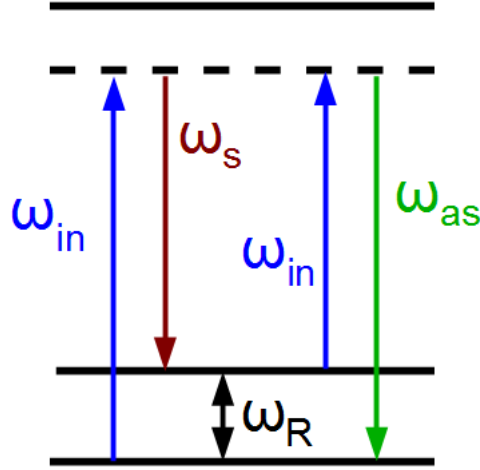


FIG. 7.1: Raman scattering diagram where an input field of frequency ω_{in} is scattered into a Stokes ($\omega_s = \omega_{in} - \omega_R$) field and anti-Stokes ($\omega_{as} = \omega_{in} + \omega_R$) field.

the material [46, 48, 49]. This is typically a weak process, with a cross-section of $\sim 10^{-6} \text{ cm}^{-1}$ [48].

This effect can be seen in crystals [88], where the scattered light shifts frequency through interaction with vibrational modes (phonons). Figure 7.1 shows a schematic of Raman scattering. An incident field with frequency ω_{in} scatters off of a phonon of frequency ω_R . There are two possibilities for the scattered field – a Stokes field with frequency $\omega_s = \omega_{in} - \omega_R$, and an anti-Stokes field with frequency $\omega_{as} = \omega_{in} + \omega_R$ [46, 48, 49].

There are several factors that determine the nature of the scattering – the possible phonon modes of the crystal, the incident direction of the light relative to the crystal axes, the polarization of the incident light relative to the crystal, and the direction and polarization of the scattered light.

7.2 Hyper-Raman scattering

Hyper-Raman scattering is the interaction between two incident photons and a vibrational mode of a material. The two photons (ω_i) are converted into a single photon of a higher frequency (ω_{out}), which is shifted by the frequency of the vibrational mode (ω_R) such that $\omega_{out} = 2\omega_i - \omega_R$. This process is intensity dependent.

Raman scattering is usually described in terms of the polarizability instead of the susceptibility (from Sec. 2). The susceptibility relates to the total electric field, whereas the polarizability relates the polarization of a medium to the external field only [89].

Selection rules for Raman and hyper-Raman transitions are determined by the relation between the polarizability and the symmetries of the phonon modes in a particular crystal lattice. The polarization response of a material to an external electromagnetic field can be generally expanded in the electric field to:

$$P_i = \alpha_{ij}E_j + \frac{1}{2}\beta_{ijk}E_jE_k + \frac{1}{6}\gamma_{ijkl}E_jE_kE_l + \dots, \quad (7.1)$$

where α is the polarizability, β and γ are the first- and second- hyper-polarizability tensors, correspondingly [90, 91]. Traditional notation for tensors α_{ij} and β_{ijk} uses indices i, j, k for the crystallographic axes x, y, z with the first index i corresponding to the polarization of the scattered radiation, and indices j, k describe polarization of the input photon (for Raman) or polarization of two incident photons (for hyper-Raman). Further, the scattering cross-section for hyper-Raman and Raman scattering for various geometries is usually written as $d_1(ijk)d_2$ and $d_1(ij)d_2$, with d_1 and d_2 describe correspondingly the directions of incident and scattered radiation.

Lithium niobate has a trigonal crystal structure (space group $C_{3v}^6(R3c)$), and thus

the optical phonon modes can be classified into 3 groups of modes: $\Gamma = 4A_1 + 5A_2 + 9E$ (the number indicates the number of modes in each group, and each group can be further separated into transverse and longitudinal) [92, 93]. Each mode group couples to different polarizations combinations of the incident and scattered fields, and thus each has different polarizability and hyperpolarizability tensors [92, 94].

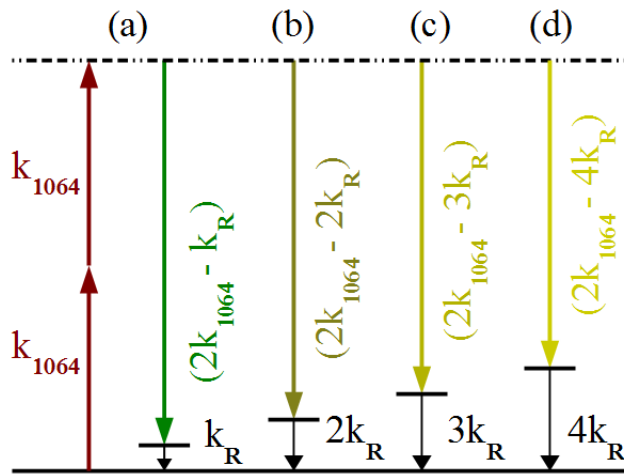


FIG. 7.2: Schematics of hyper-Raman scattering photon conversions (*a.*), in which two photons from the incident field interact with a medium to produce one new photon and a phonon; and (*b. - d.*) multi-phonon hyper-Raman overtone transitions.

7.3 HRS in WGMR Experiment

A schematic of the experimental setup is shown in Fig. 7.3. Efficient coupling of laser radiation into and out of the WGMR is possible by means of frustrated-TIR at the surface of a coupling prism (Sec. 4.1). In our experiments, the horizontally polarized output of a Novawave 1064 nm fiber laser (courtesy of Dr. S. A. Aubin) was focussed on the internal surface of an equilateral diamond prism (1.5 mm sides) at the critical angle for total internal reflection (TIR) between the prism and the

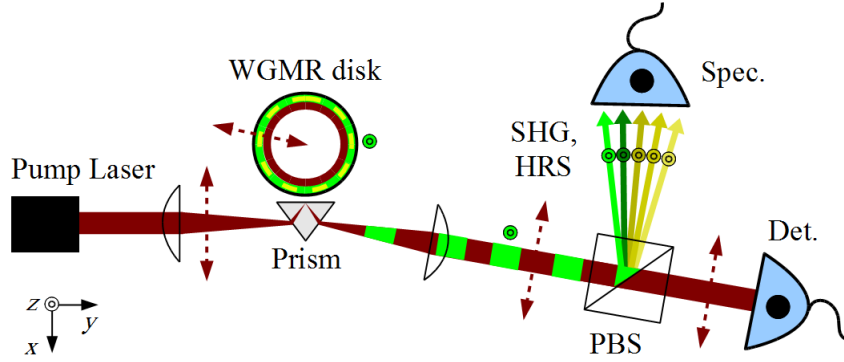


FIG. 7.3: HRS experiment schematic showing input and generated fields (see text for abbreviations, arrows show polarizations).

disk. The coupling efficiency was adjusted by changing the separation between the prism and the disk using precision micrometer. In this experiments we used two WGMR disks: a 1 mm-thick stoichiometric lithium niobate wafer (LiNbO_3 , $\text{Li/Nb} \sim 1$) and a magnesium oxide-doped lithium niobate wafer ($\text{MgO}:\text{LiNbO}_3$, $\text{MgO} \sim 3.5\%$). The diameters of both disks were approximately 7 mm. Each disk was z-cut, with the extraordinary axis of the crystal perpendicular to the radius of the disk. The subsequent procedure applies to both disks. The sides of the disks were hand-polished in our laboratory following the procedure developed in Sec. 4.3, to a rounded cross-section with approximately 0.2 mm radius of curvature at the disk's equator. The laser used for the described experiments did not allow a controlled frequency sweep, so that the pump frequency had to be manually adjusted every time to the frequency of some WGMR eigenmode to achieve maximum coupling. The lack of continuous frequency tuning capability significantly complicated the process of finding the optimal coupling and made the measurements of Q-factor at 1064 nm wavelength virtually impossible. However, we estimate that the Q-factor of the disk exceeds 10^7 from data obtained using a similar disk and a tunable 800 nm laser.

The radiation inside the disk exited through the same coupling prism and was recollimated by the second lens. All optical fields generated through nonlinear frequency conversion inside the disk were polarized in z direction (as indicated in Fig.) and orthogonal to x -polarized pump laser. A polarizing beam splitter (PBS) placed after the output collimating lens split these fields from the transmitted pump laser and sent them to a broadband spectrometer [Ocean Optics HR4000, resolution 0.4nm (Spec.)]. The transmission of the pump beam, measured by a photodiode (Det.) placed at the second output of the polarizing beam splitter, was used to control coupling efficiency.

To study nonlinear frequency conversion inside the disk, we gradually increased the power of the pump laser until we observed generation of light at different wavelengths. Even though we have operated at room temperature (i.e., far from non-critical phase matching temperature) we observed second harmonic generation (SHG) at 532 nm inside our whispering-gallery mode disk, with a pump power of $P_\omega = 11$ mW, as shown in Fig. 7.4(a). This result was somewhat surprising, as the experimentally determined phase matching temperature for our stoichiometric lithium niobate was $T_{PM} = 140$ °C (MgO:LiNbO₃ $T_{PM} = 99$ °C). The efficiency of the second harmonic conversion was significantly reduced due to the phase mismatch - at a pump power of $P_\omega = 300$ mW the output second harmonic power was $P_{2\omega} \sim 3$ μ W). With increased pump power, we unexpectedly observed Raman-type generation of several additional fields, yellow-shifted with respect to the green 532 nm SH field. In the stoichiometric lithium niobate disk (*Middle*, Fig. 7.4) these four unexpected fields appeared at roughly the same threshold power $P_\omega \simeq 430$ mW at approximately equidistant frequencies 545 nm, 559 nm, 573 nm, and 587 nm. A similar spectrum was observed in MgO:LiNbO₃ at somewhat higher pump power, due to less efficient coupling (*Bottom*, Fig. 7.4). The frequency position of the shifted modes, the scattering geometry inside the WGMR, and the relative intensity of the generated fields suggest

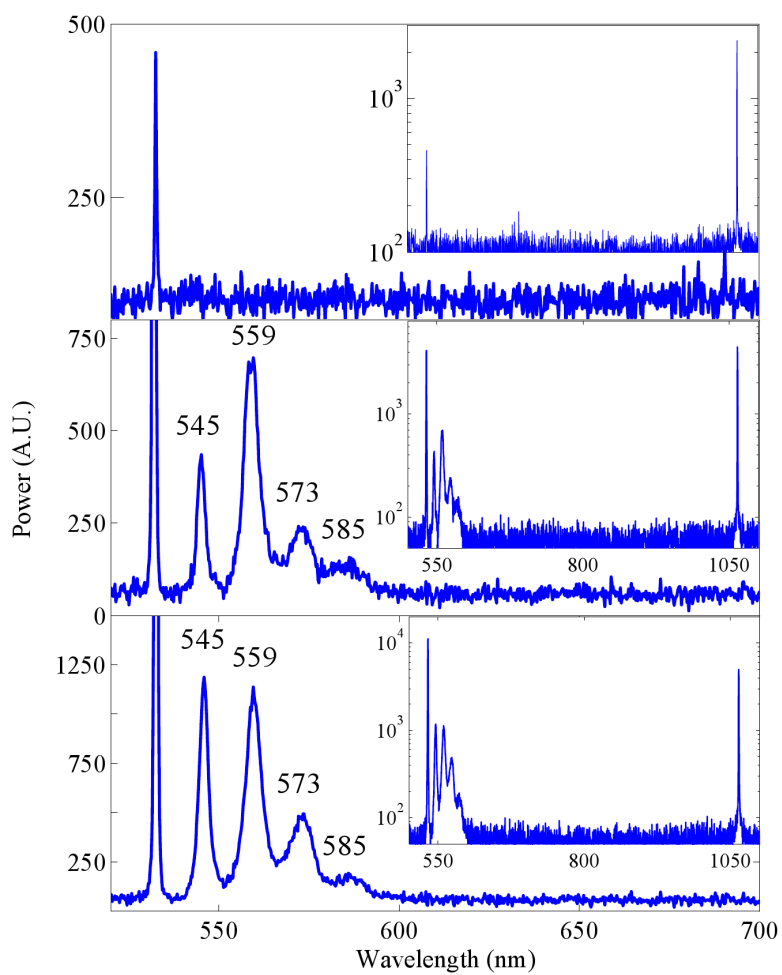


FIG. 7.4: Output spectra of HRS emission from whispering-gallery mode resonators. *Top*: SHG emission from stoichiometric LiNbO_3 disk with 11 mW pump power; *Middle*: emission from same disk at 650 mW pump power and coupling efficiency 70 %, *Bottom*: emission from $\text{MgO}:\text{LiNbO}_3$ disk at 825 mW pump power and coupling efficiency 30 %.

that they are generated through a hyper-Raman process, in which the hyper-Raman scattering is accompanied by excitation of one or multiple phonons in configuration shown in Figure 7.2.

The observed frequency difference between two consecutive generated fields of ≈ 14 nm corresponds to a Raman shift of $\omega_R = 455 \text{ cm}^{-1}$, associated with either the E(LO)7 or an A_2 phonon mode in LiNbO_3 [93, 95, 96]. However, the generation of the yellow-shifted fields via direct Raman scattering of the second harmonic field of same polarization is prohibited by the selection rules, since the α_{zz} element of the E-mode polarizability tensor is zero. Similarly, we can rule out the A_2 mode as both its α_{zz} and β_{zxx} elements are zero. Rather, hyper-Raman scattering of the pump field is possible, since β_{zxx} is nonzero for the E-modes.

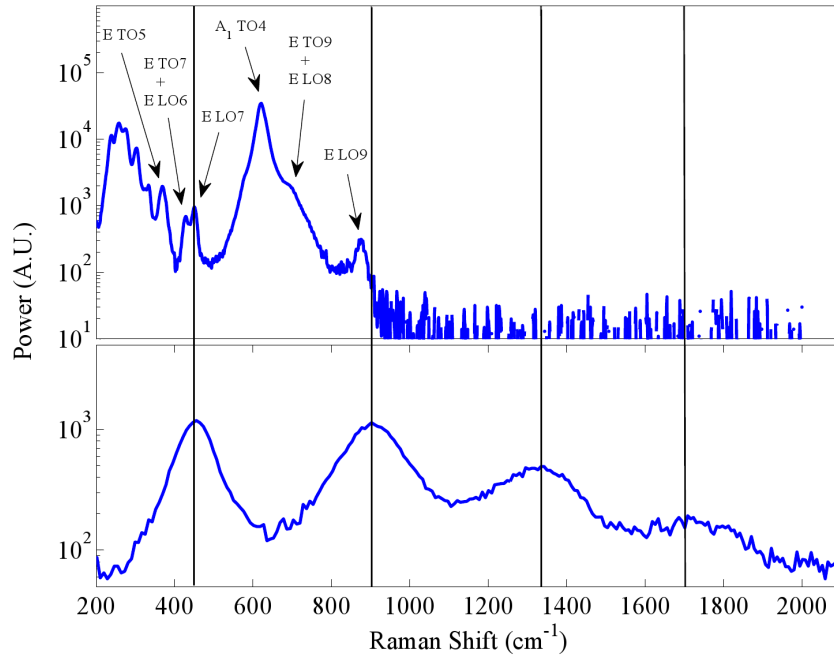


FIG. 7.5: Wavelength shift for (*Top*) Raman scattering of 785 nm from a lithium niobate crystal, and (*Bottom*) emission from lithium niobate WGMR with a 1064 nm pump, referenced to 532 nm. Lines are at 455 cm^{-1} , 909 cm^{-1} , 1337 cm^{-1} and 1686 cm^{-1} . Some optical modes are labeled in *Top* figure [93, 95, 96].

Still, hyper-Raman scattering involving single phonon cannot explain observation of lower-frequency yellow fields. Such process would involve excitation of phonons with Raman shifts of 909 cm^{-1} , 1337 cm^{-1} , and 1686 cm^{-1} , and such high-frequency phonons are not supported by the lithium niobate crystal lattice. This was verified by obtaining a traditional Raman scattering spectra for our samples using a 785 nm DeltaNu Raman Spectrometer. Comparison of this Raman spectra with recorded WGMR emission is shown in Fig. 7.5. We can also rule out cascaded Raman scattering as all the generated fields are polarized in the same z direction, and the polarizability tensor element for that process is zero as described above. These extra fields are more consistent with multi-phonon overtones $2\omega_0 - 2\omega_R$, $2\omega_0 - 3\omega_R$, $2\omega_0 - 4\omega_R$ (Fig. 7.4). Thus we think these results can be attributed to second-order hyper-Raman scattering.

In conclusion, we observed four Raman-shifted modes along with non-phase matched second harmonic generation inside our lithium niobate whispering-gallery mode disk resonators. The generated second harmonic field was neither powerful enough nor of the proper scattering geometry to produce observed Raman scattering at 455 cm^{-1} . Thus, we attribute Stokes fields produced at 545 nm, 559 nm, 573 nm, and 587 nm to the hyper-Raman scattering and second-order hyper-Raman scattering of the 1064 nm pump beam. This is interesting to study for both cavity hyper-Raman scattering itself, as well as its consequences for other nonlinear processes inside high-quality whispering-gallery mode resonators.

CHAPTER 8

VO₂ MIT and Q-switching

8.1 Q-switching

Optical cavities can be modulated to allow or prevent light building up in power. This can be done actively (in the case of Pockels cells) or passively (in the case of Kerr-lens mode-locking or a saturable absorber). This effectively modulates the cavity quality factor. This is called *Q-switching* [97].

Whispering-gallery mode resonators have been used to create micro laser cavities [32–37]. The small cavity length could allow for short pulses with very high repetition rates. As a crucial feature of these cavities is the high quality factor, adding a region of Q-switching material would allow for pulse generation.

A Q-switch material would have to have a significant change in optical properties, a change that occurs rapidly, and is repeatable [98]. Vanadium dioxide undergoes a phase transition between from an insulator to a metal which results in a significant change in reflectivity. This transition can be induced optically, in which case it occurs on the order of picoseconds [99]. The transition is reversible and repeatable. Vana-

dium dioxide has been studied as a low-loss plasmonic material [100–103], and has been deposited on different substrates as a thin-film. The properties of the transition are altered by the properties of the thin-film (thickness, substrate, etc.).

8.2 VO₂ metal-insulator phase transition

The ability of vanadium dioxide (VO₂) to undergo a photo-induced phase transition from an insulator to a metal (referred to as a metal-insulator transition, or MIT) by a sufficiently powerful ultrafast laser pulse within a sub-picosecond timescale [104–111] makes this material a promising candidate for ultrafast optical switches [103, 112–115], and controllable electronic and plasmonic devices [101, 116]. While the exact physical process of the transition remains open to discussion, it is evident that both a critical density of photoelectrons and the excitation of relevant phonons in VO₂ play a role in the fast photo-induced MIT transition [106, 110]. The reverse process of relaxing back to the insulating state is thermal, and therefore significantly slower [117]. This long relaxation time, on the order of nanoseconds \sim microseconds, poses a challenge in designing ultrafast switching technologies.

The metal-insulator transition (MIT) in vanadium dioxide occurs around 340 K in bulk [118–120]. Below this temperature VO₂ is an insulator with a monoclinic crystal structure, while above this temperature it is a metal with a rutile structure [118, 121]. The phase transition properties of VO₂ thin films depend on the film thickness and substrate material [122]. Generally thinner films have lower transition temperatures. VO₂ films grown on different substrates have different transition temperatures, and the cause of this relationship is currently being studied.

Our studies of the optically-induced MIT in VO₂ thin-films were done in collaboration with Dr. R. A. Lukaszew at the College of William & Mary, who provided

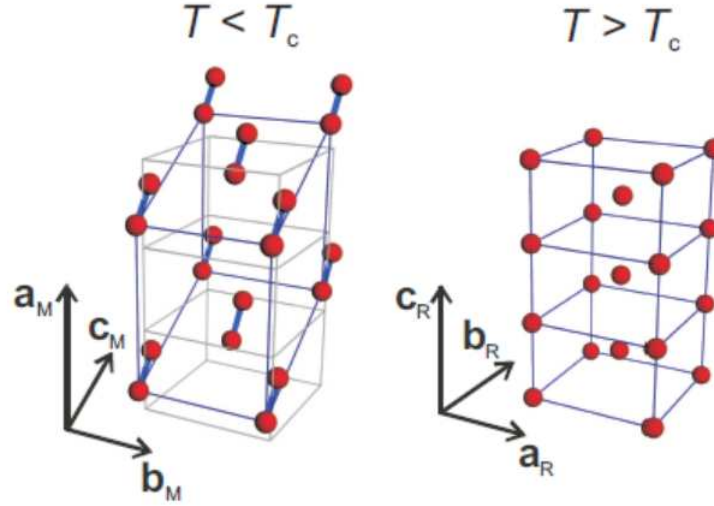


FIG. 8.1: VO₂ has an insulating monoclinic structure at low temperatures, and a metallic rutile structure at high temperatures.

the ultrafast system, cryostat system, and funding, and Dr. S. Wolf's group at the University of Virginia, who provided the VO₂ samples. We studied two VO₂ thin-film samples (shown in Figure 8.3), both grown using Biased Ion Target Beam Deposition (BITBD) [123]. One sample was 112 nm of VO₂ grown on top of a 0.5 mm TiO₂ (rutile) substrate. The TiO₂ substrate was cut along the (011) face. The other sample was 80 nm thick grown on a 0.5 mm c-Al₂O₃ (sapphire) substrate. XRD evaluation of both films showed them to be crystalline [124, 125]. The VO₂ transition temperatures were 308 K and 340 K for the rutile and sapphire samples, respectively.

To study the transition dynamics, we used an ultrafast pulsed laser to induce the transition, starting from temperatures below the transition temperature. After the transition to the metallic state, the VO₂ then relaxes back the insulating state. The ability to tailor this decay time is vital for a variety of applications. Extremely short decay times (\sim sub-ps) are useful for ultrafast optical switch applications, while longer decay times (\sim μ s) may be necessary for temporary electronic circuits. A

VO₂-based Q-switch repetition rate would be limited by this decay time.

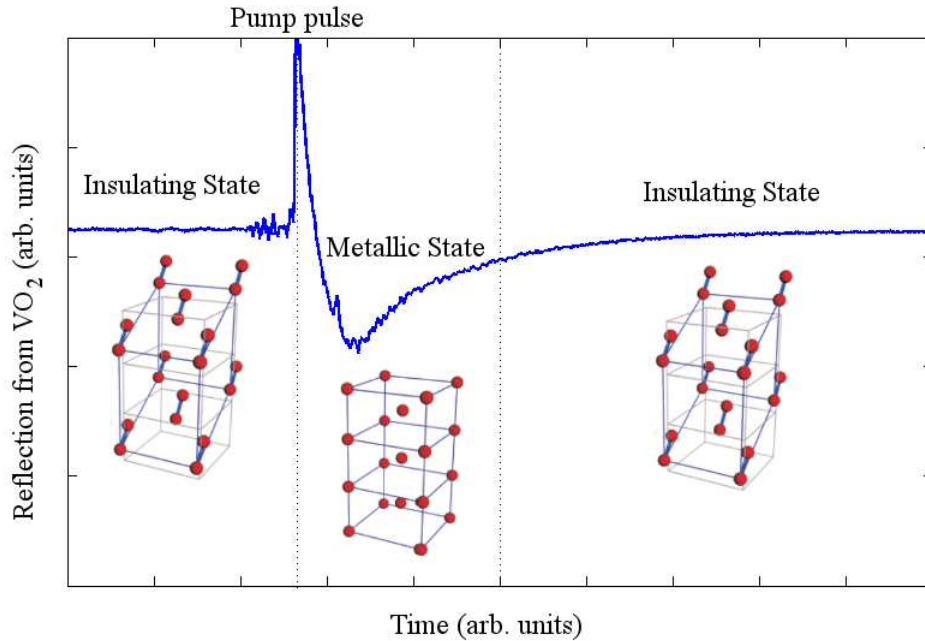


FIG. 8.2: An ultrafast pulse can cause a phase transition in VO₂ where the VO₂ goes from an insulator to a metal. This can be observed by a change in the optical reflectivity. The structure of VO₂ changes.

We report on the experimental measurement of the decay time from the metallic state for a VO₂ film deposited on TiO₂. We find that the decay time is an order of magnitude longer than for VO₂ grown on Al₂O₃, and increases as the pump fluence used to induce the transition is increased. Decay times for VO₂ on TiO₂ range from 40 ns to 1.1 μ s, while VO₂ on Al₂O₃ ranges from 1 ~ 5 ns.

8.2.1 Time-resolved pump-probe reflection measurements

We mounted our samples in a windowed cryostat with a temperature-controlled heater and a column for cooling with liquid nitrogen. We used an ultrafast laser in a pump-probe configuration with a variable time-delay between pump and probe pulses

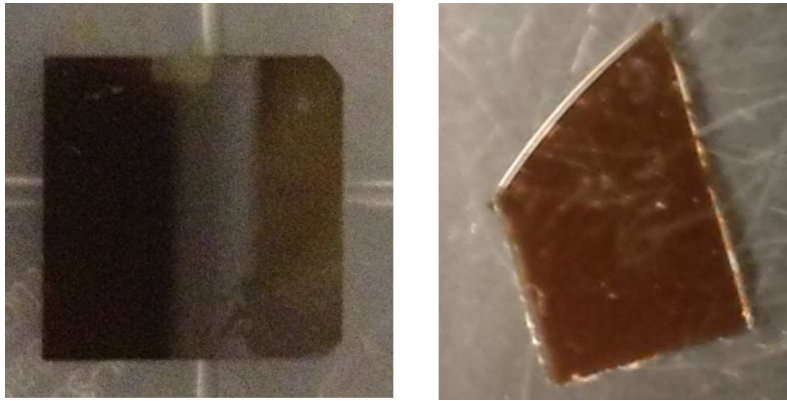


FIG. 8.3: Photos of VO_2 on rutile and sapphire substrates. *Left*: sample of VO_2 on TiO_2 used in the CW measurements. *Right*: sample of VO_2 on Al_2O_3 used in ultrafast measurements.

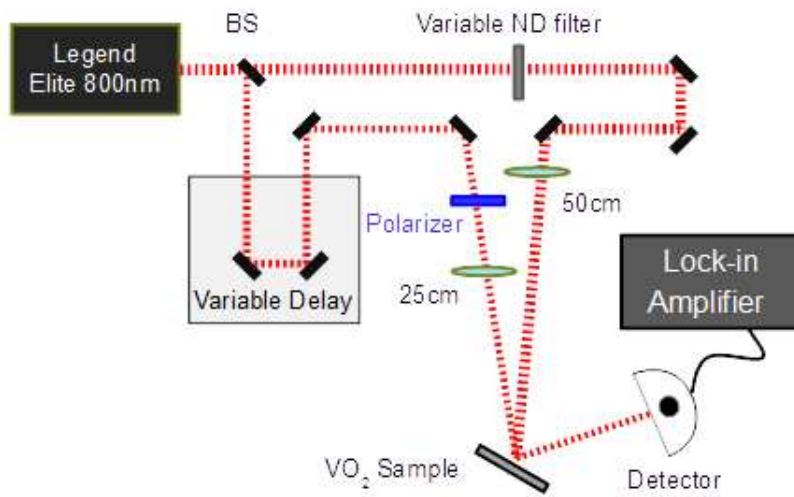


FIG. 8.4: VO_2 pump-probe with ultrafast probe experimental diagram.

to measure the optical reflectivity of our samples over time. The ultrafast 100 fs pulses were from a Coherent Legend regenerative amplifier operating at 1 kHz (Details about the system operation are in Appendix A). The pulses were sent through a beam splitter to create the pump and probe pulses. The pump pulses passed through a variable neutral-density filter (VF) to control the intensity, and were focussed to a 180 μm diameter on the VO_2 sample (Fig. 8.4).

The probe beam was directed along a variable delay stage to control the distance traveled by the probe pulse, and consequently the relative time between the pump and probe pulses. The probe pulses could be delayed relative to the pump pulses by a maximum of 4 ns. Probe power was reduced such that it could not induce the metal-insulator transition. The probe was focussed to an 80 μm on the sample to ensure it probed a uniform pump intensity. The probe reflection from the VO_2 was detected and was sent through a lock-in amplifier. To minimize the effects of probe pulse instabilities and long-term drifts due to environmental changes, our measurements are reported as changes in the probe reflection relative to the probe reflection when the pump beam was completely blocked ($\Delta R/R$). This allowed for sub-picosecond resolution of the change in reflectivity.

A typical measurement of MIT is shown in Fig. 8.5, as the probe beam delay is changed. Negative times correspond to the probe pulse arriving to the sample before the pump, thus interacting with VO_2 in its insulating stage. The fast drop in reflectivity indicates the transition of the sample to its metallic stage by the pump pulse. The time of this transition was comparable with the pulse duration, on the order of 150 fs, similar to previous experiments [105–110]. The evolution of the reflection signal from $t = 0$ to $t < 1$ ns reflected the non-equilibrium evolution of the VO_2 film [126]. However, here we focus on the slow thermal relaxation of the sample to its steady state, typically on a timescale of $t > 1$ ns. This slow increase of

reflectivity generally followed an exponential dependence:

$$\frac{\Delta R}{R}(t) = \frac{\Delta R}{R}(0) e^{-t/\tau} \quad (8.1)$$

where t is the time elapsed after MIT (i.e. the delay between probe and pump pulses), and τ is the thermal relaxation time constant.

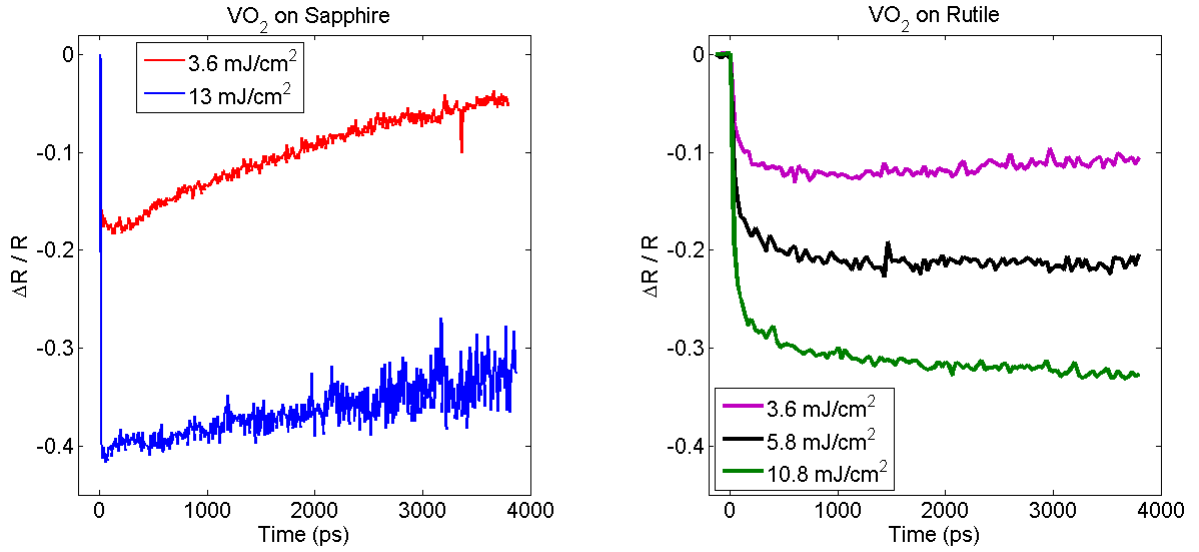


FIG. 8.5: Pump-probe measurements of VO₂ on sapphire (*Left*) and rutile (*Right*) substrates.

Fig. 8.5 demonstrates MIT measurements for both sapphire and rutile samples, measured for the full length of the delay stage track (4 ns) at room temperature. The slow relaxation back to the for the sapphire sample is well fit by Eq.(8.1), with a time constants of $\tau = 1.8$ ns and $\tau = 6.2$ ns. Over the same timescale the reflection of the rutile sample stays constant, indicating that the relaxation process takes significantly longer.

8.2.2 CW probe reflection measurements

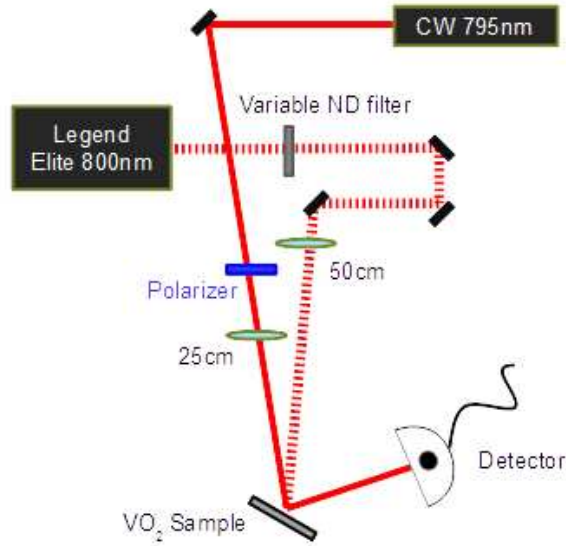


FIG. 8.6: VO₂ pump - CW probe experimental diagram - CW Probe

To measure the relaxation of the VO₂ on rutile, we modified our apparatus to use continuous-wave (CW) laser and fast photodetector (response time of 10 ns) instead of the ultrafast probe pulses (experimental set-up in Fig. 8.6). We used the same pump as in the previous section. This allowed us to probe the reflectivity at times greater than ~ 20 ns after MIT. A 2 mW CW 795 nm laser was used to probe the optical reflectivity of the sample. We set the detector to measure the reflected probe, however some scattered pump light could not be completely filtered out. Though this contamination was only present in within the first ~ 10 ns (and with thus little effect on our long-timescale measurements), we took baseline measurements without the probe laser on and subtracted the these from our measurements.

Example measurements of the MIT in VO₂ on rutile for two different pump pulse powers are shown in Fig. 8.7. After the initial drop from the transition to the

metal state, the reflectivity clearly takes longer than a few ns to return to the level of the insulating state. This is significantly longer than the VO₂ on sapphire sample (Fig. 8.5). Because this is longer than the response rate of the detector, we confirm that we can use CW probe measurements for the rutile sample.

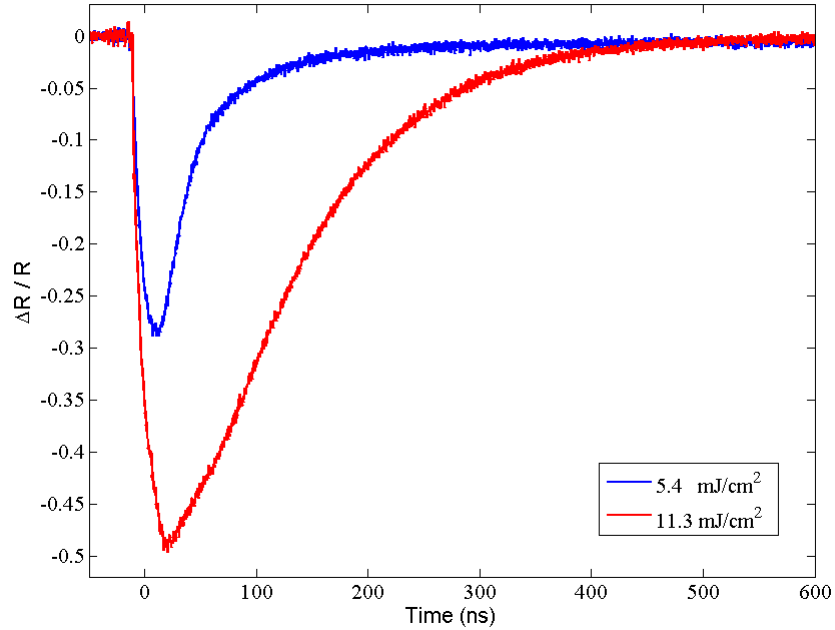


FIG. 8.7: CW pump-probe measurements of VO₂ on rutile sample.

8.2.3 Metallic state decay analysis

Fig. 8.7 also reveals that the rate of thermal relaxation for both samples decreases with higher pump power. This is an intuitively expected trend – since there is non-negligible absorption in the VO₂ thin film, more energy must be dissipated in case of more powerful pump pulse. Moreover, for the higher pump powers we observed deviation of the measured reflectivity from Eq.(8.1) for short times. We speculate that the observed “flattening” of the curves was due to the pump pulse heating the

sample above the threshold value for the thermally-induced MIT. In this case the reflectivity does not change significantly as the sample stays metallic while it cools to the transition temperature (where the reflectivity then changes significantly) . For all experimental curves only the later exponential part of the measured reflectivity was included into the fitting thermal relaxation time analysis.

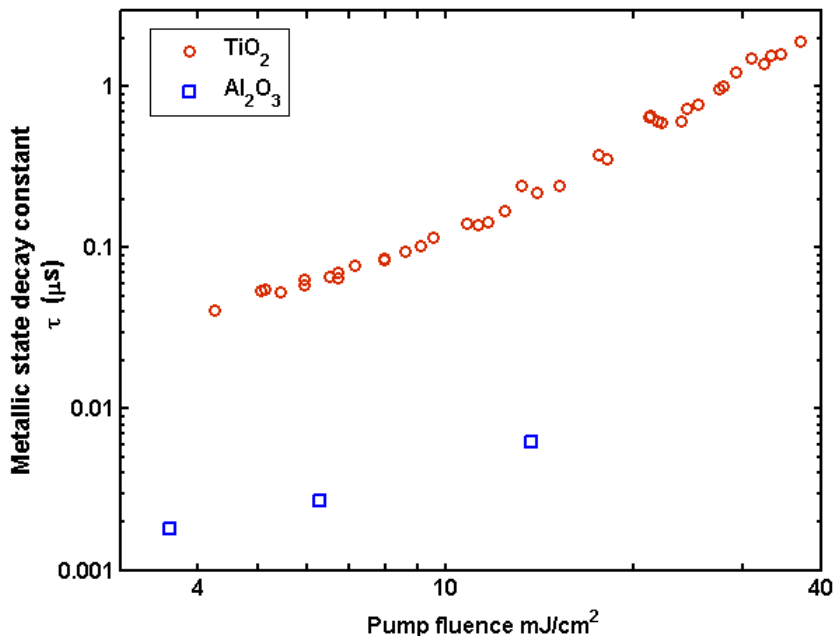


FIG. 8.8: Metallic state relaxation time constant τ vs. pump fluence found from a fit of the change in reflectivity to Eq. 8.1. Rutile data was obtained with a CW probe; Sapphire data using an ultrafast probe.

The dependence of the measured relaxation time constant τ on pump fluence is shown in Fig. 8.8. The available range of pump fluence was limited by our ability to reliably detect a change in reflectivity at low fluences, and by the VO₂ damage threshold (pump fluence > 40 mJ/cm²).

To investigate the temperature dependence on the relaxation time, we also repeated the measurements for VO₂ on rutile while changing the substrate temperature.

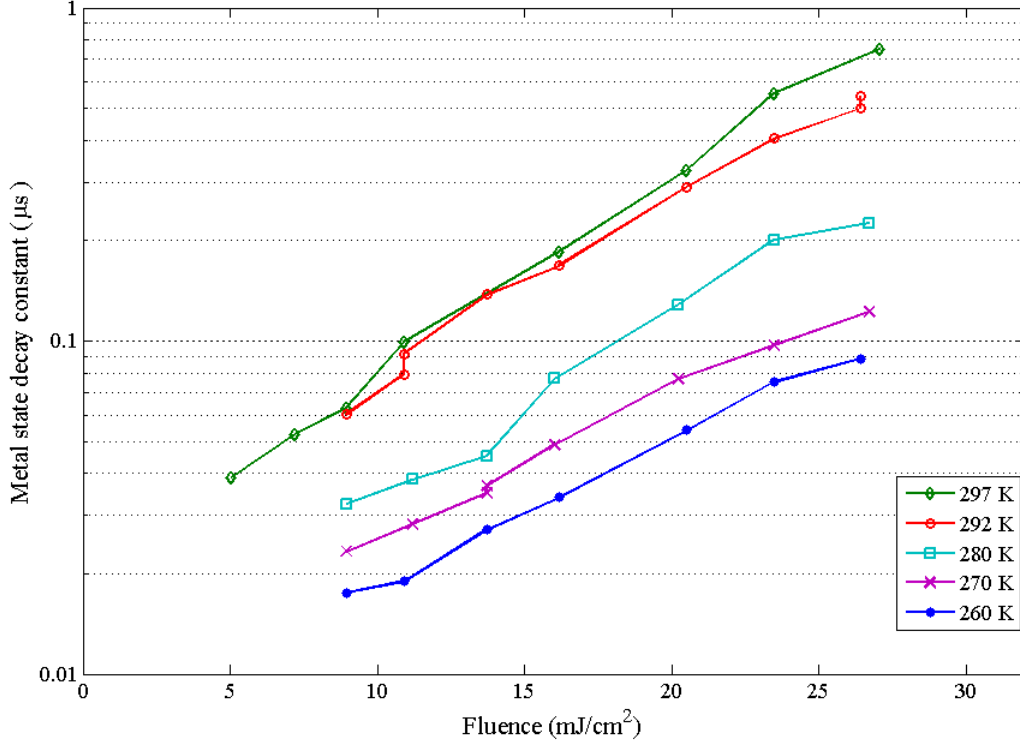


FIG. 8.9: Various substrate temperatures for the metallic state relaxation constant τ vs. pump fluence. Substrate temperature has a significant effect, though the relaxation times remain an order of magnitude above the sapphire relaxation times.

For these measurements the cryostat was pumped to a pressure of 10^{-4} Torr in with a dual stage sorption pump, and the substrate cooled to five different temperatures between 260 K and 297 K. Since the VO_2 relaxation can only be due to thermal exchange with the substrate, we expect that lowering the substrate temperature should decrease the relaxation time. The measurements in Fig. 8.9 confirm this prediction. Lowering the temperature by 30 K sped up the relaxation process by roughly a factor of five.

The most dramatic finding is the difference in relaxation times between the two samples. As thermal dissipation is the only mechanism available for the relaxation, there must be a difference between thermal transfer properties in the two samples.

The thermal conductivity of rutile is a factor of three less than sapphire (~ 9 vs. $27 \text{ Wm}^{-1}\text{K}^{-1}$), however we found more than an order of magnitude difference in the relaxation time. We suspect there is a large difference in the interfacial heat transport between the VO_2 and the substrate. This is influenced by the different mismatch of the crystal lattices of the VO_2 and substrate at the interface, causing strain on the VO_2 film. The effect of substrate strain on the other MIT properties is under ongoing investigation [125, 127–129]. Strain also affects the size and shape of the metallic domains that form, which may also affect the relaxation rate. As such, the precise cause of the extended relaxation in VO_2 on rutile is the subject of continuing research. This must be understood in order to tailor the properties of VO_2 thin films for any ultrafast optical switching applications.

Lastly, further investigation is needed to understand the role of substrate structure in relaxation time of an optically-induced MIT in VO_2 . The ability to tailor the relaxation time is important for applications such as ultrafast optical switching or temporary circuits, where this time will determine the limit to the switch repetition rate or the persistence time of the circuit. While depositing VO_2 on a rutile substrate reduces the transition temperature and threshold pump power, it also increases the relaxation time. Understanding the mechanism behind this effect may lead to a way to mitigate or alter the delay time.

CHAPTER 9

Conclusions and Outlook

Whispering-gallery mode resonators have unique properties that bring advantages to many different fields. We explored using them for nonlinear optical processes and quantum optics. In particular, we examined second harmonic generation inside a WGMR as a method for generating low-power squeezed light. Though it has lately been less studied for squeezed light than other methods, squeezing via SHG has several advantages. Optical parametric oscillation (OPO) [19–22, 25, 44] has generated the most squeezing [23, 24], however OPO squeezing typically requires more steps than SHG, and produces squeezed vacuum states. Squeezing through second harmonic generation requires a single conversion step, reducing the equipment and complexity, and produces bright, intensity squeezed light, rather than vacuum. Four-wave mixing (FWM) is another process used to produce squeezed light [26–28]. The best squeezing through four-wave mixing has been achieved in atomic vapors, and require frequencies tuned to atomic transitions. This reduces the possible wavelengths. Second harmonic generation is achievable for a large range of wavelengths. However SHG has generally required high pump power to achieve modest conversion efficiency.

We explored using a high-quality factor WGMR cavity to produce bright, intensity squeezed light through SHG with low pump power.

9.1 Summary of results and limitations

We analyzed the quantum fluctuations in the output of a WGMR cavity under conditions of SHG using an input-output model (Sec. 3.4). Squeezing in transmitted pump intensity noise depends on the detection (noise) frequency, quality factor of the WGMR, input pump power, and saturation power (a measure of the SHG conversion). Squeezing is a maximum for low detection frequencies (Figure 3.6), which poses a problem for detection, as technical $1/f$ noise increases at low frequencies. The quality factor (Q) of the WGMR has a more dramatic effect. We found that squeezing in the intensity noise of the transmitted pump increases by ~ 6 dB with an order of magnitude increase in the quality factor of the cavity (Figure 3.10). With experimental conditions that are possible (detection frequency = 100 kHz, saturation power $W_0 = 3$ mW [43], and input pump power $P_{in} = 0.2$ mW [43]), predicted squeezing ranges from ~ 3 dB at $Q = 10^7$ to > 9 dB at $Q = 10^8$.

In order to demonstrate this experimentally, we developed procedures to produce high-quality factor, crystalline WGMR disks from nonlinear optical materials (Sec. 4.3). We worked with lithium niobate (LiNbO_3) and magnesium oxide-doped lithium niobate ($\text{MgO}:\text{LiNbO}_3$), and we were able to polish these disks to achieve an absorption-limited quality factor of $Q > 10^8$. We built a mount for our disks to couple a tunable-frequency laser into the whispering-gallery modes through prism coupling (Sec. 4.1). We found that the phase-matching temperature of the 1064 nm-to-532 nm SHG was reduced inside the whispering-gallery modes - to 89°C from 110°C for $\text{MgO}:\text{LiNbO}_3$. We were able to measure a maximum of 1 % conversion,

with an input pump power of ~ 1 mW. This was less than we expected (from previous work [43, 45]), which corresponded to higher saturation powers (~ 4 W versus ~ 3 mW). We attributed this to imperfect spatial mode-matching, due to the lack of control over the pump-to-second harmonic (pump-SH) mode overlap and phase-matching. The free spectral range of the WGMR contains many modes due to the curvature of the disk. The frequency separation between modes is different for the pump and second harmonic. Thus control of the relative frequency between pump and second harmonic modes is required. We implemented an electro-optic effect-based control using a DC electric field applied across the extraordinary axis of the disk. However, we were still unable to improve our saturation power. Due to the multitude of modes, there are many pairs of pump-SH modes, whose spatial overlap varies. Because the second harmonic modes exist closer to the rim than the pump modes, the k -vector mismatch varies, and the phase-matching temperature varies (sometimes significantly). To search for efficient SHG through all the mode pairs requires finding the phase-matching temperature and SH mode frequency for such a mode pair simultaneously (since the SH mode is not observable unless both these conditions are met). This makes it experimentally difficult to search for optimal conditions for SHG with no *a priori* knowledge of these values.

To determine if we could observe bright squeezed light, we measured the intensity noise of the transmitted pump field from our WGMR disk (Chapter 6) during second harmonic generation. We found experimentally that while the coupling to the WGMR did not increase the intensity noise, moderately efficient second harmonic generation increased the intensity noise of the pump. We attributed this to unstable second harmonic mode overlap, causing FM-to-AM conversion noise (Sec. 6.5.1). We did observe indications that more efficient SHG coincided with a drop in the excess noise, though not below shot noise (Figures 6.7, 6.9).

Additionally, our noise detection was limited to frequencies above ~ 3 MHz due to excess laser noise. An intensity noise eater supplied by the manufacturer reduced the intensity noise at low frequencies, but did not reduce it to shot noise. We were also limited by the quantum efficiency of our photodetectors, which was around 85 % for our pump photodiodes, and 80 % for our SH photodiodes, as well as the low-frequency amplifier noise from the operational amplifiers. Due to the combination of low SHG power and low quantum efficiency, we were unable to obtain any significant noise measurements of the transmitted second harmonic.

We were also technically limited by a couple other factors. Our coupling to the WGMR disk was limited to < 50 % of the incident pump. 100 % coupling is known as impedance-matching or critical coupling, and requires that the incident beam spatially match the cavity's internal mode at the point of coupling. Whereas at the interface of a two-mirror cavity the mode resembles a gaussian beam, the whispering-gallery modes for a disk are approximate solutions to spherical Bessel functions and spherical harmonics (Sec. 2.3.2), and the coupling at the interface relies on evanescent wave coupling, making mode-matching more difficult [70]. It is possible to achieve close to ~ 80 % [86].

When we accounted for the low SHG efficiency and high detection frequency in our theoretical calculations, our predicted possible squeezing was reduced from ~ 9 dB for the ideal case to less than 1 dB for our actual parameters. With the quantum efficiency of our photodiodes, a reduction of less than a dB is very difficult to observe.

9.2 Outlook and potential improvements

In order to address our non-optimal phase/mode-matching, the WGMR disks could be engineered to reduce the number of whispering-gallery modes. This would reduce the set of mode pairs, reducing the searchable parameter space. Single-mode WGMRs have been fabricated by creating a small protrusion on the rim of a WGMR disk through diamond-point turning techniques [130]. The reduced size of this region creates single-mode conditions. Alternately, WGMRs have been engineered with a continuum spectrum [131]. Instead of removing extraneous modes, this would ensure a mode is always available, easing the constraint on one parameter. Both of these methods require more careful control over the shape of the WGMR resonator during fabrication.

We were also limited by our mode-matching of the pump to the internal WG modes. Matching the input beam shape to the spatial mode of the cavity would increase the coupling efficiency. This has been accomplished using a GRIN lens [43], and also by coupling with a tapered fiber [130, 132].

In Sec. 3.5.2 squeezing increases at lower detection frequencies. However, laser noise prevented us from detecting squeezing below ~ 2 MHz. This could be resolved by using a laser that does not exhibit a relaxation oscillation (Sec. 6.3), which may or may not be realistic for 1064 nm. An alternative solution is to use a more effective noise eater to eliminate the noise from the oscillation.

In principle, the modal overlaps and phase-matching temperatures could be calculated to find the optimal modes and temperatures, following the work of [43]. This would be approximate, as the precise geometry of the disks are not known. An attempt to more carefully measure the curvature of the disk would make the results of the calculations more accurate. As it is possible the optimal tempera-

ture/overlap combination is significantly far from our current operating temperature (89°C, Sec. 5.2), even an approximate prediction would be useful.

With improvements that have already been demonstrated, it is possible to design an experiment that would demonstrate significant intensity squeezing, with very-low input powers ($< \text{mW}$), through second harmonic generation in a whispering-gallery mode resonator.

APPENDIX A

Ultrafast laser system

The Coherent Legend system is designed to produce amplified ultrafast pulses of around 100 fs in pulse length, with more than 1 mJ of energy per pulse. A Ti:Sapphire oscillator (in our case a Coherent Mantis) is pumped by a 5 W, 532 nm CW laser (Millenia) and aligned to produce ~ 6 nJ, < 100 fs pulses at a repetition rate of 80 MHz. In order to produce pulses with a higher energy, a regenerative amplifier is used. This is the center of the Legend system. The schematic of the system is shown in Fig. A.1.

The regenerative amplifier (RGA) consists of an actively controlled cavity with a Ti:Sapphire crystal pumped by a 15 W, 532 nm Q-switched laser (Coherent Evolution). The cavity is controlled by three Pockels cells. These are synced to let a single seed pulse enter, pass through the Ti:Sapphire crystal a set number of times, and then exit. The pulse gets amplified in every pass through the crystal by energy from the 15 W pump. After a few passes, the pulse will then begin losing energy in subsequent passes, and the exit Pockels cell must be set to let the pulse exit before such time.

Amplification of ultrashort (< 1 ps) pulses in this manner would result in damage to the Ti:Sapphire crystal. To avoid this, the seed pump (from the Mantis oscillator) pulses are first stretched (chirped) in time. A grating is used to spread out the frequencies in the pulse (pulse frequency width is ~ 80 nm) in space, they are made to travel different distances, then recombined by the grating in space. This stretches the pulse in time, reducing the peak intensity to prevent damage in the crystal. Then once the pulses are amplified by the RGA cavity, they are put through the reverse process, and compressed back to a pulse length of 100 fs. Now the pulses have nearly 3 orders of magnitude more energy, 1 mJ compared to 6 nJ. Because the pulses must be allowed to travel multiple passes through the RGA cavity, the repetition rate of the amplified pulses is also reduced (our repetition rate is 1 kHz).

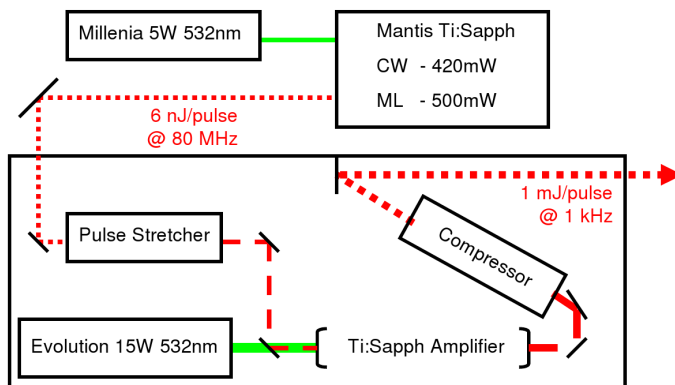


FIG. A.1: Coherent Legend system schematic showing the components and beam path.

Funding for this system was provided through the SRC and VMEC (Dr. R. A. Lukaszew, PI).

BIBLIOGRAPHY

- [1] S. L. Braunstein and P. van Loock, *Rev. Mod. Phys.* **77**, 513 (2005).
- [2] A. S. Coelho, F. A. S. Barbosa, K. N. Cassemiro, A. S. Villar, M. Martinelli, and P. Nussenzveig, *Science* **326**, 823 (2009).
- [3] W. P. Bowen, N. Treps, B. C. Buchler, R. Schnabel, T. C. Ralph, H.-A. Bachor, T. Symul, and P. K. Lam, *Phys. Rev. A* **67**, 032302 (2003).
- [4] A. Furusawa, J. L. Srensen, S. L. Braunstein, C. A. Fuchs, H. J. Kimble, and E. S. Polzik, *Science* **282**, 706 (1998).
- [5] N. Takei, H. Yonezawa, T. Aoki, and A. Furusawa, *Phys. Rev. Lett.* **94**, 220502 (2005).
- [6] T. Horrom, R. Singh, J. P. Dowling, and E. E. Mikhailov, *Phys. Rev. A* **86**, 023803 (2012).
- [7] K. Goda, O. Miyakawa, E. E. Mikhailov, S. Saraf, R. Adhikari, K. McKenzie, R. Ward, S. Vass, A. J. Weinstein, and N. Mavalvala, *Nature Physics* **4**, 472 (2008).
- [8] C. M. Caves, *Phys. Rev. D* **23**, 1693 (1981).
- [9] K. McKenzie, D. A. Shaddock, D. E. McClelland, B. C. Buchler, and P. K. Lam, *Phys. Rev. Lett.* **88**, 231102 (2002).

- [10] H. Vahlbruch, S. Chelkowski, B. Hage, A. Franzen, K. Danzmann, and R. Schnabel, *Phys. Rev. Lett.* **95**, 211102 (2005).
- [11] L. A. Lugiato, F. D. Martini, and G. Strini, *Opt. Lett.* **8**, 256 (1983).
- [12] R.-D. Li and P. Kumar, *Phys. Rev. A* **49**, 2157 (1994).
- [13] H. Tsuchida, *Opt. Lett.* **20**, 2240 (1995).
- [14] T. Suhara, M. Fujimura, K. Kintaka, H. Nishihara, P. Kurz, and T. Mukai, *Quantum Electronics, IEEE Journal of* **32**, 690 (1996), ISSN 0018-9197.
- [15] Y. qing Li, D. Guzun, and M. Xiao, *Opt. Lett.* **24**, 987 (1999).
- [16] U. Andersen and P. Buchhave, *Opt. Express* **10**, 887 (2002).
- [17] M. J. Lawrence, R. L. Byer, M. M. Fejer, W. Bowen, P. K. Lam, and H.-A. Bachor, *J. Opt. Soc. Am. B* **19**, 1592 (2002).
- [18] S. Zhang, Y. Li, J. Liu, and K. Zhang, *Journal of Physics B: Atomic, Molecular and Optical Physics* **39**, 4163 (2006).
- [19] G. J. Milburn and D. F. Walls, *Phys. Rev. A* **27**, 392 (1983).
- [20] J. Laurat, L. Longchambon, C. Fabre, and T. Coudreau, *Opt. Lett.* **30**, 1177 (2005).
- [21] Y. Takeno, M. Yukawa, H. Yonezawa, and A. Furusawa, *Opt. Express* **15**, 4321 (2007).
- [22] M. Pysher, R. Bloomer, C. M. Kaleva, T. D. Roberts, P. Battle, and O. Pfister, *Opt. Lett.* **34**, 256 (2009).

- [23] H. Vahlbruch, M. Mehmet, S. Chelkowski, B. Hage, A. Franzen, N. Lastzka, S. Goßler, K. Danzmann, and R. Schnabel, *Phys. Rev. Lett.* **100**, 033602 (2008).
- [24] G. Masada, T. Suzudo, Y. Satoh, H. Ishizuki, T. Taira, and A. Furusawa, *Opt. Express* **18**, 13114 (2010).
- [25] M. Mehmet, H. Vahlbruch, N. Lastzka, K. Danzmann, and R. Schnabel, *Phys. Rev. A* **81**, 013814 (2010).
- [26] R. E. Slusher, B. Yurke, P. Grangier, A. LaPorta, D. F. Walls, and M. Reid, *J. Opt. Soc. Am. B* **4**, 1453 (1987).
- [27] D. K. Giri and P. S. Gupta, *Journal of Optics B: Quantum and Semiclassical Optics* **6**, 91 (2004).
- [28] C. F. McCormick, V. Boyer, E. Arimondo, and P. D. Lett, *Opt. Lett.* **32**, 178 (2007).
- [29] E. E. Mikhailov and I. Novikova, *Opt. Lett.* **33**, 1213 (2008).
- [30] T. Horrom, A. Lezama, S. Balik, M. D. Havey, and E. E. Mikhailov, *Journal of Modern Optics* **58**, 1936 (2011).
- [31] T. Horrom, I. Novikova, and E. E. Mikhailov, *Journal of Physics B: Atomic, Molecular and Optical Physics* **45**, 124015 (2012).
- [32] V. Sandoghdar, F. Treussart, J. Hare, V. Lefèvre-Seguin, J. M. Raimond, and S. Haroche, *Phys. Rev. A* **54**, R1777 (1996).
- [33] S. M. Spillane, T. J. Kippenberg, and K. J. Vahala, *Nature* **415**, 621 (2002).
- [34] K. Sasagawa, K. Kusawake, J. Ohta, and M. Nunoshita, *Electronics Letters* **38**, 1355 (2002), ISSN 0013-5194.

- [35] B. Min, T. J. Kippenberg, and K. J. Vahala, *Opt. Lett.* **28**, 1507 (2003).
- [36] M. Cai, O. Painter, K. J. Vahala, and P. C. Sercel, *Opt. Lett.* **25**, 1430 (2000).
- [37] B. Min, T. J. Kippenberg, L. Yang, K. J. Vahala, J. Kalkman, and A. Polman, *Phys. Rev. A* **70**, 033803 (2004).
- [38] A. M. e. a. Armani, *Science* **317**, 783 (2007).
- [39] W. Lukosz, *Sensors and Actuators B: Chemical* **29**, 37 (1995), ISSN 0925-4005, proceedings of the 2nd European Conference on Optical Chemical Sensors and Biosensors.
- [40] R. W. Boyd and J. E. Heebner, *Appl. Opt.* **40**, 5742 (2001).
- [41] S. Blair and Y. Chen, *Appl. Opt.* **40**, 570 (2001).
- [42] W. Fang, D. B. Buchholz, R. C. Bailey, J. T. Hupp, R. P. H. Chang, and H. Cao, *Applied Physics Letters* **85**, 3666 (2004).
- [43] J. U. Fürst, D. V. Strekalov, D. Elser, M. Lassen, U. L. Andersen, C. Marquardt, and G. Leuchs, *Phys. Rev. Lett.* **104**, 153901 (2010).
- [44] J. U. Fürst, D. V. Strekalov, D. Elser, A. Aiello, U. L. Andersen, C. Marquardt, and G. Leuchs, *Phys. Rev. Lett.* **105**, 263904 (2010).
- [45] V. S. Ilchenko, A. A. Savchenkov, A. B. Matsko, and L. Maleki, *Phys. Rev. Lett.* **92**, 043903 (2004).
- [46] D. L. Mills, *Nonlinear Optics* (Springer, 1998).
- [47] J. D. Jackson, *CLASSICAL ELECTRODYNAMICS, 3RD ED* (Wiley India Pvt. Limited, 2007), ISBN 9788126510948.

- [48] R. W. Boyd, *Nonlinear Optics* (Academic Press, 2003).
- [49] E. G. Sauter, *Nonlinear Optics* (John Wiley & Sons, Inc., 1996).
- [50] P. Kryukov, V. Dmitriev, G. Gurzadyan, and D. Nikogosyan, *Handbook of Nonlinear Optical Crystals* (Springer, 1997).
- [51] D. Xue and S. Zhang, *Journal of Physics: Condensed Matter* **9**, 7515 (1997).
- [52] U. Schlarb and K. Betzler, *Phys. Rev. B* **50**, 751 (1994).
- [53] I. Shoji, T. Kondo, A. Kitamoto, M. Shirane, and R. Ito, *J. Opt. Soc. Am. B* **14**, 2268 (1997).
- [54] J. A. Giordmaine, *Phys. Rev. Lett.* **8**, 19 (1962).
- [55] G. D. Boyd and D. A. Kleinman, *Journal of Applied Physics* **39**, 3597 (1968).
- [56] O. Svelto, *Principles of lasers / by Orazio Svelto ; translated by David C. Hanna* (Plenum Press New York, 1976), ISBN 0306308600.
- [57] G. Rempe, R. Lalezari, R. J. Thompson, and H. J. Kimble, *Opt. Lett.* **17**, 363 (1992).
- [58] L. Rayleigh, *Philosophical Magazine Series 6* **20**, 1001 (1910).
- [59] L. Rayleigh, *Philosophical Magazine Series 6* **27**, 100 (1914).
- [60] J. R. Schwesyg, T. Beckmann, A. S. Zimmermann, K. Buse, and D. Haertle, *Opt. Express* **17**, 2573 (2009).
- [61] K. J. Vahala, *Nature* **424**, 839 (2003).

- [62] A. B. Matsko, ed., *Practical Applications of Microresonators in Optics and Photonics* (CRC Press, 2009).
- [63] A. N. Oraevsky, *Quantum Electronics* **32**, 377 (2002).
- [64] A. A. Savchenkov, V. S. Ilchenko, A. B. Matsko, and L. Maleki, *Phys. Rev. A* **70**, 051804 (2004).
- [65] M. L. Gorodetsky, A. A. Savchenkov, and V. S. Ilchenko, *Opt. Lett.* **21**, 453 (1996).
- [66] D. W. Vernooy, V. S. Ilchenko, H. Mabuchi, E. W. Streed, and H. J. Kimble, *Opt. Lett.* **23**, 247 (1998).
- [67] A. Matsko and V. Ilchenko, *Selected Topics in Quantum Electronics*, *IEEE Journal of* **12**, 3 (2006), ISSN 1077-260X.
- [68] C. C. Lam, P. T. Leung, and K. Young, *J. Opt. Soc. Am. B* **9**, 1585 (1992).
- [69] G. Kozyreff, J. L. Dominguez Juarez, and J. Martorell, *Phys. Rev. A* **77**, 043817 (2008).
- [70] M. Gorodetsky and V. Ilchenko, *Optics Communications* **113**, 133 (1994), ISSN 0030-4018.
- [71] P. L. Knight and L. Allen, *Concepts of Quantum Optics* (Pergamon Press, 1983).
- [72] M. O. Scully and M. S. Zubairy, *Quantum Optics* (Cambridge University Press, 1997).
- [73] H.-A. Bachor, *A Guide to Experiments in Quantum Optics* (WILEY-VCH, 1998).

- [74] R. J. Glauber, Phys. Rev. **131**, 2766 (1963).
- [75] D. F. Walls, Nature **306**, 141 (1983).
- [76] J. J. Sakurai and S. F. Tuan, *Modern quantum mechanics: solutions manual* (Benjamin-Cummings, Menlo Park, CA, 1985).
- [77] J. U. Fürst, D. V. Strekalov, D. Elser, A. Aiello, U. L. Andersen, C. Marquardt, and G. Leuchs, Phys. Rev. Lett. **106**, 113901 (2011).
- [78] M. J. Collett and C. W. Gardiner, Phys. Rev. A **30**, 1386 (1984).
- [79] P. Meystre and M. Sargent, *Elements of Quantum Optics*, SpringerLink: Springer e-Books (Springer, 2007), ISBN 9783540742111.
- [80] V. B. Braginsky, M. L. Gorodetsky, and V. S. Ilchenko, Phys. Lett. A **137**, 393 (1989).
- [81] D. K. Serkland, P. Kumar, M. A. Arbore, and M. M. Fejer, Opt. Lett. **22**, 1497 (1997).
- [82] F. A. GRANT, Rev. Mod. Phys. **31**, 646 (1959).
- [83] E. Hecht and A. Zajac, *Optics*, World student series (Addison-Wesley Pub. Co., 1974).
- [84] O. Paul, A. Quosig, T. Bauer, M. Nittmann, J. Bartschke, G. Anstett, and J. Lhuillier, Applied Physics B **86**, 111 (2007), ISSN 0946-2171.
- [85] M. Klein and T. Furtak, *Optics*, Wiley series in pure and applied optics (Wiley, 1986), ISBN 9780471872979.
- [86] M. L. Gorodetsky and V. S. Ilchenko, J. Opt. Soc. Am. B **16**, 147 (1999).

- [87] *Ada4817 low noise, 1 ghz fastfet opamps* (2008-2013).
- [88] R. Loudon, *Advances in Physics* **13**, 423 (1964).
- [89] D. Griffiths, *Introduction to electrodynamics* (Prentice Hall, 1999), ISBN 9780138053260.
- [90] V. Denisov, B. N. Mavrin, and V. B. Podobedov, *Physics Reports* **151** (1987).
- [91] S. J. Cyvin et al., *Journal of Chemical Physics* **43**, 4083 (1965).
- [92] R. F. Schaufele and M. Weber, *Physical Review* **152**, 705 (1966).
- [93] A. Ridah, P. Bourson, M. D. Fontana, and G. Malovichko, *J. Phys.: Condens. Matter* **9**, 9687 (1997).
- [94] V. N. Denisov et al., *Optics Communications* **26**, 372 (1978).
- [95] R. Claus, G. Borstel, E. Wiesendanger, and L. Steffan, *Physical Review B* **6**, 4878 (1972).
- [96] P. Hermet, M. Veithen, and P. Ghosez, *Journal of Physics: Condensed Matter* **19**, 456202 (2007).
- [97] S. Hooker and C. Webb, *Laser Physics*, Oxford Master Series in Condensed Matter Physics Series (OUP Oxford, 2010), ISBN 9780198506928.
- [98] H. W. Liu, L. M. Wong, S. J. Wang, S. H. Tang, and X. H. Zhang, *Journal of physics. Condensed matter : an Institute of Physics journal* **24**, 415604 (2012), ISSN 1361-648X.
- [99] T. Cocker, L. Titova, S. Fourmaux, G. Holloway, H.-C. Bandulet, D. Brassard, J.-C. Kieffer, M. El Khakani, and F. Hegmann, *Physical Review B* **85**, 155120 (2012), ISSN 1098-0121.

- [100] B. Felde, W. Niessner, and D. Schalch, *Thin solid films* **305**, 61 (1997).
- [101] M. Rini, A. Cavalleri, and R. Schoenlein, *Optics ...* **30**, 558 (2005).
- [102] R. Lopez, T. E. Haynes, L. a. Boatner, L. C. Feldman, and R. F. Haglund, *Optics letters* **27**, 1327 (2002), ISSN 0146-9592.
- [103] D. W. Ferrara, E. R. MacQuarrie, J. Nag, a. B. Kaye, and R. F. Haglund, *Applied Physics Letters* **98**, 241112 (2011), ISSN 00036951.
- [104] A. Cavalleri and D. V. D. Linde, *Applied Physics A* **579**, 577 (1999).
- [105] a. Cavalleri, C. Tóth, C. Siders, J. Squier, F. Ráksi, P. Forget, and J. Kieffer, *Physical Review Letters* **87**, 237401 (2001), ISSN 0031-9007.
- [106] a. Cavalleri, T. Dekorsy, H. Chong, J. Kieffer, and R. Schoenlein, *Physical Review B* **70**, 3 (2004), ISSN 1098-0121.
- [107] a. Cavalleri, M. Rini, H. Chong, S. Fourmaux, T. Glover, P. Heimann, J. Kieffer, and R. Schoenlein, *Physical Review Letters* **95**, 067405 (2005), ISSN 0031-9007.
- [108] H.-T. Kim, Y.-W. Lee, B.-J. Kim, B.-G. Chae, S. J. Yun, K.-Y. Kang, K.-J. Han, K.-J. Yee, and Y.-S. Lim, *Physical Review Letters* **97**, 4 (2006).
- [109] M. Nakajima, N. Takubo, Z. Hiroi, Y. Ueda, and T. Suemoto, *Journal of Luminescence* **129**, 1802 (2009), ISSN 00222313.
- [110] T. L. Cocker, L. V. Titova, S. Fourmaux, H. C. Bandulet, D. Brassard, J. C. Kieffer, M. a. El Khakani, and F. a. Hegmann, *Applied Physics Letters* **97**, 221905 (2010), ISSN 00036951.
- [111] S. Lysenko, a.J. Rua, V. Vikhnin, J. Jimenez, F. Fernandez, and H. Liu, *Applied Surface Science* **252**, 5512 (2006), ISSN 01694332.

- [112] T. Ben-Messaoud, G. Landry, J. Gariépy, B. Ramamoorthy, P. Ashrit, and a. Haché, *Optics Communications* **281**, 6024 (2008), ISSN 00304018.
- [113] S. B. Choi, J. S. Kyoung, H. S. Kim, H. R. Park, D. J. Park, B.-J. Kim, Y. H. Ahn, F. Rotermund, H.-T. Kim, K. J. Ahn, et al., *Applied Physics Letters* **98**, 071105 (2011), ISSN 00036951.
- [114] M. Rini, Z. Hao, R. W. Schoenlein, C. Giannetti, F. Parmigiani, S. Fourmaux, J. C. Kieffer, a. Fujimori, M. Onoda, S. Wall, et al., *Applied Physics Letters* **92**, 181904 (2008), ISSN 00036951.
- [115] F. Cilento, C. Giannetti, G. Ferrini, S. Dal Conte, T. Sala, G. Coslovich, M. Rini, A. Cavalleri, and F. Parmigiani, *Applied Physics Letters* **96**, 021102 (2010), ISSN 00036951.
- [116] T. Driscoll, S. Palit, M. M. Qazilbash, M. Brehm, F. Keilmann, B.-G. Chae, S.-J. Yun, H.-T. Kim, S. Y. Cho, N. M. Jokerst, et al., *Applied Physics Letters* **93**, 024101 (2008), ISSN 00036951.
- [117] H. Wen, L. Guo, E. Barnes, J. H. Lee, D. a. Walko, R. D. Schaller, J. a. Moyer, R. Misra, Y. Li, E. M. Dufresne, et al., *Physical Review B* **88**, 165424 (2013), ISSN 1098-0121.
- [118] F. J. Morin, *Phys. Rev. Lett.* **3**, 34 (1959).
- [119] J. B. Goodenough, *Journal of Solid State Chemistry* **3**, 490 (1971), ISSN 0022-4596.
- [120] N. Mott, *Metal-insulator transitions* (1998).
- [121] A. Zylbersztein and N. F. Mott, *Phys. Rev. B* **11**, 4383 (1975).

- [122] B. Lazarovits, K. Kim, K. Haule, and G. Kotliar, *Physical Review B* **81**, 115117 (2010), ISSN 1098-0121.
- [123] K. G. West, J. Lu, J. Yu, D. Kirkwood, W. Chen, Y. Pei, J. Claassen, and S. a. Wolf, *Journal of Vacuum Science & Technology A: Vacuum, Surfaces, and Films* **26**, 133 (2008), ISSN 07342101.
- [124] L. Wang, E. Radue, S. Kittiwatanakul, C. Clavero, J. Lu, S. a. Wolf, I. Novikova, and R. a. Lukaszew, *Optics letters* **37**, 4335 (2012), ISSN 1539-4794.
- [125] E. Radue, E. Crisman, L. Wang, S. Kittiwatanakul, J. Lu, S. A. Wolf, R. Wincheski, R. A. Lukaszew, and I. Novikova, *Journal of Applied Physics* **113**, 233104 (2013).
- [126] M. Hada, K. Okimura, and J. Matsuo, *Physical Review B* **82**, 153401 (2010), ISSN 1098-0121.
- [127] M. Liu, H. Y. Hwang, H. Tao, A. C. Strikwerda, K. Fan, G. R. Keiser, A. J. Sternbach, K. G. West, S. Kittiwatanakul, J. Lu, et al., *Nature* **487**, 345 (2012), ISSN 1476-4687.
- [128] Y. Cui and S. Ramanathan, *Journal of Vacuum Science & Technology A* **29**, 041502 (2011).
- [129] E. Abreu, M. Liu, J. Lu, K. G. West, S. Kittiwatanakul, W. Yin, S. A. Wolf, and R. D. Averitt, *New Journal of Physics* **14**, 083026 (2012).
- [130] A. A. Savchenkov, I. S. Grudinin, A. B. Matsko, D. Strekalov, M. Mohageg, V. S. Ilchenko, and L. Maleki, *Opt. Lett.* **31**, 1313 (2006).
- [131] A. A. Savchenkov, A. B. Matsko, and L. Maleki, *Opt. Lett.* **31**, 92 (2006).

[132] M. K. Chin and S. T. Ho, *J. Lightwave Technol.* **16**, 1433 (1998).

VITA

Matthew Thomas Simons

Matt T. Simons was born on the 29th of March, 1985 in Fairfax County, Virginia. He attended Floris Elementary School, Benjamin Franklin and Rachel Carson Middle Schools, and Oakton High School. While at Oakton, he discovered an interest in physics thanks to his two great physics teachers and the Team America Rocketry Challenge. In 2003, he entered the University of Virginia. He graduated with distinction in 2007 with a Bachelor of Science in Physics and a minor in Foreign Affairs. Matt entered the College of William & Mary in the fall of 2007, and began work with Dr. Irina Novikova in the Quantum Optics Group to develop whispering-gallery mode resonators as a source of nonclassical light. He received a Master of Science in 2009.